SLL 82 469 $-SLC$

469

SCALING OF X-RAY PREIONIZED MERCURY BROMIDE LASERS
Final Report

Submitted to
Defense Advanced Research Projects Agency

November 1981

DTIC QUALITY INSPECTED 4

19980309 384

MATHEMATICAL SCIENCES NORTHWEST, Inc.

U3898

Accession Number: 3898

Publication Date: Nov 01, 1981

Title: Scaling of X-Ray Preionized Mercury Bromide Lasers - Final Report

Corporate Author Or Publisher: Mathematical Sciences Northwest, 2755 Northrup Way, Bellevue, WA 98004

Report Prepared for: Defense Advanced Research Projects Agency, Arlington, VA Report Number Assigned by Contract Monitor: SLL 82 469

Comments on Document: Archive, RRI, DEW

Descriptors, Keywords: Scaling X-ray Preionize Mercury Bromide Laser Experiment Model Closed Loop Requirement Risk Optics

Pages: 00109

Cataloged Date: Nov 27, 1992

Contract Number: N00123-80-C-1136

Document Type: HC

Number of Copies In Library: 000001

Record ID: 25231

Source of Document: DEW

SCALING OF X-RAY PREIONIZED
MERCURY BROMIDE LASERS

Final Report
(Contract No. N00123-80-C-1136)

Submitted to

Defense Advanced Research Projects Agency

Submitted by

Mathematical Sciences Northwest
2755 Northup Way
Bellevue, Washington 98004

November 1981

CONTENTS

Section I

INTRODUCTION

This report details work performed by MSNW under the Phase I
DARPA/NAVY Space Based Blue Green Laser Program. The goals of this program
were to demonstrate over 1 J at over 1 percent efficiency in the Blue Green
spectral region, develop appropriate models to extrapolate to a 2 J device,
and develop a design of a 200 watt device. The focus of our work was the
HgBr electric discharge laser. Our efforts emphasized preionized,
avalanche discharge pumping of this medium. X-ray preionization was
selected as the preionization method for large apertures and long lifetimes
needed for the ultimate space based laser. The effort described here
resulted in a single pulse device that easily exceeded the required energy
and efficiency goals.

The HgBr laser lases at 502 and 504 nm and amplifies strongly over a
roughly 5 nm bandpass.[1] It is the only laser system currently under
consideration for Naval underwater communication application that operates
directly, in the blue-green spectral region, without a conversion scheme.
MSNW has demonstrated that HgBr lasers can be scaled to the range of single
pulse energies of interest. Energies of over 1.75 J have been obtained.
Laser efficiency measurements at MSNW show that overall laser system
efficiencies for future systems in excess of 1 percent are achievable for
preionized discharges operating at the requisite single pulse energies.
The HgBr laser system thus offers many attractive features for the laser
communications application.

The development of efficient, long lifetime laser systems operating
in the blue-green spectral region is needed for naval underwater
communications applications. Lasers of 200 W or greater average power,
with an overall efficiency better than 1 percent, are required for a
satellite based blue-green laser communications system. For successful
deployment in space, such a device ultimately needs to be capable of a 10^{10}
shot lifetime. The lifetime and satellite deployment of such a device

place stringent requirements on the development of the laser device and its associated subsystems. The next logical step is development of a 200 W, 1 percent efficient, HgBr laser system capable of running for 10^8 shots. Such a laser system will develop much of the technology needed to design a 10^{10} shot, pre-space qualified brassboard laser.

While offering a number of potential advantages in terms of spectral operating regime and system simplicity, the HgBr laser did not have a technology base at the start of this program as broad as that relating to rare gas halide discharge lasers, the drivers for the competitive Raman conversion blue green laser systems. Most notable in a comparison to XeCl laser technology are issues of materials of construction for truly long run operation. The ultimately achievable energy density at high efficiency, the ultimately achievable pulse duration for stable preionized discharge, and even the optimum pressure and gas composition for preionized discharges are still not completely determined. Thus the efficiency and single pulse energy measurements quoted here from current data should be considered conservative lower bounds for a technology that is still capable of growing.

The MSNW approach to scaling HgBr lasers features the use of x-ray preionized avalanche discharges. This technique was first applied to rare gas halide avalanche discharges by workers at UCSD[2] and in Japan.[3] The UCSD studies and analysis[4] clearly show that large apertures (up to 5 x 5 cm^2) and stable long pulse avalanche discharges can be achieved with this method. Starting early in 1980, we applied this technology to a variety of avalanche discharge lasers, XeCl, CO_2, and HgBr. MSNW has since that time built and developed 30 cm, 50 cm, and 1 m HgBr discharge lasers that have successfully shown the aperture and energy scalability of this technique. We have produced pulses of over 1.75 J at efficiencies of up to 1.4 percent in the 1 meter device, and efficiencies over 1.7 percent at energies over 1.4 J. This efficiency is defined as energy out ratioed to energy stored on an intermediate capacitor. This capacitor is resonantly charged on a time scale 30 times longer than the discharge pump pulse. Thus the charging circuit contributes negligibly to laser pumping.

While the x-ray preionization scheme has obvious direct application for large volume HgBr discharge scaling, it is also eminently suited for space qualified application. Our experimental studies and analysis have shown that an adequate, uniform x-ray preionization level can be achieved with total electron beam currents of less than 10 amps. Moreover, a properly designed x-ray generator, should be capable of producing adequate preionization when operating at fairly low electron beam voltages. The voltage needed for x-ray preionization is considerably lower than that needed for an e-beam to preionize or sustain a discharge laser.

The x-ray preionized approach offers the potential for good chemical compatibility and very long life. Because the preionizer is separated from the gas flow by a solid x-ray window, gas lifetime should be better than that achievable by a uv preionized discharge, wherein the gas mixture comes into intimate contact with preionizing arcs. Comparing system longevity to an e-beam preionized or e-beam sustained discharges, the x-ray technique can utilize an x-ray window thickness that is substantially greater than the window thickness necessary for an e-beam preionized or sustained laser. Such extra window thickness thus minimizes the risk of mechanical fatigue resulting from the cyclic pressure stress induced by the roughly 1 atm overpressure due to repetitive discharge loading.

In meeting the objectives of this program, we utilized three test devices: a 30 cm gain length device, a 50 cm gain length device, and a 1 m device.

The 30 cm gain length device built, under NOSC sponsorship, was used to first demonstrate an x-ray preionized HgBr laser. Active cross-sectional areas of up to 3 x 2 cm^2 were observed, a significant advance over that achieved by uv preionization. This device was used to study variations in laser performance with electrical driver characteristics. Single pulse energies of up to 230 mJ were observed, but efficiencies were low, 1/2 percent or less. However, the device provided important lessons in materials compatibility and $HgBr_2$ chemical purity, and in efficiency losses in the pulser.

A second x-ray preionized device was built under this program. The laser uses glass construction and high purity chemicals, and thus corrosion was greatly reduced compared to our 30 cm device. The device has a 50 cm gain length, and provides a direct comparison to the high efficiency 55 cm NOSC uv preionized laser device.[5] The NOSC device has demonstrated up to 1.3 percent overall efficiency when injection locked, albeit at lower single-pulse energies. The MSNW 50 cm device has produced up to 520 mJ from an aperture of 3 x 3 cm^2. An extensive set of data was achieved with this device. The data showed qualitatively similar variations of efficiency with voltage and composition as observed at NOSC. However, the laser efficiency observed was lower than at NOSC, 0.6 percent relative to a slowly pulse charged capacitor array, and 0.4 percent overall. Our analysis has shown that this has been due in large part to optical losses, non-optimized electrode contour leading to useless energy flow in the nonextracted laser volume, and poor matching of the pulsers utilized to excite the discharge. A critical finding was the gradual degradation of optical transmission of antireflection coated windows, strongly suggesting that ultimate systems use Brewster windows.

To achieve outputs over 1 J, we built a 1 m gain length cell capable of operating at pressures well in excess of that possible before. With a 3.5 cm electrode spacing lasing efficiencies of up to 1.3 percent, and single pulse energies of up to 1.1 J at over 1 percent efficiency have been observed. Increasing electrode spacing to 5 cm yielded single pulse energies of over 1.75 J. The efficiency of this device relative to an intermediate capacitor store that was slowly pulsed charged was 1.6 percent at energy densities of 0.6 J/l. This is substantially better efficiency than that observed in our smaller scale systems. If one defines a laser head efficiency, i.e., energy out ratioed to energy that actually gets to the laser head, after output switch losses, our 1 meter HgBr laser is operating at 2.1 percent efficiency. Our analysis presented in Section II supports the thesis that with proper electrode contouring, somewhat longer pulse laser operation, and careful attention to energy losses in switches and resistive losses of the device, overall efficiencies in excess of 1 percent are readily achievable for the 200 W Phase II device.

The area of long lived pulsed power is obviously critical to future phases of this program. A long living electrical output switch is a key element. In our most successful 1 m single pulse device experiments we used a triggered multichannel gas switch. Such switching may possibly be acceptable for long life operation, with some development. However, the additional flow loop and gas makeup system for the railgap gas make this somewhat less efficient and more risky for long life. Hence, scaling our current switch technology to average power is less attractive to us for 10^8 and 10^{10} shot operation at high efficiency. As such, we considered triggered railgaps only as a backup or preliminary switch to be used in initial shakedown tests of the system. Multiple parallel thyratrons are the switch of choice studied in this contract period. These devices have proven long lifetime when used at modest current rate of rise. However, they require a fair amount of auxilliary heater power. Thus, when many are used in parallel to achieve high current rate of rise, heater losses degrade overall system efficiency. The multiple thyratron switch pulser can have a very long lifetime if properly engineered. Alternate switching approaches may need to be developed for truly long life operation.

Although the laser head, pulser, and flow loop are major elements of any future device, a number of important auxiliary systems need to be considered. The ultimate device needs to operate narrow band. MSNW has extracted energy successfully with a 0.01 nm seed source. The experiments utilized coincidences between Ar ion laser lines and the HgBr lasing and amplifying spectrum. Although only a partial laser aperture was extracted, and hence full energy was not attained, these experiments give reasonable expectation that HgBr can be efficiently extracted with an extremely narrow band. Verification tests for other wavelengths need to be performed because the Ar ion lines chosen need not be the optimum extraction wavelength.

Injection locking or MOPA configurations also are beneficial to laser efficiency as they allow for extraction during the optical buildup time. For our 1 m laser this is estimated to improve efficiency about 10 percent, while the shorter gain length NOSC 55 cm and MSNW 50 cm devices

could be expected to yield 20 - 30 percent enhancements. Since a narrow bandwidth is desired and since efficiency is degraded in generation of a narrow band in an oscillator, some low power seed source is needed to inject the 200 W device.

The remaining sections in this report detail the work performed for this contract. Section II describes the experimental measurements in the three lasers studied for this program. The modeling of the discharge excited laser system is described in Section III. Section IV details the design approach and our methodology for rapidly developing materials for the closed loop 200 W laser.

REFERENCES

1.   E.J. Schimitschek and J.E. Celto, Opt. Ltr. 2, 64 (1978); R. Burnham, Appl. Phys. Lett. 33, 156 (1975).

2.   S.C. Lin and J.I. Levatter, Appl. Phys. Lett. 34: 505 (1979).

3.   S. Sunuida, M. Obura, and T. Funiska, Appl. Phys. Lett. 33: 913 (1978).

4.   J.I. Levatter and S.C. Lin, J. Appl. Phys. 51: 210 (1980).

5.   E.J. Schimitschek and J.E. Celto, Appl. Phys. Lett. 36, 176, (1980).

Section II

EXPERIMENTAL MEASUREMENTS

During the past 13 months, three single pulse x-ray preionized HgBr lasers have been built and tested at MSNW. Their length, aperture and laser performance are summarized in Table 2-1 and discussed in this section. These devices each taught significant lessons in the use of x-ray preionization and the foibles of HgBr lasers. The smaller lasers were in retrospect very sensitive to optical losses and generally exhibited performance which deteriorated with time. The 30 cm device had severe corrosion problems due to impure $HgBr_2$. The 50 cm device served as a touchstone for comparison to the 55 cm device at NOSC, a device which showed considerably better efficiency than our first two HgBr discharge lasers. The 100 cm device was brought on line recently and has proven that efficiencies as good or better than those achievable at the 60 - 100 mJ level at NOSC can also be attained in a large volume, 1 m gain length device producing single pulse energies of almost 2 J.

2.1 The 30 cm Device

The smallest of our three devices was initially built under a separate earlier program for HgBr laser scaling studies funded by the NOSC/ONR.[1] The discharge was housed in a ceramic tube. The chamber was heated by stainless clad coaxial heater wires attached to a copper heating jacket which surrounded the laser tube. A blanket of ceramic fiber provided thermal insulation between the laser tube and the surrounding environment.

The x-ray generator was an available cold cathode electron beam gun operating at a current density of 1-4 A/cm^2. The x-rays were generated by striking a 0.5 mil Ta foil and were transported through the 2 mil thick Al foil, the insulation material, and the ceramic laser tube walls.

Table 2-1

Summary of MSNW X-ray Preionized Devices

Device Gain Length cm	Aperture cm²	Single Pulse Energy J	Efficiency %	Energy Density J/L
30	3 x 2	Up To 0.23J	0.5% At Best And Very Sensitive To System Degradation	Up To 1.5
50	3 x 3 (Not Always Filled)	Up To 0.52J	0.5% At Highest Energy Relative To Pulsed Capacitor 0.6% At Lower Energies	1.2 At High Energy 0.35 At Best Efficiency
100	3.5 x 3.5	Up to 1.1J At Greater Than 1.0% Efficiency 0.650 J at 1.3%	Over 0.8% To Wall-plug Over 1.3% to slowly pulse charged capacitor	1.1 At Better Than 1% Efficiency
100	4.5 x 4.5	Over 1.75 J At Efficiency Greater Than 1.4%	Over 0.9% To Wall-plug Over 1.6% to slowly pulse charged capacitor	0.7 At Better Than 1.5% Efficiency

Under an earlier NOSC contract[1] a measurement of the preionization electron number density was made for two situations: the normal cell, and one with 1/16" lead inserted between the laser tube and x-ray source. We found stable discharges achievable with electron densities of 5×10^8 per cm^3 corresponding to an electron source strength of 2×10^{13} ions/cm^3/sec. In a properly designed preionizer this can be achieved with e-beam currents densities much less than 100 ma/cm^2.

Both external and internal optical cavity configurations were tried on this laser cell. The external cavity optics were isolated from the laser medium by near normal incidence windows. The best performance was obtained using the internal cavity arrangement with reflectors in direct contact with the laser gas and mounted to the laser tube via adjustable metal bellows assemblies.

The effects of various electric pulsers on laser performance are summarized in Table 2-2. Three different PFNs were used. The "baseline" performance in Ne/N_2/HgBr$_2$ mixtures of 180 mJ from the 30 cm device was obtained with "PFN A", an LC inversion circuit charged to 30 kV and switched by a triggered spark gap. The total capacitance of this circuit was nominally 80 nF at 33 kV. Accurate determination of the energy stored on this PFN required analyzing the charging current and voltage waveforms because of voltage dependent capacitance above 25 kV.

The laser performance with PFN A degraded with time due to corrosion inside the laser tube and on the PFN connections, and probably optical losses that grew with laser window and reflector age. Thus laser output energies obtained using PFNs B and C were separately compared to the energy obtained with PFN A just prior to the installation of each alternative drive circuit.

The highest laser output energy of 230 mJ was obtained using PFN B, a 100 nsec Blumlein circuit with a capacitance of 160 nF, charged to 34 kV. This represented a 64 percent improvement over the laser energy obtained with PFN A. PFN C, a pulse-charged lumped-element array, had a nominal total capacitance of 115 nF. When charged to 32 kV, PFN C resulted

Table 2-2

Single Pulse Scaling Results
on 30 cm Device

		V_o	Laser Energy
PFN A:	L-C Generator*	30 kV	180 mJ
PFN A:	L-C Generator**	30 kV	140 mJ
PFN B:	100 nsec Blumlein	34 kV	230 mJ
PFN A:	L-C Generator***	30 kV	110 mJ
PFN C:	Pulse Charged Capacitor Array	32 kV	150 mJ

---

*   Initial Performance With Short Connections

** Subsequent Performance With Longer Connections

***Performance With PFN A Degraded With Time Due To Corrosion
Inside The Laser Tube And On The PFN Connections

in a laser output energy of 150 mJ, corresponding to a 36 percent improvement over the laser energy obtained with PFN A. The results were all obtained with a gas mixture composition of 12 torr $HgBr_2$ (T=185 C) and 150 torr N_2 in 2.5 atm Ne.

For PFN A, the peak voltage was 42 kV and the peak current was 13 kA, corresponding to a current density of 217 A/cm^2 over the estimated 2 x 30 cm^2 discharge area. With PFN B the peak voltage was 30 kV and the peak current was 20 kA. Lasing pulses of up to 70 ns FWHM were observed with PFN B, thus showing that stable x-ray preionized discharges could be achieved.

With both PFNs considerable time elapsed from the start of the discharge current flow until the laser exceeded threshold. This delay is shown more clearly in Figure 2-1, which depicts the power flow past the current and voltage monitors for PFN A during gain buildup and laser oscillation. Detailed analysis of the discharge voltage and current waveforms during laser oscillation indicated that of 35 J initially stored in PFN A, only 19 J were transferred into the laser head, 4 J were stored in the circuit inductance and 14 J were dissipated in the spark gap. This example showed clearly the need to utilize more than one channel for efficient switching. The overall efficiency as determined by ratioing laser energy to energy stored on the PFN was 0.5 percent. The waveform analysis implied a laser head efficiency of only 1 percent. This is at variance with our most recent results and was probably due to the short gain length, corroded electrode connections, and optics and current flowing outside the active region.

As a result of experiments on the 30-cm device, several technical problem areas were identified. A substantial amount of metal corrosion was observed at points where solid $HgBr_2$ was in contact with the stainless steel electrodes and feedthroughs. Chemical analysis showed the corrosion to be bromide salts of iron, chromium and nickel, the principal constituents of stainless steel. Conversion of electrode material into metal bromides implies the release of Hg vapor. The quenching of $HgBr^*$ and $N_2(A)$ by Hg vapor, the deterioration of electrode surface finish
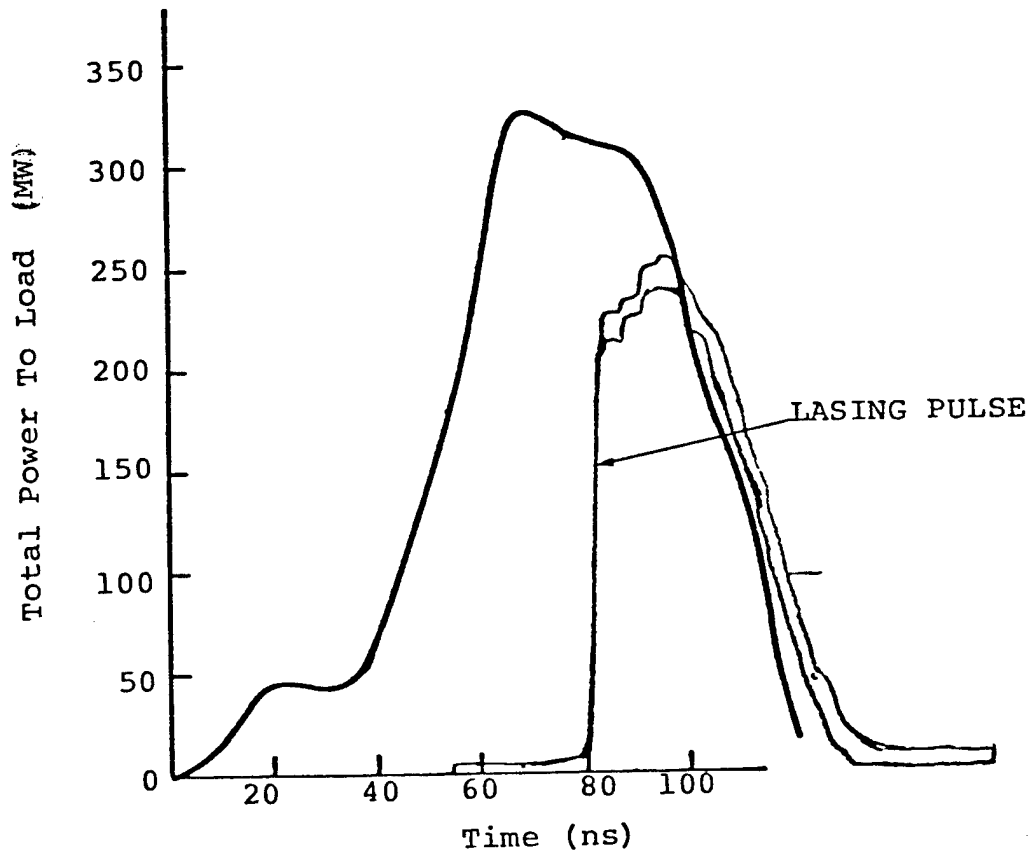
Figure 2-1. Power Flow Past I-V Monitor – PFN A.

80 04217

accompanying corrosion, and the overall consumption of $HgBr_2$ all contributed to the observed steady degradation of laser performance with time. In the absence of extensive corrosion, periodic cell evacuation followed by refills of fresh $HgBr_2$ restored laser performance.

Chemical purity of the $HgBr_2$ was not an issue specifically addressed in experiments on the 30-cm device. The inherently appreciable concentrations of impurity substances in commercially available $HgBr_2$ was recognized from chemical analyses of commercial samples, and steps were subsequently taken to insure that the $HgBr_2$ admitted to the larger scale laser devices was purified by three or more vacuum distillation cycles.

In addition to metal corrosion, appreciable quantities of particulates were generated in the laser medium by the discharges. The particulates can in principle arise from small crystals of $HgBr_2$, ablated electrode material, and corrosion particles. A single discharge in a freshly prepared laser medium was sufficient to produce intense particulate scattering as observed with a HeNe laser probe beam, and appreciable reductions in laser energy. This suggested that a separate gas/$HgBr_2$ mixing manifold be utilized, a method that was introduced on the 1 m device, and should obviously be implemented in the 200 W machine.

Oxidative corrosion of some of the circuit connections housed within the heating jacket, but outside of the laser tube itself was observed. This resulted in excessive resistive losses in the PFN circuit during discharge. By altering the circuit mechanical design we have minimized this source of useless energy loss in the laser head. Resistive connections must be minimized in all elements of the device in order to achieve optimum efficiency.

2.2 The 50 cm Device

A substantial amount of the learning process for this program involved a 50 cm gain length, glass tube laser. The device was used for gain and narrow band extraction experiments, optimization of PFN, gas mixture and deposition rate. Because of its length and materials choice it

provided a direct, one to one comparison with the uv preionized NOSC laser which had better efficiency than our 30 cm device. A summary of the properties of the laser head are given in Table 2-3, and in Figure 2-2 is a photograph of the assembled laser head before being placed in its heat shield and having electrical drivers attached.

The performance and relevant characteristics of the 50 cm device are summarized in Table 2-4. For comparison we show the properties of the efficient small scale NOSC device. The table shows that large apertures, up to 3 x 3 cm^2, and high energies are achievable in a small system. However the best efficiency was a factor of two or more lower. A significant question existed during the months of use of the 50 cm device regarding the cause for the degraded efficiency, relative to the similar gain length NOSC device. These questions raised the suspicion that x-ray preionization may not for some reason be capable of producing as high an efficiency. The table shows that there were several other differences between the two machines other than the style of preionization.

The photograph (Figure 2-2) clearly shows two of the shortcomings of this device: too few feedthroughs (only four on one side and end returns on the other), and one electrode that is flat rather than contoured. The first effect leads to increased circuit inductance for driving the discharge. The second leads to a poor impedence match because of extraneous current flow outside the laser active volume. Moreover, the current in the fringe areas that are optically accessible is also wasted because of weak pumping. AR coated windows (or on occassion laser reflectors) are contained in the end flange mounted on bellows shown in the photo. A significant finding of the 50 cm device campaign was that AR coatings became lossy with age. The cause of the window deterioration is not known, but it appears to be due to $HgBr_2$ or impurity attack. We have found that the loss in transmission does not occur for that part of the window isolated from gas by a virtue of being behind an O-ring. Thus a better approach for a long run device is to utilize Brewster end windows.

Table 2-3

Characteristics of 50 cm Laser

Discharge Length   -   50 cm

Discharge Width   -   3 cm (voltage dependent)

Electrode Gap   -   3 cm

Cavity Length   -   1 m

Gas Pressure   -   2 atm

Gas Temperature   - 200°C

Materials   -   Pyrex Glass Plasma Tube, 304 Stainless Steel Electrode Assembly and Optical Flanges, Gold Plated Electrode Feed-throughs and Fasteners, Viton O-Rings.

Overall Dimensions of Laser Head   -   1.4 m long x 15 cm diameter (including Heater Shell and Electrical Feed throughs).

Windows   -   AR Coated Flats in Continuous Contact with hot $HgBr_2$ Vapors.
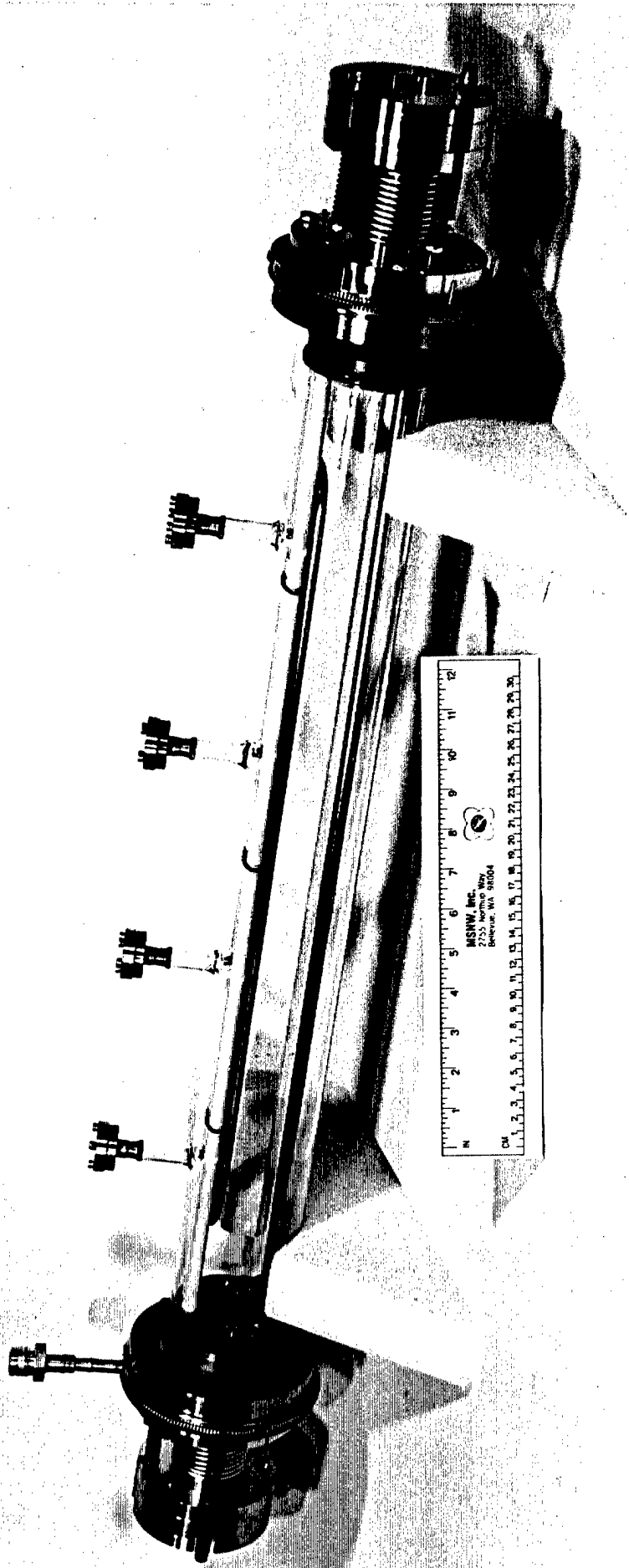
Figure 2-2. MSNW 50 cm HgBr Laser Head

Table 2-4

Comparison of HgBr Discharge Lasers

Laboratory	NOSC	MSNW
Type	Avalanche-Self Sustained	Avalanche-Self Sustained
Ionization Source	UV	X-Ray
Length/Energy	55/60 - 100 mJ	50/250 - 525 mJ
Effeciency (%)	1.0 Free Running	0.6 Free Running
	1.3 Locked (Broad Band)	--
Electrodes	Strongly Curved	Gentle Curve/Flat
Aperture (cm^2)	2.7 x 0.9	3 x 3
Excitation Rate (kW/cm^3)	~ 600 For Best Results	> 600 - Shrinking Profile At Lower E/N
Inductance (nH)	~ 30 nH	~ 100 nH
Impedance (Ω) Driver	~ 1.3	~ 1.7
Load	~ 1	? < 0.5
Window/Optics	Brewster/External	AR Coat/Internal

Analysis of current and voltage waveforms for our 50 cm device and the NOSC device showed that the impedance was well matched in the NOSC device, but poorly matched in our 50 cm laser. This in and of itself decreased the efficiency of the MSNW system by a factor of two relative to the NOSC machine.

The precision of the measurement of efficiency listed in Table 2-5. and in the following discussion depended on the selection of PFN. Several different configurations of electrical pulsers were used to optimize the laser performance with the 50-cm device. The fundamental design of the pulser in every case was a rapid pulse charge network or line with the pulse charging time dependent on the output switch. Three basic variations of this design were utilized: a lumped element array utilizing ceramic capacitors, a copper strip line assembly with a 100 ns pulse length. The copper/insulator line was rolled into a compact configuration. Finally, a pulser composed of three equivalent transmission lines each separately energized by a single 12 nF capacitor and switched with three triggered spark gaps. The performance and characteristics of these three pulsers are summarized in Table 2-5.

The first two pulsers utilized self breaking surface rail gaps to switch the high voltage pulse to the laser load. This switch required rapid pulse charging of the line (~500ns) and efficiency numbers are quoted ratioed to energy flowing through the line or capacitors up to the time the voltage reversed, usually after termination of lasing. No attempt was made with these pulsers to relate the efficiency to the primary capacitor store since the efficiency did not exceed the 1 percent goal from the intermediate capacitor/line. The line using three parallel 12 nF capacitors and triggered switches allowed us to slowly pulse charge the capacitors. Negligible energy could flow from the D.C. charged capacitor to the laser head during the 100 ns lasing pulse and the efficiency quoted is that obtained by ratioing the energy stored on the three capacitors at the time of switch triggering. Again since the efficiency relative to these intermediate storage capacitors did not exceed the 1 percent goal, no measurement was made of the efficiency relative to the D.C. charged

Table 2-5

Components and Performance of Pulsers
for 50 cm Device

Pulser Type	Capacitance	Output Switch	Single Pulse Energy	Efficiency	Pulse Duration
A) Lumped Element Murata Ceramic Capacitor Transmission Line $\tau_p \sim 70$ns	130 nF	Surface Railgap	525 mJ 2 atm Ne 225 torr N_2 6 torr $HgBr_2$	0.56	80 ns
B) Rolled Up Copper Sheet Transmission Line $\tau_p \sim 100$ns	40 nF	Surface Railgap	215 mJ 2.4 atm Ne 45 torr N_2 12 torr HgBr 380 mJ 2 atm Ne 225 torr N_2 6 torr $HgBr_2$	0.6% 0.4%	120 ns
C) Three Parallel Maxwell Capacitors	36 nF	Three Triggered Spark Gaps	Up To 325 mJ Extensive Variations Of Gases And Laser Output	0.6% At About 160 mJ	80 ns

capacitor stored energy. Moreover no attempt was made to make the transfer efficiency higher. Only in the 1 m device was efficient charging of the intermediate line studied.

The 50 cm device with the triggered spark gap pulser did provide a significant data base for model comparison. This has enabled us to understand better some of the pitfalls and performance design limits of x-ray preionized systems. Figure 2-3 shows the output energy as a function of stored energy for a wide variety of gas mixtures. The comparison to the corresponding curves from the NOSC device are striking. Clearly low N_2 mixture fractions can yield higher efficiency, over a narrow range. As found at NOSC increased N_2 also increases the single pulse energy. A second feature of this plot is that the efficiencies are lower than the NOSC device, not even including the inefficiencies of the capacitor charging.

The laser beam cross-section was monitored using burn patterns on carbon paper obtained for the 5 percent N_2 mixtures of Figure 2-4. These results show that the higher efficiencies were achieved when the 3 cm x 3 cm aperture is under filled by the laser beam. In other experiments, visual observation of the discharge region from above showed that the discharge extends well beyond the volume defined by the cavity mirrors and can stream off the ends to the end plate current returns. Clearly, the laser has excited regions that are not extracted by virtue of insufficient gain and vignetting. We confirmed this with gain measurements. Gain in the 50 cm device was probed with a cw Ar^+ laser. A fortuitous overlap of the 501.7 nm Ar^+ laser and the high resolution spectrum of the HgBr medium was exploited (Figure 2-5). A typical gain temporal signal is shown in Figure 2-6. Note that the gain FWHM, 100 ns, is longer than the lasing pulse, implying inefficiencies in laser startup.

A plot of the peak gain as a function of the charging voltage is shown in Figure 2-7 for a gas mixture containing 12 torr $HgBr_2$ and 46 torr N_2 in 1.6 Amagat Ne. For these data the gain was measured at two locations: along the optical axis and parallel to but approximately 1.5 cm above this axis. At low voltages the gain off axis drops, and efficient

	HgBr$_2$(torr)	N$_2$(torr)	Ne(Amagat)
■	12	18	1.6
⊗	12	46	1.6
○	12	91	1.6
△	4.6	91	1.6
●	12	180	1.6
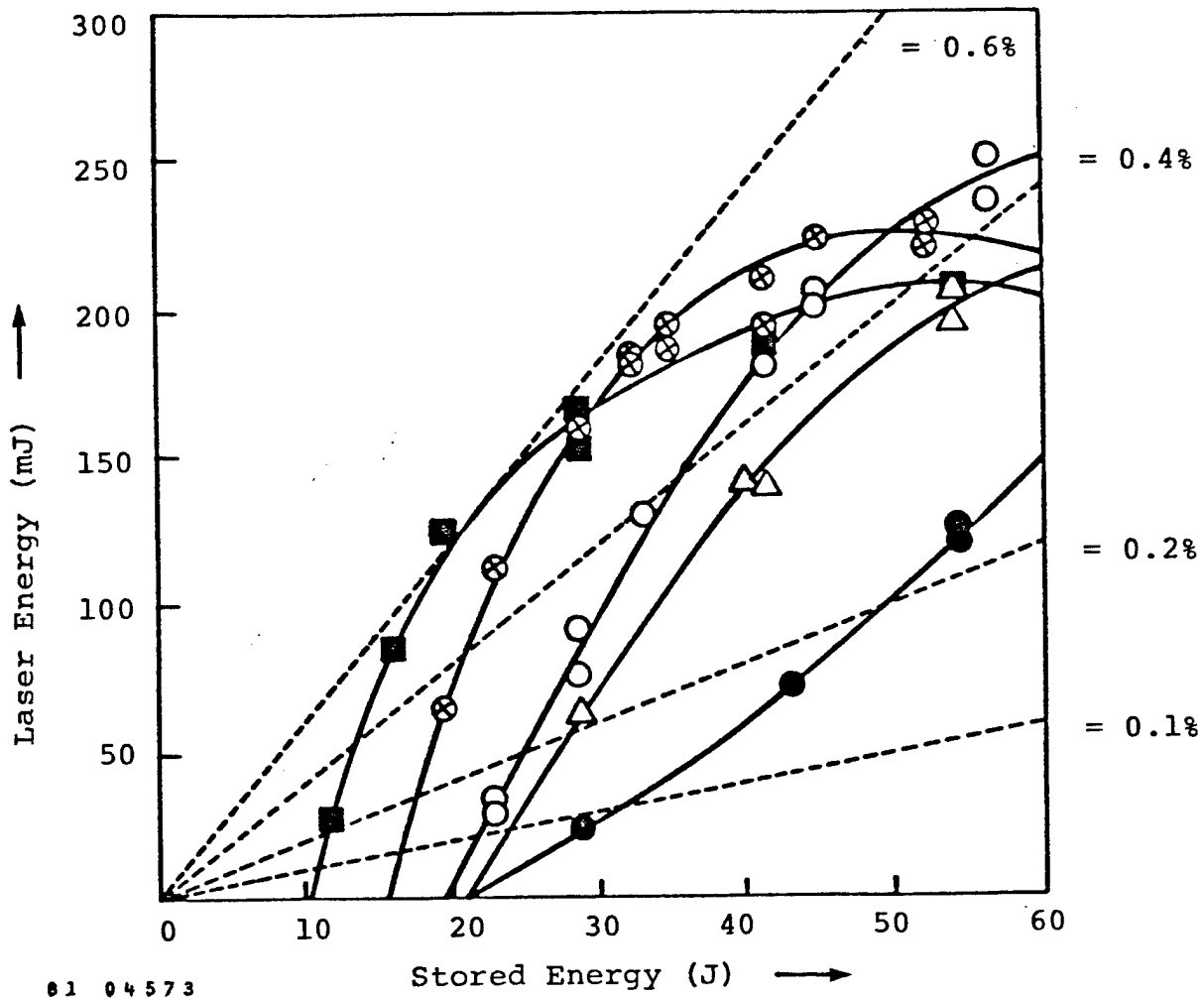
Figure 2-3. Laser Performance with the Multiple Triggered Spark Gap Driver and 50 percent Output Coupling.
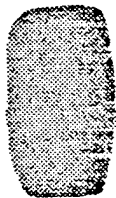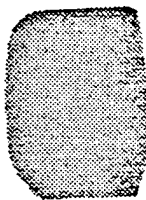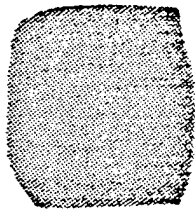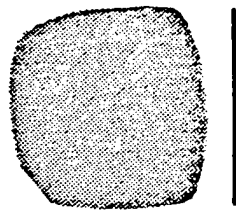
STORED ENERGY (J)	13.6	28	35	45	54
CHARGE VOLTAGE (kV)	27.5	30	32.5	37.5	40
ENERGY OUTPUT (mJ)	30	150	180	210	230
EFFICIENCY (%)	0.22	0.54	0.52	0.45	0.42

81 04795

Figure 2-4. Burn Patterns for 50 cm HgBr Discharge. The highest efficiencies were achieved with an under square lasing volume. Gain outside the lasing aperture was measured.
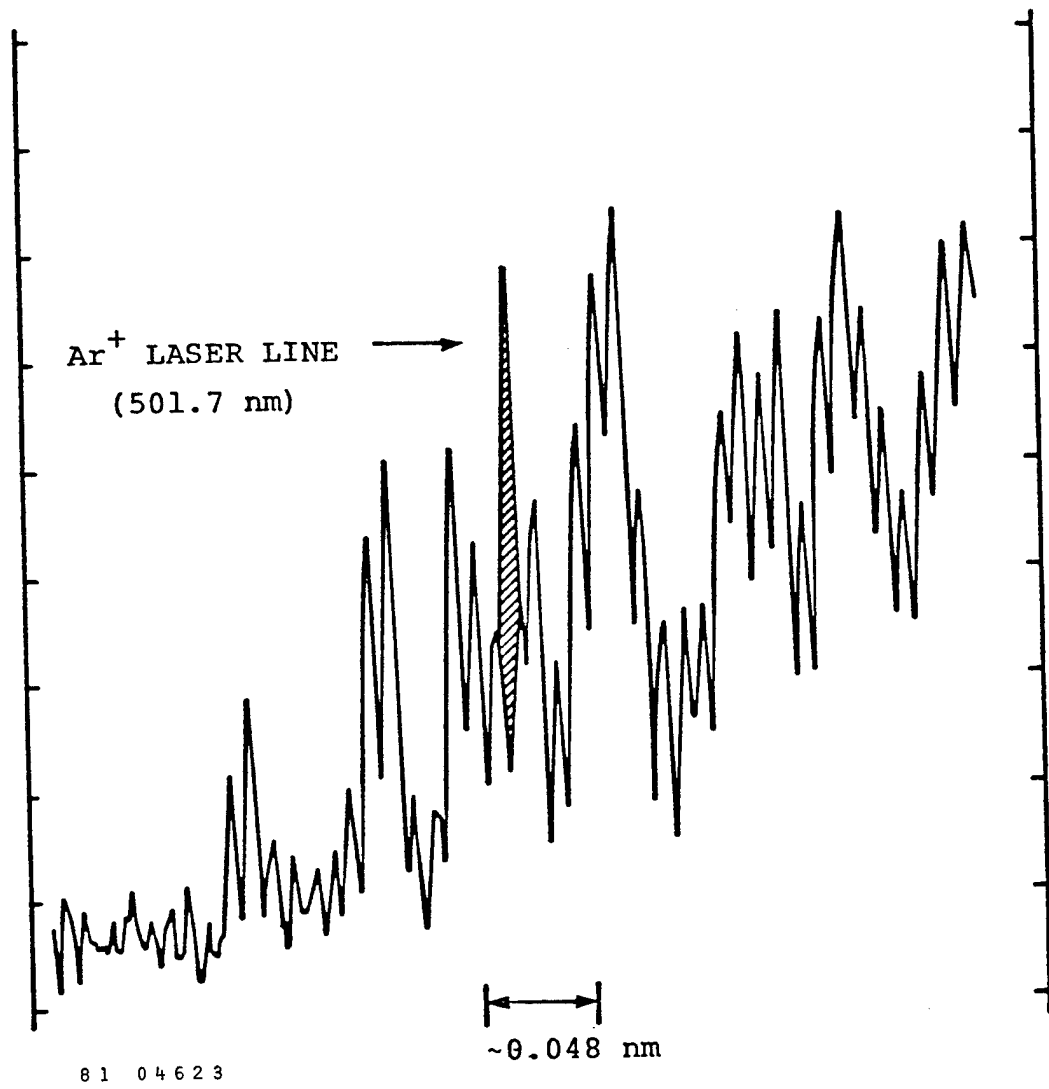
Figure 2-5. High Resolution HgBr Laser Spectrum Near 502 nm.

Intensity (ARB. Units)

I_O X 4

I

1 μs/div

50 ns/div

81 04653
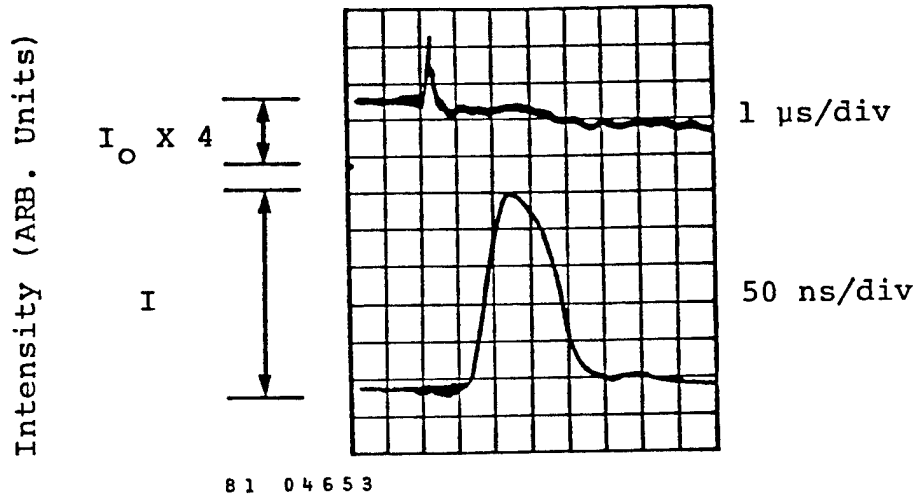
o 39 kV CHARGE

o ~ 0.5% EFFICIENCY

o FULL OR OVERFULL
   DISCHARGE

o $g_{PEAK} \sim 5\% \ cm^{-1}$

Figure 2-6. HgBr Gain Temporal Profile.
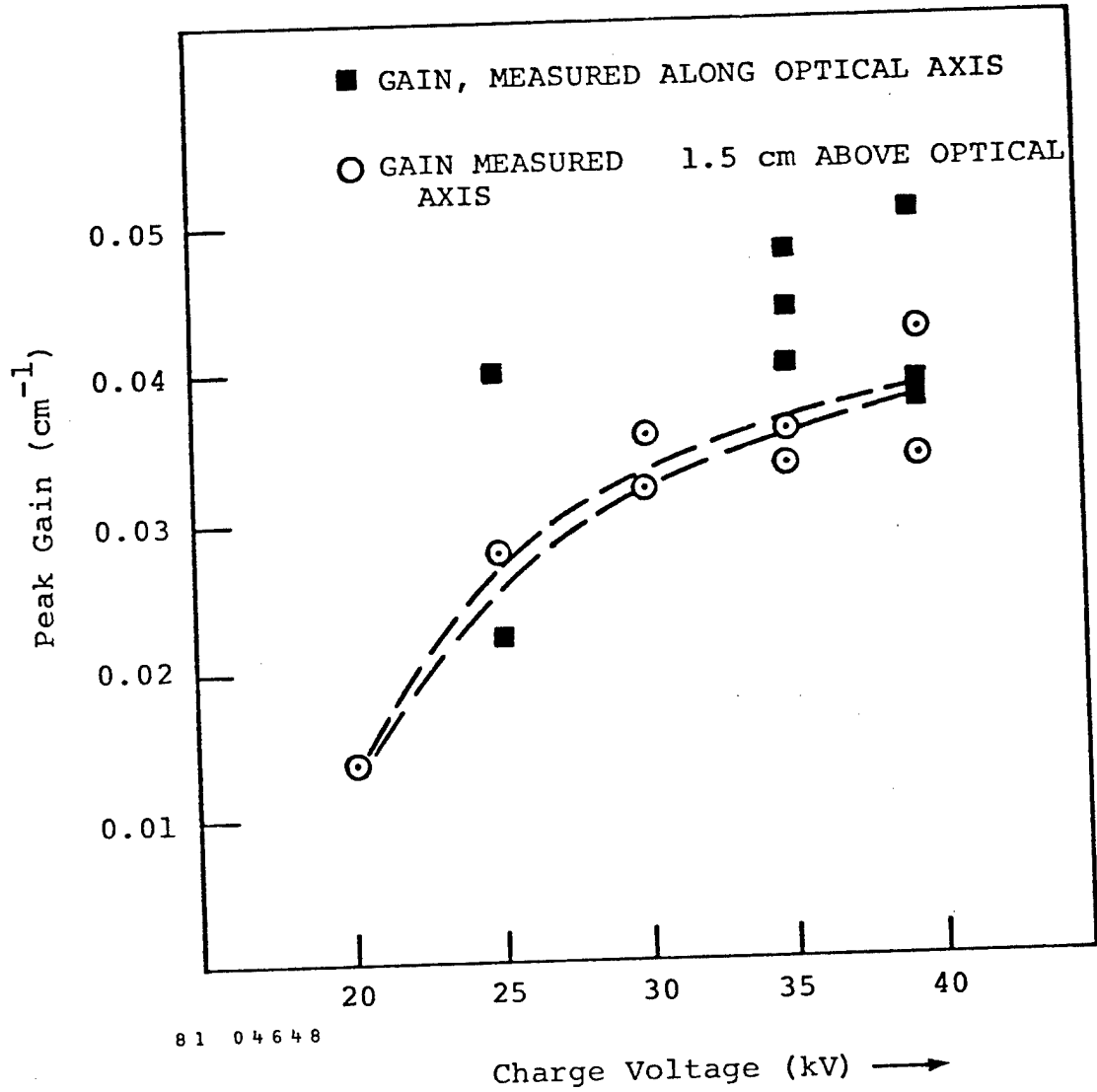
Figure 2-7. Peak Gain Measured on and off Axis.

extraction in this device becomes more difficult. The energy flowing outside the optically active region is wasted. This effect was observed also when the laser was operating near optimum conditions for this pulser.

The laser output shape was also found to be sensitive to mirror and AR coated window losses. We found that the loss of two AR coated windows increased from about 2 percent when new to 40 percent after six weeks of contact with $HgBr_2$. This change in transmission is obviously detrimental to lasing performance, especially in a cavity with a g_oL of only 2.5, since the gain to loss ratio is well under 10, the approximate minimum value of gain to loss ratio for efficient extraction.

The 50 cm device used glass construction. This gave us the ability to monitor sidelight fluorescence for the first time. Figure 2-8 shows sidelight fluorescence without lasing and with various output coupler reflectivities. The cross hatched area represents wasted $HgBr^*$ fluorescence which if extracted would increase performance by up to 30 percent. Such effects have been measured by NOSC. For our 1 m device the improvement would be smaller, only 10 percent or so.

Narrow Band Extraction

One of the most significant results of the 50 cm device effort described above was the efficient extraction of the HgBr* energy density in an extremely narrow band. We have utilized the overlap of the 501.7 Ar ion line to extract in a very narrow band. The overlap is shown in Figure 2-5. A cw Ar ion laser was used to injection lock a flash lamp pumped long pulse (~200 nsec) dye laser. The dye laser was injected using a ring resonator. The spectral content of the dye laser was measured by video recording the highly dispersed output of a 1 m monochromator using a grating in 27th order. We found that 50 percent of the dye laser output was within a 7×10^{-3} nm bandwidth and 50 percent in a broad 2 nm background, that is, the contrast ratio was 130 to 1. This signal was amplified in two passes through the center of the 50 cm HgBr laser. We found the output of the HgBr medium in this arrangmenet was 0.6 J/l over the 50 cm^3 sampled. This was the same volumetric output as this device

ROLL UP PFN

SIDELIGHT FLUORESCENCE

A: 99 PERCENT OUTPUT COUPLING
(NO LASER EMISSION
OBSERVED)

B: 92 PERCENT OUTPUT COUPLING
(175 mJ → 222 mJ)

C: 70 PERCENT OUTPUT COUPLING
(250 mJ → 325 mJ max)

D: 50 PERCENT OUTPUT COUPLING
(230 mJ → 305 mJ max)

E: LASER EMISSION WITH 50
PERCENT OUTPUT COUPLING

INTENSITY (ARB. UNITS)

50 ns/div
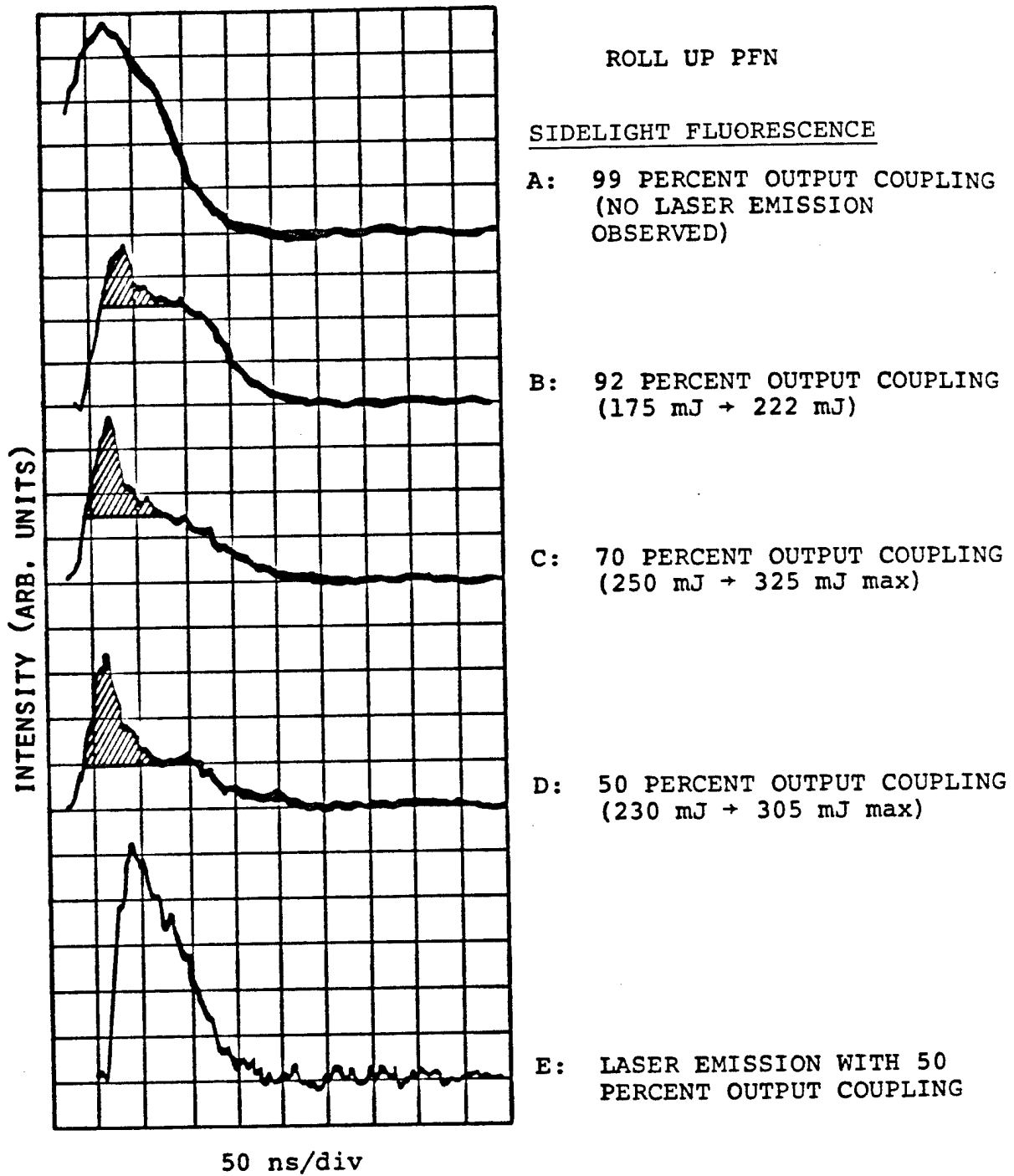
81 04575

Figure 2-8. Potential Extraction Improvement When
Injection Locked or Used as Amplifier

produced when operated as a broad band oscillator. The output was low in these experiments because of window losses. The important finding was that the output of the amplifier contained 67 percent of the energy in the narrow band, and the remainder spread out over the broad input continuum of the dye laser. Figure 2-9 shows the line width of the narrow band emission on two scales and the output of the HgBr laser when operated as an oscillator. The narrow band source can clearly extract energy from both bands, a result that is in keeping with our spectral analysis.

Further work is clearly needed on narrow band extraction of HgBr. These experiments should be repeated with a truly narrow input, i.e., one with a greater contrast ratio of narrow band source to background. This could be achieved by filtering the output of the dye laser. Alternately, the dye laser could be seeded more heavily with a pulsed Ar ion laser.

The use of discrete Ar ion laser lines is convenient. However, there is no necessity that these wavelengths are optimum for extracting the HgBr laser. The variation of output energy with input wavelength and measurements of narrow band extraction should be performed at the greater than 1 J level.

2.3 1 Meter Device Performance

The largest single pulse energy preionized HgBr discharge built to date is our 1 m device. The nominal characteristics of the laser head are given in Table 2-6. The device is constructed with careful attention to materials and pressure capability. The gas sees only stainless steel, ceramic feedthroughs, and AR coated windows mounted at approximately normal incidence. After the 1 m device was essentially fabricated, measurements with our 50 cm machine showed that the use of AR coated windows in contact with $HgBr_2$ was detrimental to laser performance because of window losses. To probe such losses, the 1 m device was equipped with an argon ion laser to measure the reflectivity and round trip losses of the cavity on a daily basis. Also, the gas handling system of the 1 m device was designed to have a separate, valved $HgBr_2$ reservoir so that the system could be evacuated totally when desired. This results in less total $HgBr_2$/AR coated

OUTPUT OF HgBr AMPLIFIER
(x 10 MAGNIFIED 30th ORDER)

|←— 0.007 nm
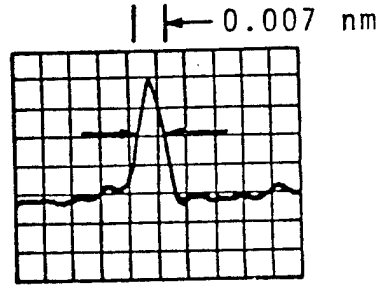
OUTPUT OF AMPLIFIER
(20th ORDER)

3.5 nm

510.7
(496.)
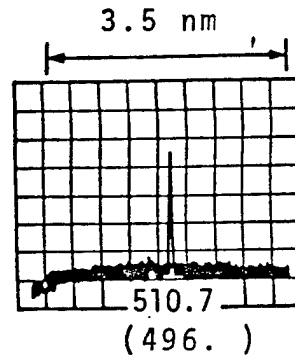
OUTPUT OF FREE RUNNING
OSCILLATOR

.504   502
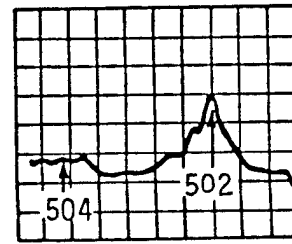
81 04749

Figure 2-9. Narrow Band Extraction Measurements
in 50 cm HgBr Laser.

Table 2-6

Characteristic Dimensions of 1 J Laser

Discharge Length   - 1 m

Discharge Width   - 5 cm possible - dependent on
                             contour
                             3 cm observed at 3.5 cm spacing
                             4.5 cm observed at 5 cm spacing

Electrode Gap   - 3.5 to 6.5 cm

Cavity Length   - 1.5 m

Gas Pressure   - up to 5 atm

Gas Temperature   - 200°C

Materials   - 304 stainless steel throughout
                             with Pyroceram feedthroughs

Overall Dimensions of   - 1.6 m long x 0.33 m wide x 0.53 m
  Laser Head   deep (including high voltage
                             feedthroughs)

window exposure.

The rugged stainless steel construction enables the 1 m cell to be pressurized to roughly twice the pressure of our earlier ceramic and glass tubes. The x-ray window is composed of two annealed stainless foils that are die pressed into a curved shape. The internal window is 15 mils and the external window is 5 mils thick. A vacuum region separates the two foils, and thus the window can operate at either high pressure in the HgBr chamber or at vacuum. The cutaway drawing, Figure 2-10, shows the double foil windows. The x-rays also pass through one electrode. This electrode is pressed in a specially machined die, so that the resultant thin electrode assumes a Chang profile. This ground plane electrode stands up from the ground plane wall by roughly 1 cm. This electrode shape considerably reduces, we believe, the opportunity for extraneous current flow to portions of the ground plane that are outside the useful laser volume. The high voltage electrode is also pressed into a Chang profile from 62 mil thick annealed stainless steel. To date the device has only been run at two electrode spacings, 3.5 and 4.9 cm. No attempt has yet been made to further optimize electrode shape.

A photograph of the device during assembly is shown in Figure 2-11. One sees on the outside of the box a holder for the resonator mirrors. These are attached to the cell by a flexible bellows and are adjustable with a ball and screw three point mount. A vacuum region separates the reflectors and the AR coated chamber windows. The laser head is heated with thermocouple controlled wire resistance heaters attached by tabs spot welded to the laser head. The entire head assembly is contained in a foam glass insulator box that thermally insulates the device from ambient air. A photograph of the internal laser high voltage electrode and ceramic feedthroughs is shown in Figure 2-12. One can see on the lower wall of the laser a Pyrex plate which insulates the lower box ground plane from the electrode. A similar Pyrex plate is attached next to the top wall. High voltage electrical pulses are coupled to the electrode through nine ceramic feedthroughs. The metal walls of the laser head provide the ground return path. This arrangement provides a much lower head inductance than either

CERAMIC HIGH VOLTAGE FEEDTHROUGHS

ELECTRODE

FOIL ELECTRODE

WINDOW

X-RAY WINDOW

SIDELIGHT FLUORESCENCE PORT

1 m GAIN LENGTH HIGH PRESSURE STAINLESS STEEL BOX

$5A/cm^2$ COLD CATHODE E-BEAM/X-RAY SOURCE
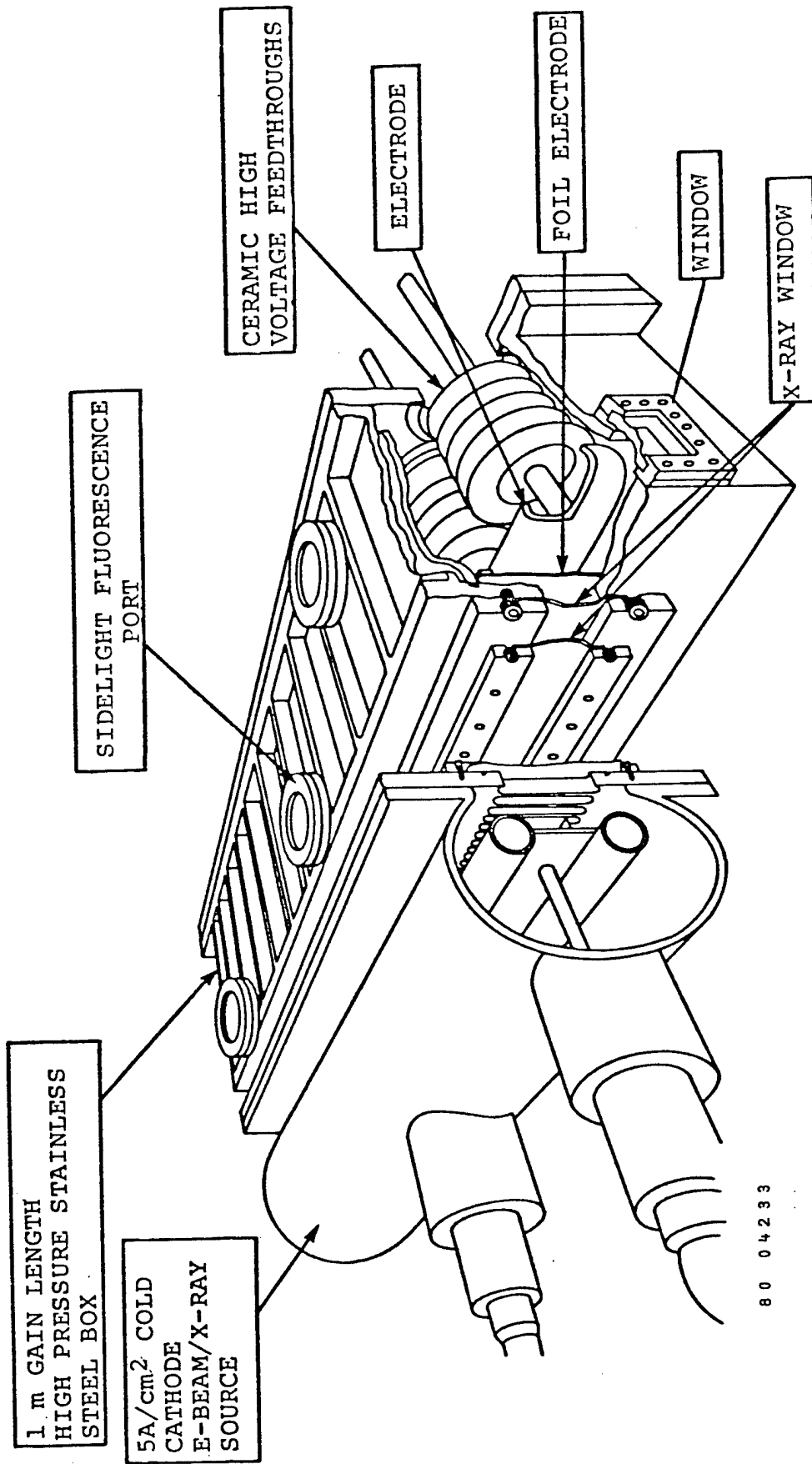
80 04 2 3 3

Figure 2-10.   Schematic Diagram of 1 J Device.
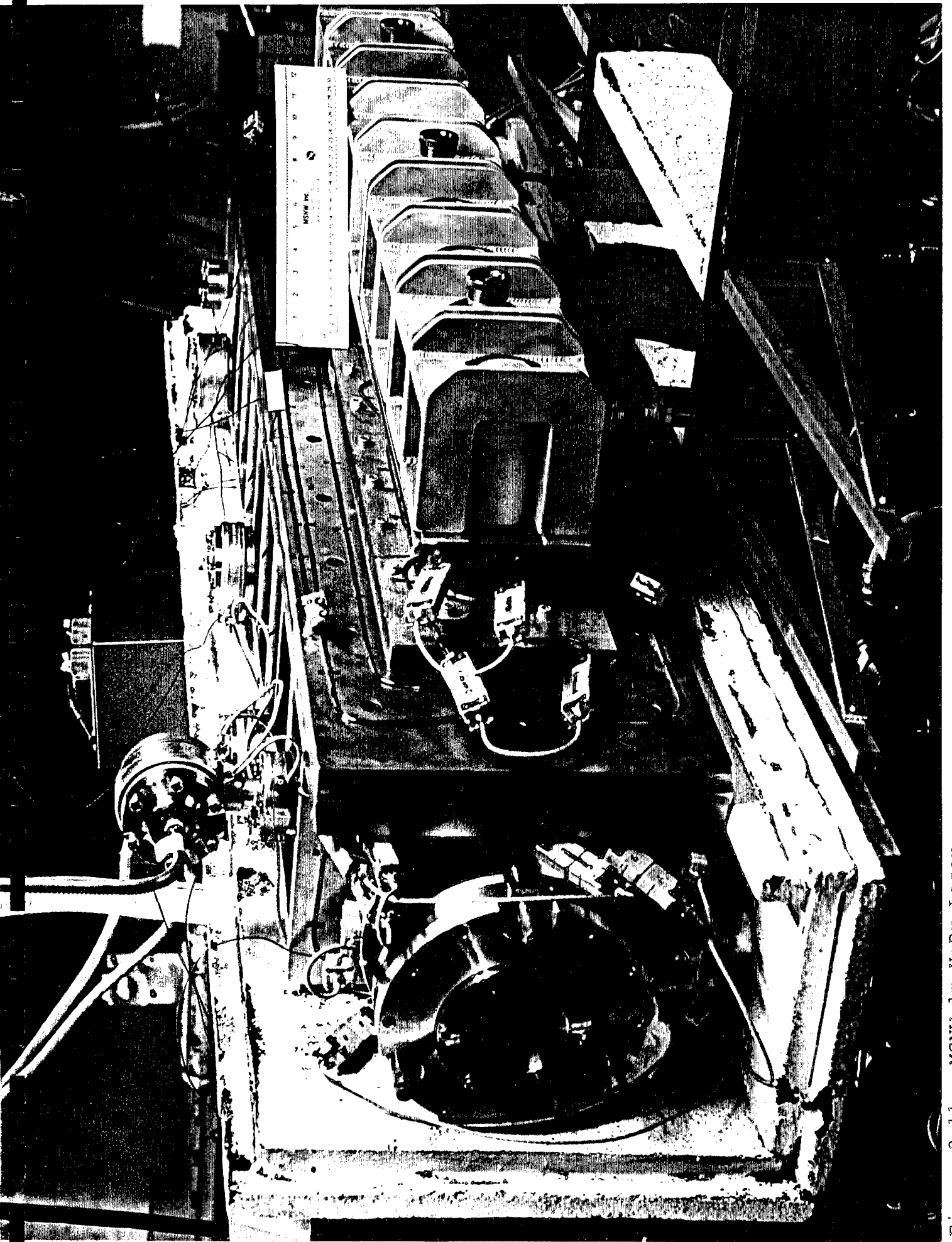
Figure 2-11. MSNW 1m HgBr Laser
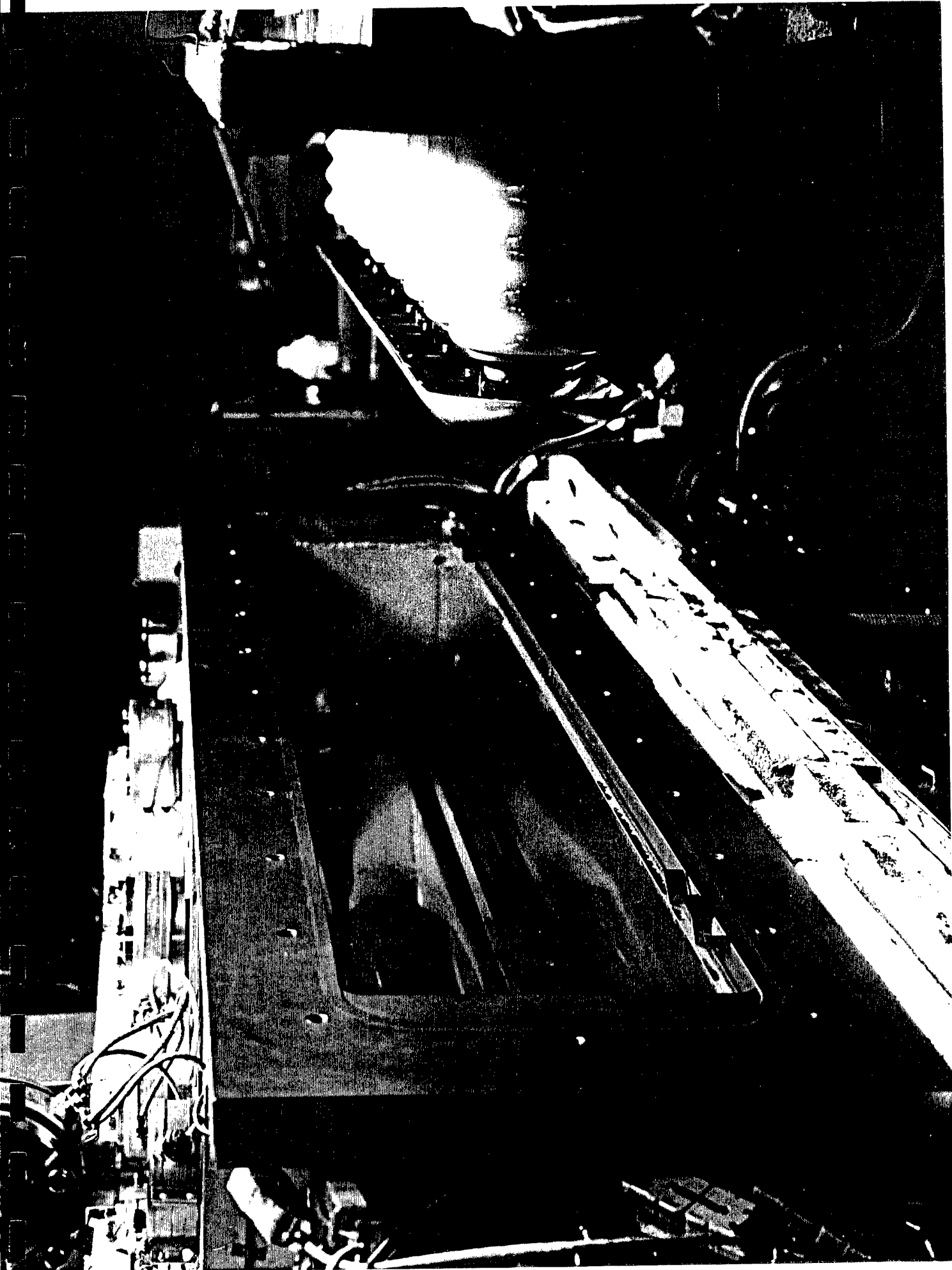
Figure 2-12. Inside View of MSNW 1m HgBr Laser

of our smaller lasers discussed previously. Measurements of the head inductance by an L-C ringing circuit show it to be of order 12 nanohenries.

The electrical pulser for this device is a pulse charged rolled up copper sheet/polyethylene capacitor/transmission line. This capacitor, termed a rollup line, has a nominal I-V pulse length based on stripline length of order 100 ns and a measured capacitance of 70 nF. This capacitor was resonantly charged in two distinct modes: rapid ~300 ns, and slow ~3 µsec. In the rapid charge mode energy from the charging circuit could flow into the laser during excitation. In the slow charge mode energy in the L-C charging circuit when the capacitor is fired can not contribute to the 100 ns pump pulse. Three output switches were used: a nontriggered railgap, an electrically triggered railgap and an Exci-Lite[TM] uv triggered railgap. The railgap is shown in Figure 2-13. Figure 2-14 gives a schematic of the circuit.

The efficiency of the 1 m system can be measured relative to several points in the circuit given in Figure 2-14. If we define the overall laser efficiency as output energy ratioed to energy stored on the capacitor C_1 used to charge the rollup stripline, C_2, our best efficiency is 0.91 percent for either fast or slow charging of C_2. Analysis shows that a major loss in energy occurs in the charging of the intermediate capacitor. Roughly 35 J of the 125 J initially stored is lost in the pulse charging switch or possibly in losses on the rollup itself or due to connections between the capacitor C_1 and C_2. These energy loss measurements were based on voltage measurements, but were correlated by simple calorimeter measurements of the energy extracted from the roll-up capacitor/line. This loss would not occur in a properly engineered resonant charging circuit.

In order to analyze the losses in the resonant charging circuit we performed an experiment in which we let C_1 ring into C_2 and followed the voltage damping on successive cycles. The capacitor C_1 was charged to 50 kV and switched into C_2. The voltage and current flowing in the circuit shown below was monitored using
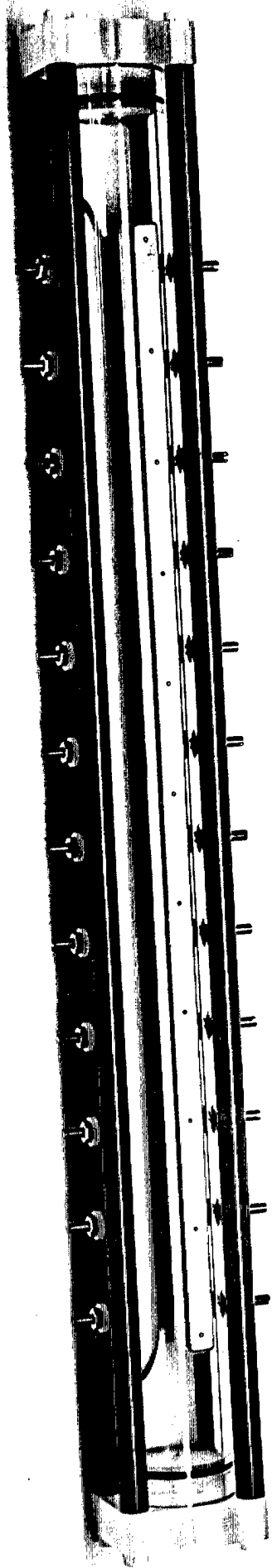
Figure 2-13. Multi-Channel Rail Gap
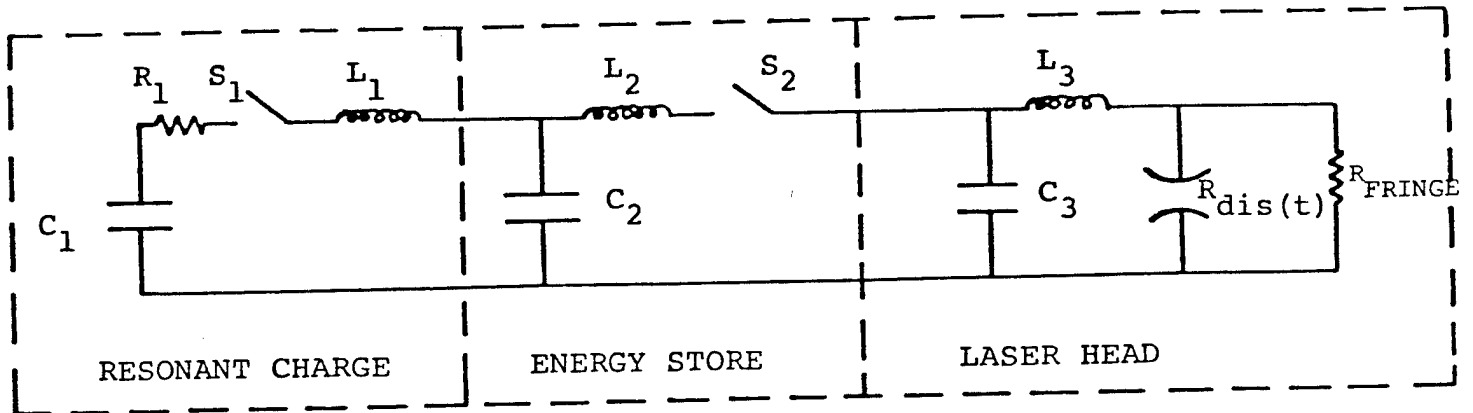
81 04924

Resonant Charging Circuit

$C_1 = 0.1\mu F$

S_1 a single channel spark gap

R_1 resistance of connections (~2Ω)

L_1 ~ 1.4μH charging inductor-fast charge

~ 15μH slow charge

Energy Store

C_2 ~ 70 nF stripline

L_2 ~ 70 nH

S_2 "multichannel" output switch

C_3 ~ 7.7 nF stripline transition section

L_3 ~ 12 nH head inductance

Figure 2-14. 1m Device Circuit Schematic.
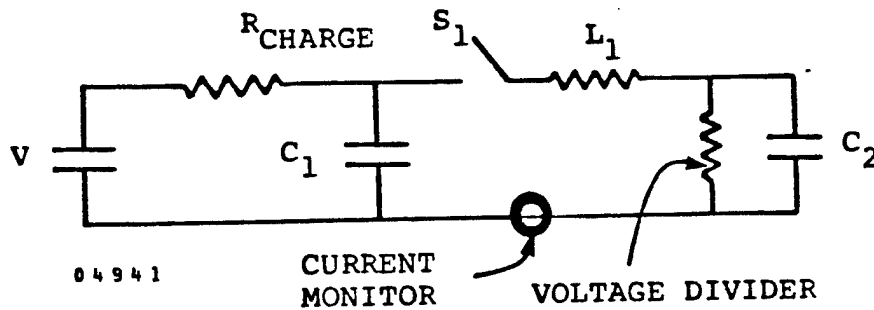
calibrated current and voltage probes. The loss on the nth successive cycle is given by

$$\Delta \frac{E_n}{E_{n-1}} = 1 - \left(\frac{V_n}{V_{n-1}} \right)^2$$

Thus measurement of voltage on successive cycles can give ΔE. Figure 2-15 shows the I and V traces and the fractional energy loss in the circuit per cycle on this analysis. The losses stabilize at about 6 percent per cycle after about 6 cycles, and these are resistive losses in the RLC circuit. The "extra" losses during the first 5 cycles are due to the resistive switch, capacitor mismatch or corona in the PFL. During the first half cycle, the period which is used to charge C_2 for a laser experiment, the net losses are 32 percent. These losses are distributed roughly at 25 percent into switch or capacitor loss, 3 percent into resistive connections and 4.5 percent due to the mismatch of C_1 and C_2. This latter energy loss, given by

$$\frac{E_2}{E_1} = 1 - \frac{4\, C_2\, C_1}{(C_1 + C_2)^2}$$
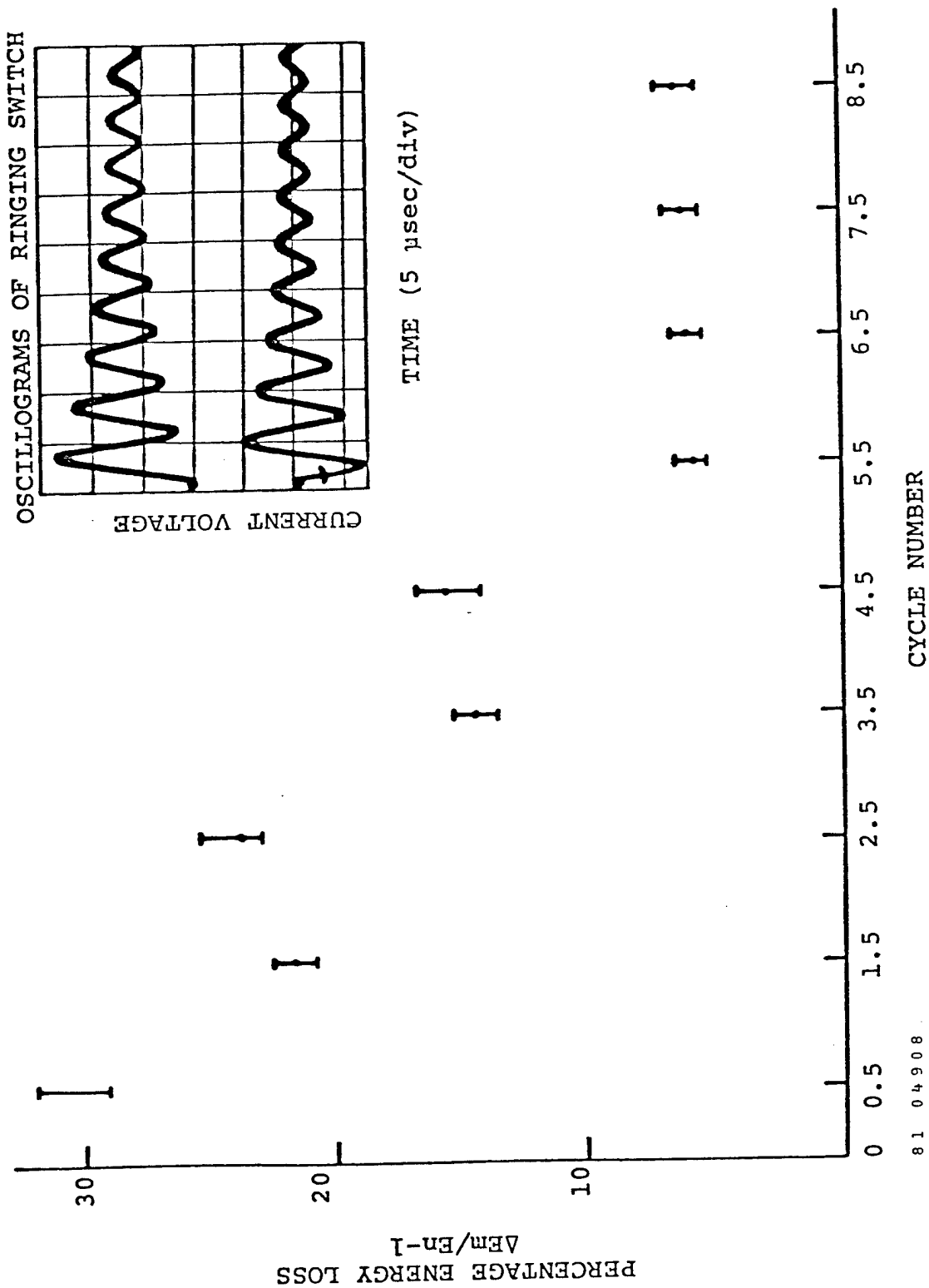
Figure 2-15. Energy Loss in Pulse Charging Switch.

is minor compared to the switch or capacitor losses. The losses above apply to slow charging through this switch. Roughly similar energy losses (~25 percent) apply to rapid charge experiments.

An alternative analysis of the charging losses that is not dependent on voltage monitor calibration can be obtained from the damping of the charging current shown in Figure 2-16. The current for a damped RLC circuit is given by

$$i(t) = I_o \exp\left(-\frac{Rt}{2L}\right) \sin\omega t \qquad ; \qquad \omega^2 = \frac{1}{LC}$$

where $\frac{1}{C} = \frac{1}{C_1} + \frac{1}{C_2}$ and L is the inductance between C_1 and C_2. Figure 2-16 shows a semilog plot of the relative amplitudes of successive current maxima. Except for the first maximum, the plot is reasonably well fit by a straight line with a slope giving R/2L. The inductance L was estimated from the ringing frequency and the known capacitances to be L = 15.4 μH. This yields a damping resistance of 2.4Ω , which is quite large. Using the above formula for the current and integrating the resistive losses for the first half cycle indicates that 17 J is lost in this resistance, in reasonable agreement with the previous analysis.

Most of the experimental data was obtained with the slowly charged line. To present the bulk of our data on the 1 m device we define efficiency as the output energy ratioed to energy stored on C_2 for a slow pulse charge. This efficiency includes one major loss, energy loss in the output switch. From current and voltage traces taken on the laser side of the output switch we find that roughly 30 percent of the energy stored on the capacitor C_2 is lost in the output switch S_2. This is most likely due to the fact that the railgap is operating with only a few channels, if multichannelling at all. Figure 2-17 gives the typical energy flow and loss for an experiment on the 1 m device with a 3.5 cm electrode spacing that yielded 930 mJ output, corresponding to 1.1 percent efficiency relative to C_2, 0.75 percent efficiency relative to the storage capacitor C_1 and 1.6 percent laser head efficiency. This is a result that is typical
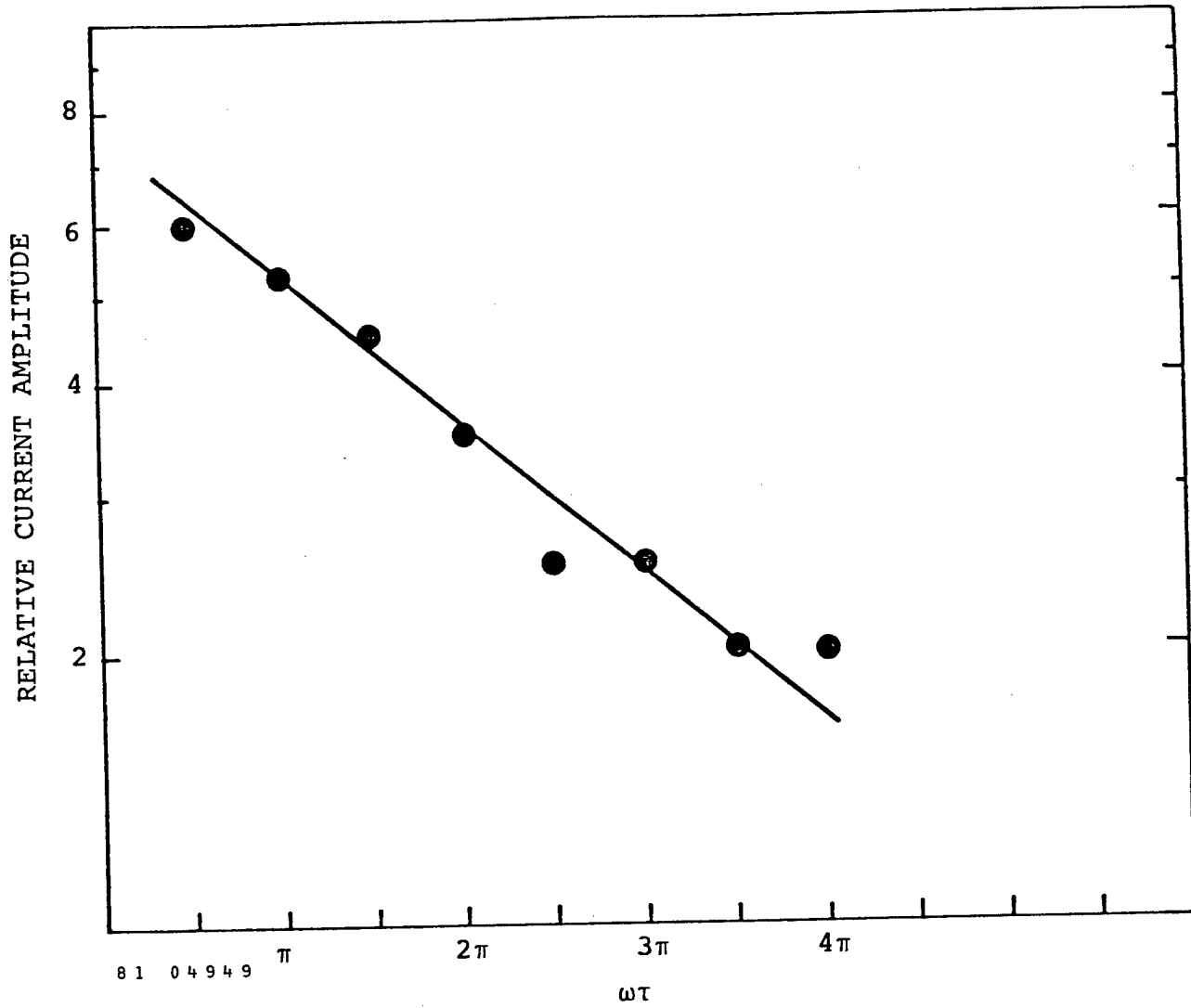
Figure 2-16. Analysis of Charging Current Damping.
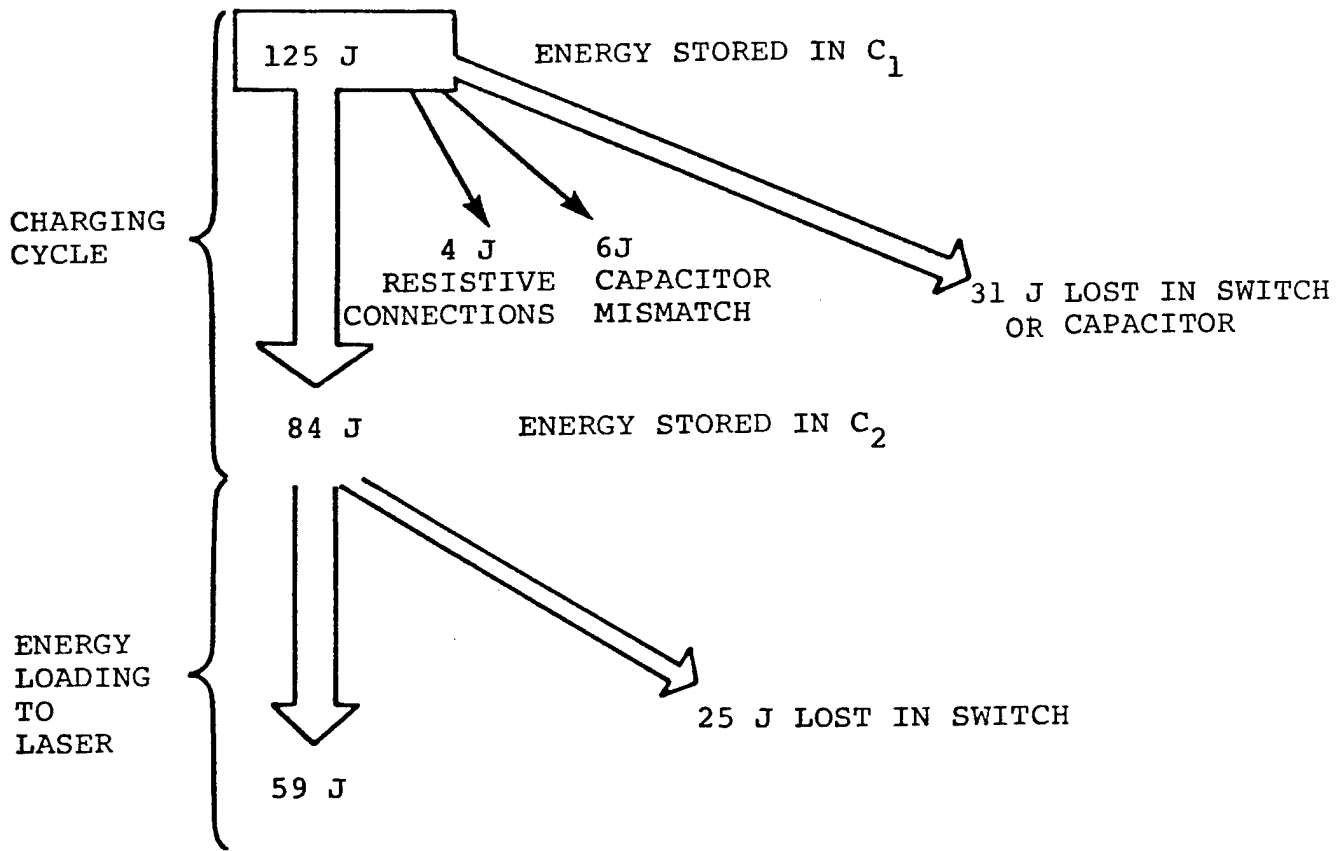
Figure 2-17. Typical Energy Losses in Current 1m HgBr Laser.

for a strongly excited HgBr medium, i.e., one that produces about 1 J/liter output. In keeping with our prior experience with the 50 cm device and results at NOSC, we find higher overall efficiencies at lower energy densities and power deposition rates. We have achieved with a 3.5 cm spacing 750 mJ outputs with only 55 J stored on C_2, corresponding to 1.3 percent efficiency relative to C_2, and 1.8 percent efficiency relative to the energy remaining after the output switch.

Figure 2-18 shows a typical current and voltage waveform for the 1 m laser: 2-18a showing the fairly flat current pulse achieved with Ne/N$_2$ mixtures, and 2-18b showing one pertaining to a lasing mixture, using 10 percent N_2 and 6 torr $HgBr_2$. The current remains fairly steady but the voltage undulates, impressing an undulating power pulse on the laser mixture. This HgBr electric driver is the first one built at MSNW which has sufficiently low head and line inductance to translate these power pulses into the laser medium with high fidelity. The result is a fluctuating laser signal.

A typical set of oscillograms is shown in Figure 2-19. This is typical output at 4.9 cm electrode spacing in 4 atm Ne with 5 torr $HgBr_2$. Here we record the charging voltage on the rollup, which reached a peak value of 57 kV, the total current and laser intensity and voltage and current traces for the pulser driving the laser. The rapid temporal fluctuations in laser intensity are seen, as is the fairly rapid turn on. After breakdown the current is relatively constant for 100 ns. There are subtle differences in current temporal shape depending on the point along the railgap that is monitored. The laser pulse duration FWHM is about 150 ns. The single pulse energy was 1.4 J as measured on our surface absorbing calorimeter. The laser pulse begins to fall in intensity when the voltage begins to drop, presumably because C_2 is close to fully depleted. There appears to be no evidence that lasing is terminating before power drops off, or that the discharge is becoming unstable. Thus it is realistic to project that slightly higher energy densities can be achieved by stretching the pump pulse duration at constant power loading.
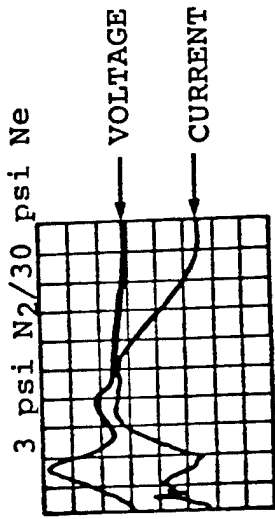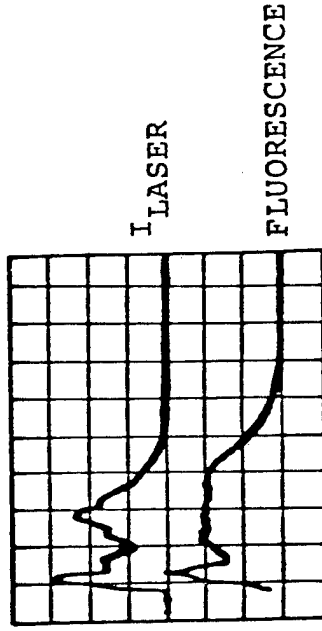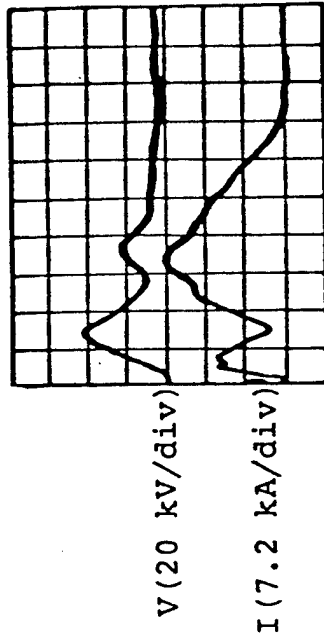
Figure 2-18. Typical Waveforms of 1 m Device.

CHARGING
VOLTAGE
ON ROLLUP
20 kV/div

0.5 µsec/div

TIME

CURRENT AT
PROBE AFTER
S_2 $\dfrac{7.2kA}{DIV}$

LASER PULSE
INTENSITY

50 ns/div

TIME

VOLTAGE

$\dfrac{20kV}{DIV}$

CURRENT $\dfrac{7.2kA}{DIV}$
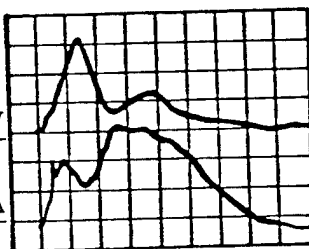
TIME

81 04927

Figure 2-19.   Typical Oscillograms for a 1.4 J
   Pulse in $Ne/HgBr_2$.

Figure 2-20 shows another set of oscillograms for a 4 atm Ne/HgBr$_2$ mixture at a 5 cm electrode spacing. The main differences between this shot and that presented in Figure 2-19 is that the HgBr$_2$ pressure was increased to 10 torr and the output mirror was changed to an uncoated flat (R~8 percent). The effect of higher HgBr$_2$ pressure is to decrease the discharge impedance; the current is about 30 percent higher and the operating voltage is substantially lower than for the lower HgBr$_2$ concentration shot shown in Figure 2-19. The voltage on the rolled up line reached 56 kV for this shot which produced 1.63 J of laser energy. This corresponds to an efficiency of 1.5 percent. The 0.1 µF storage capacitor was charged to 60 kV giving an overall efficiency of 0.9 percent. In spite of this high efficiency and high output energy, the laser pulse duration is only about half that seen, with the lower HgBr$_2$ density shots (Figure 2-19).

Figure 2-21 shows the effect on laser performance of increasing the electrode spacing from 3.5 to 5 cm. The gas mixture for both spacings was Ne/2.5 percent N$_2$ but the total pressure was reduced for the 5 cm gap data in order to work at similar voltages. The 5 cm gap gives higher energies and efficiencies, especially at higher charging voltages.

Figure 2-22 shows the HgBr laser performance for two Ne pressures and for a Ne/2.5 percent N$_2$ mixture at the 5 cm electrode gap. This data was taken with a relatively low HgBr$_2$ pressure (~5 torr) and an R = 30 percent output mirror. A carbon paper burn taken at the laser output mirror measured 4.5 cm x 4.5 cm. The pure Ne mixtures gave higher output energies and efficiencies, and increasing the Ne pressure from 3 to 4 atm further improved the performance.

Figure 2-23 shows similar data taken with higher HgBr$_2$ pressure (~10 torr). Increasing the HgBr$_2$ pressure increases both the output energy and the efficiency. The effect on discharge impedance and laser pulse shape was previously mentioned in connection with Figure 2-20. The data in Figure 2-23 show the same trend of improving performance with increasing Ne pressure. Also apparent from Figure 2-23 is that higher output coupling gave slightly increased performance. It is evident from the data presented

CHARGING VOLTAGE
ON ROLLUP
CAPACITOR
(20kV/div)
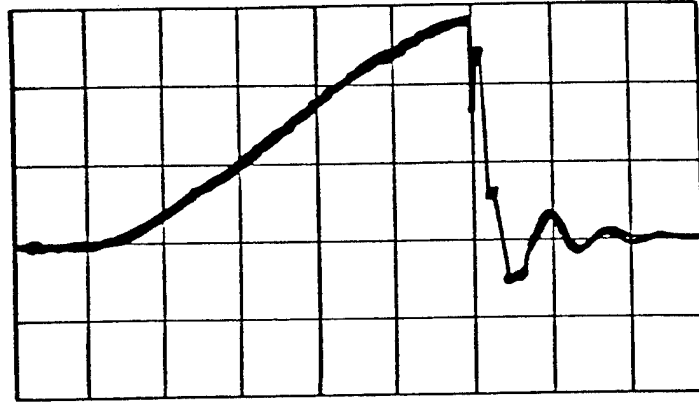
→| |← 0.5/usec/div

VOLTAGE
(20kV/div)

CURRENT
(7.2kA/div)

LASER INTENSITY
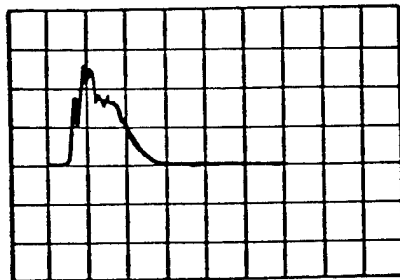
81 04946

Figure 2-20.   Typical oscillograms for a 1.6 J
               HgBr laser pulse in Ne/HgBr$_2$.
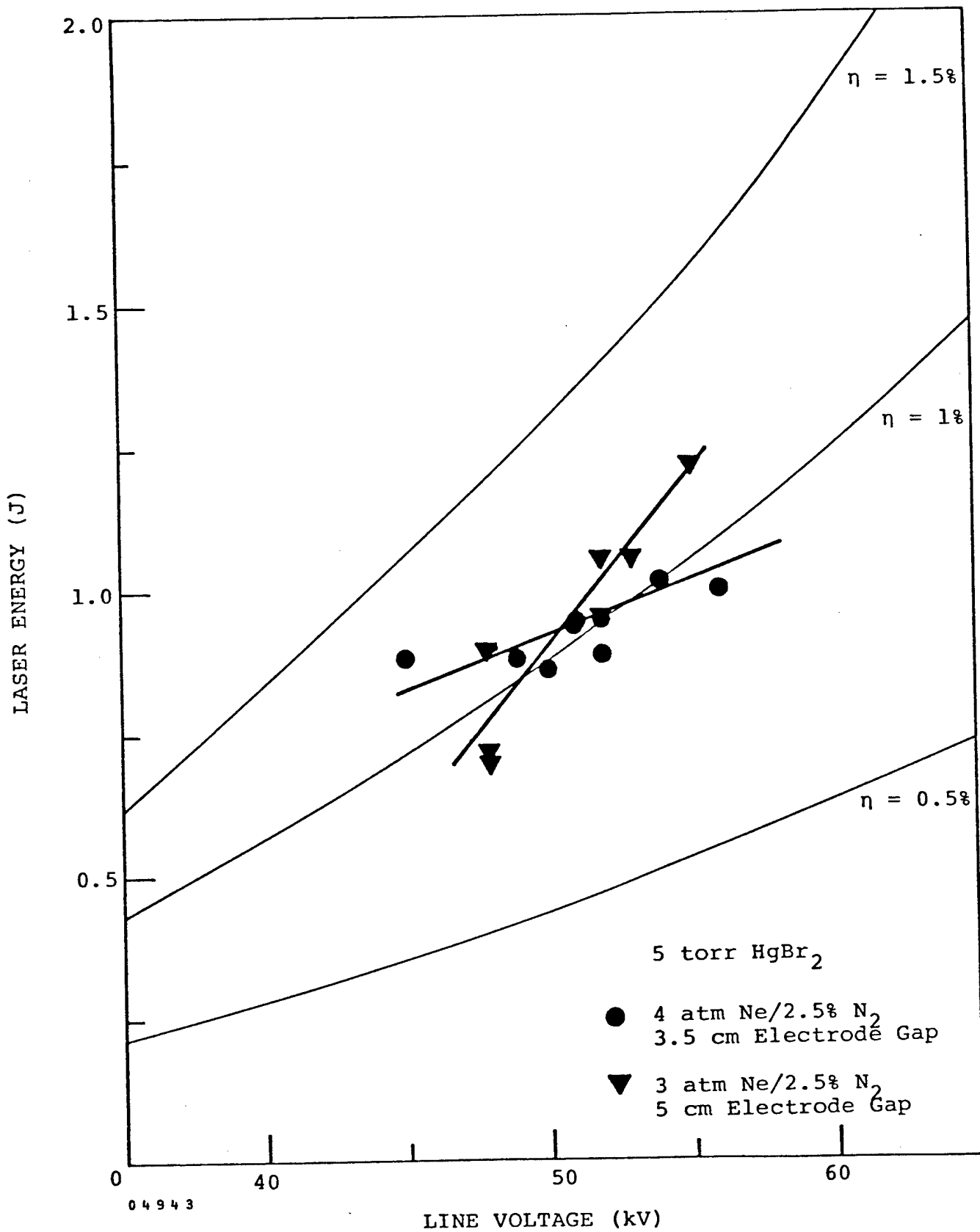
Figure 2-21. Comparison of HgBr laser performance for
3.5 and 5 cm electrode gaps.
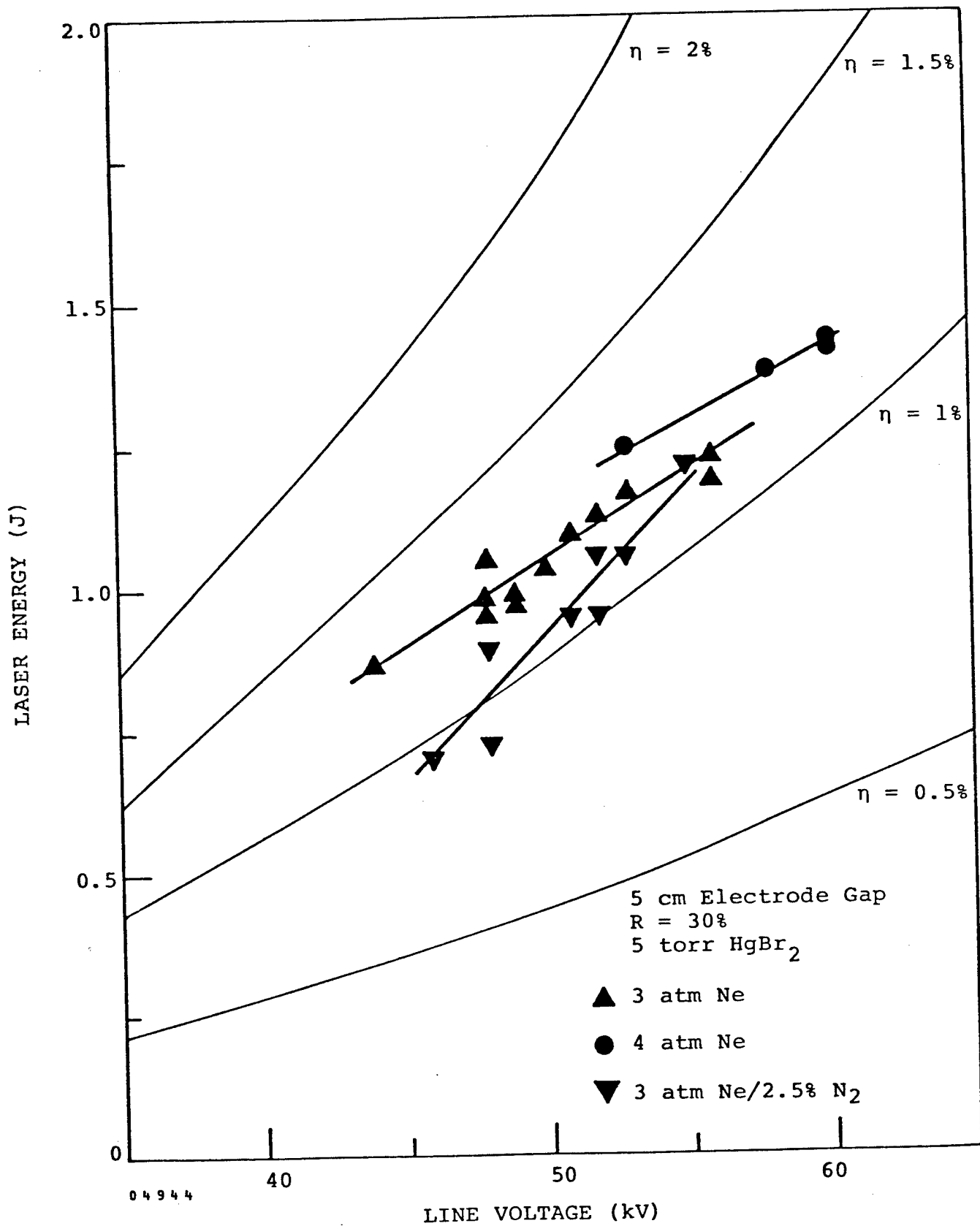
Figure 2-22. Comparison of HgBr laser performance for Ne and Ne/N$_2$ mixtures.
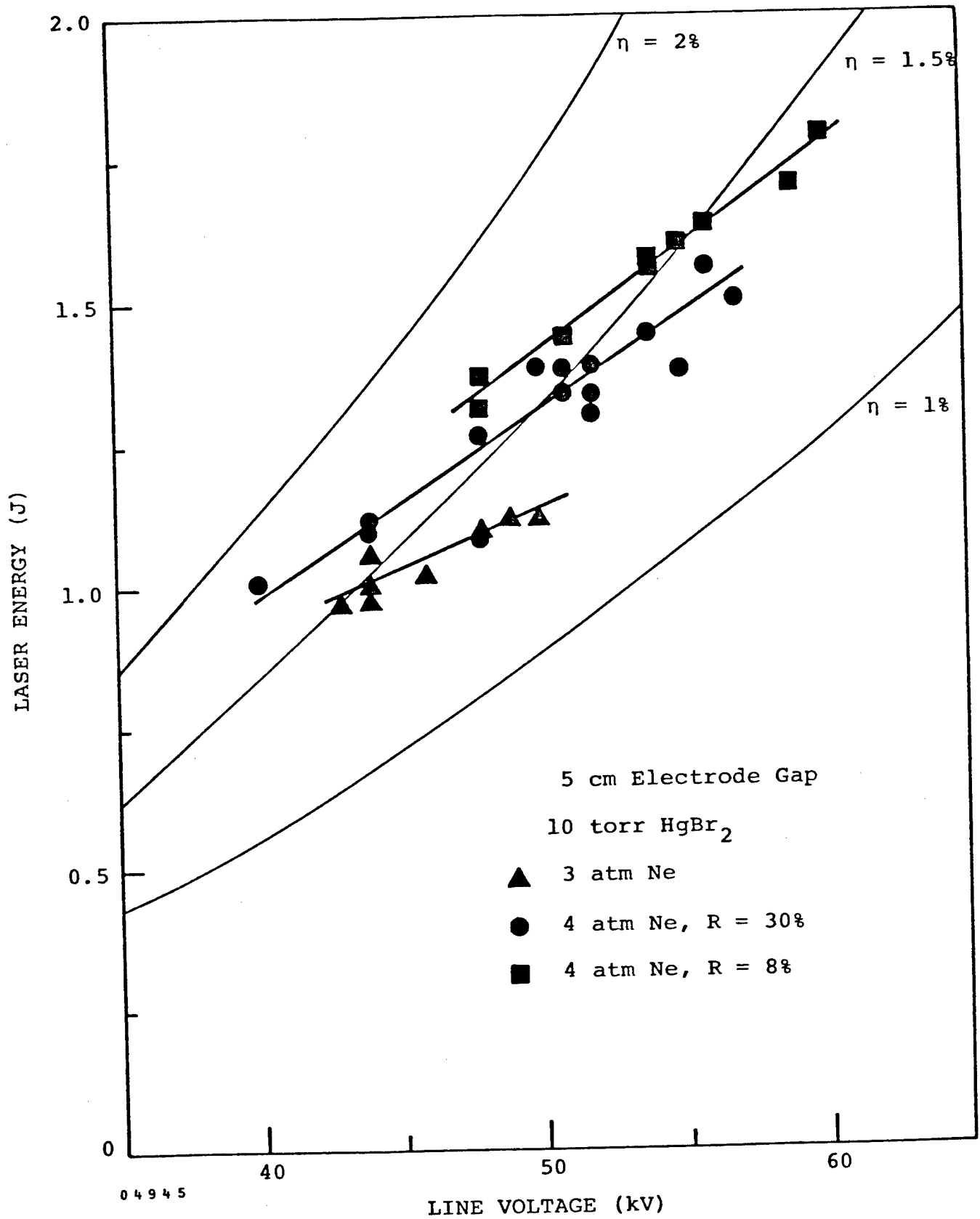
Figure 2-23. HgBr laser performance as a function of charging voltage for Ne mixtures.

that output energies of greater than 1.5 J at efficiencies greater than 1.5 percent were readily obtained from the nominal 2.25 liter discharge volume. Higher energies could undoubtedly be achieved with higher charging voltages, although probably at some sacrifice in efficiency.

REFERENCES

1. Mathematical Sciences Northwest, Inc., Scaling Studies for Mercury Bromide Lasers, Contract No. N00014-80-C-0245 (Prepared for Office of Naval Research), April 1981.

Section III

MODELING

Several codes are in use for modeling our existing laser heads. For media and circuit modeling the most important codes are the electron transport Boltzmann code, the coupled laser kinetics/circuit code, multi-pass amplifier codes for expanding geometries, a parasitic code, and rapid circuit analysis code (Spice) which uses estimates of the time varying load impedance to optimize pulser design.

The post pulse chemical kinetics is modeled separately using as input the final species concentrations from the laser code. Postpulse media chemistry is discussed with the flow loop. Straightforward analysis of x-ray generation, transmission and deposition is used to predict the preionization level achieved in the media without resort to any sophisticated code calculations. Estimates of minimum preionization level required are taken from the analysis of Lin and Levatter[1] and our own experimental results.

For laser head design and the interpretation of our own and other single pulse experiments, the work horse code has been that which couples media kinetics and pulsed power. This code includes cavity flux buildup from noise or an injected level. The effects of losses, both in windows and saturable and nonsaturable losses in the medium are included. The specific identity of absorbers other than Br_2, dust, and window loss are not known. The rate constants and proceses used in this model are tabulated in Appendix A. An input to this code is a curve fit of results of energy partitioning and rate constants calculated from solution of the Boltzmann electron transport equations as a function of electric field strength. Typical output of our Boltzmann code, shown in Figure 3-1 for a $Ne/N_2/HgBr_2$ mixture having 6 percent N_2 and 6 torr $HgBr_2$. Similar plots are available for a wide range of $Ne/N_2/HgBr_2$ composition. The graph shown is for a Boltzmann code calculation in which the direct formation of $HgBr^*$ by the process
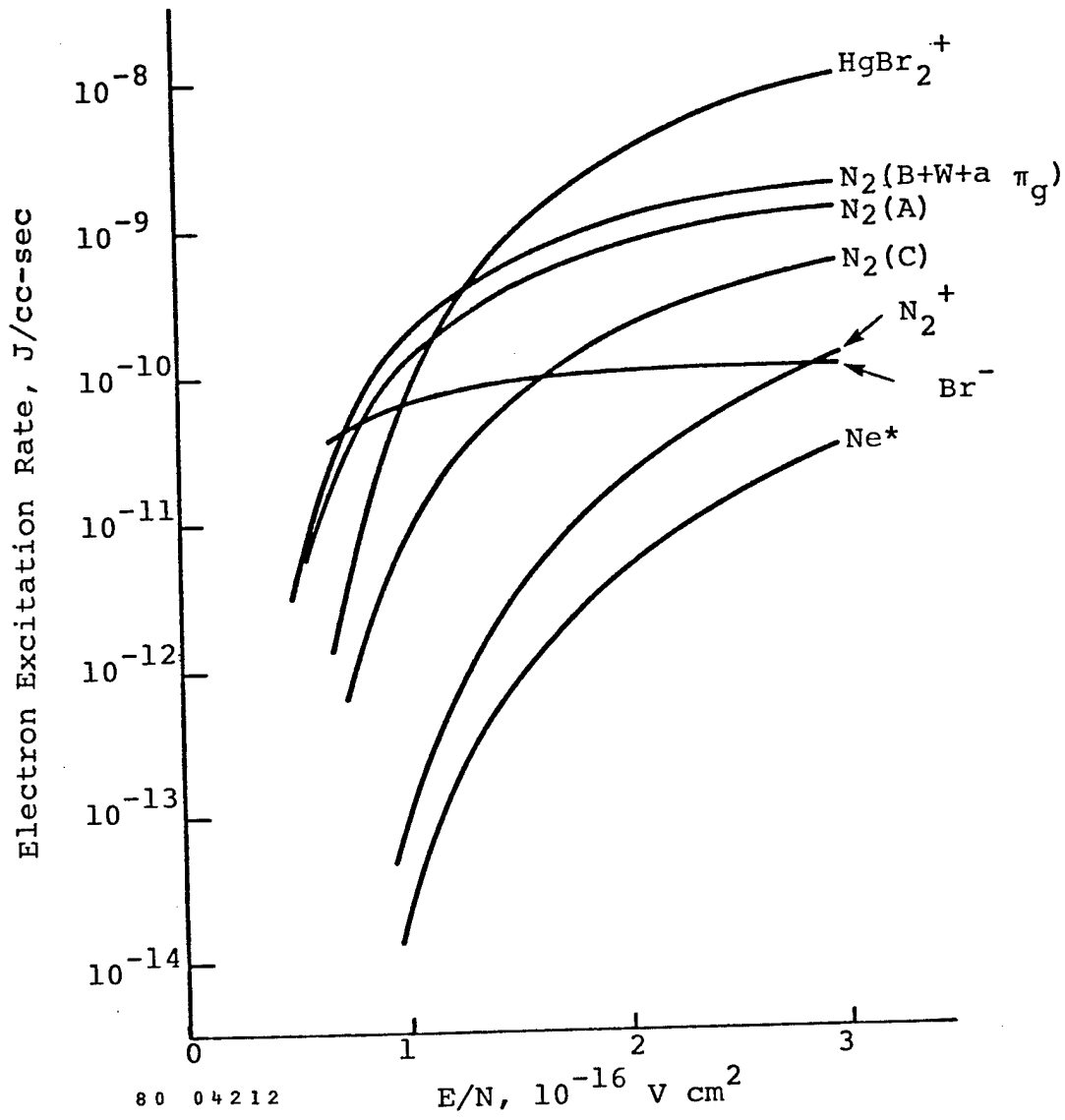
Figure 3-1. Boltzmann code results for 6% N_2, 0.25% $HgBr_2$.

$$e + HgBr_2 \rightarrow HgBr^* + e$$
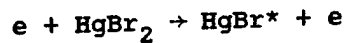
is neglected. We have also produced similar plots for the case where HgBr* direct formation is allowed to proceed. Figure 3-2 shows the excitation rates for a Ne and $HgBr_2$ mixture in which the direct pumping of $HgBr_2$ to HgBr(B) is based on an assumed cross-section 1×10^{-16} cm^2 with a 6 eV threshold. Recent results on our 1 m device at very low and zero N_2 mole fractions have shown that this direct process must be included in the modeling.

To predict lasing performance in a preionized discharge, one must input to the coupled laser chemistry code the functional time dependence of the E/N that the pulser/laser head produces. This can be done in two ways. Primarily we solve in a self consistent fashion the circuit differential equations and the laser media chemical kinetic differential equations. We also can input the E/N profile from measured or predicted pulsers directly into the laser media model, although this method is not used routinely. Figure 3-3 shows a typical circuit modeled, in this case the L-C inversion circuit of the NOSC 55 cm device.[2] The circuit code allows for a time dependent switch resistance. Moreover, the code includes the provision for a time dependent gas impedance in parallel with the main discharge to account for fringing currents, i.e. current flow outside the laser active medium.

3.1 Code Validation and Application

To validate the code we modeled the NOSC 55 cm HgBr laser. This laser has a 55 cm gain length and 80 cm resonator spacing. Because of the strongly curved electrodes on this device, we assume a fringing current $I_f(t) = 2\% \, I_{DIS}(t)$. Figure 3-4 shows the current and voltage traces predicted by our model for the NOSC device (see Figure 3-3 for the definition of V_1 and V_2). The model used in predicting these experiments uses an N_2^* transfer mechanism only. The total current flowing in the system is predicted well, although the voltage may be somewhat high. Reduction of NOSC data implied a value of V_2 of 6.1 kV, at the peak
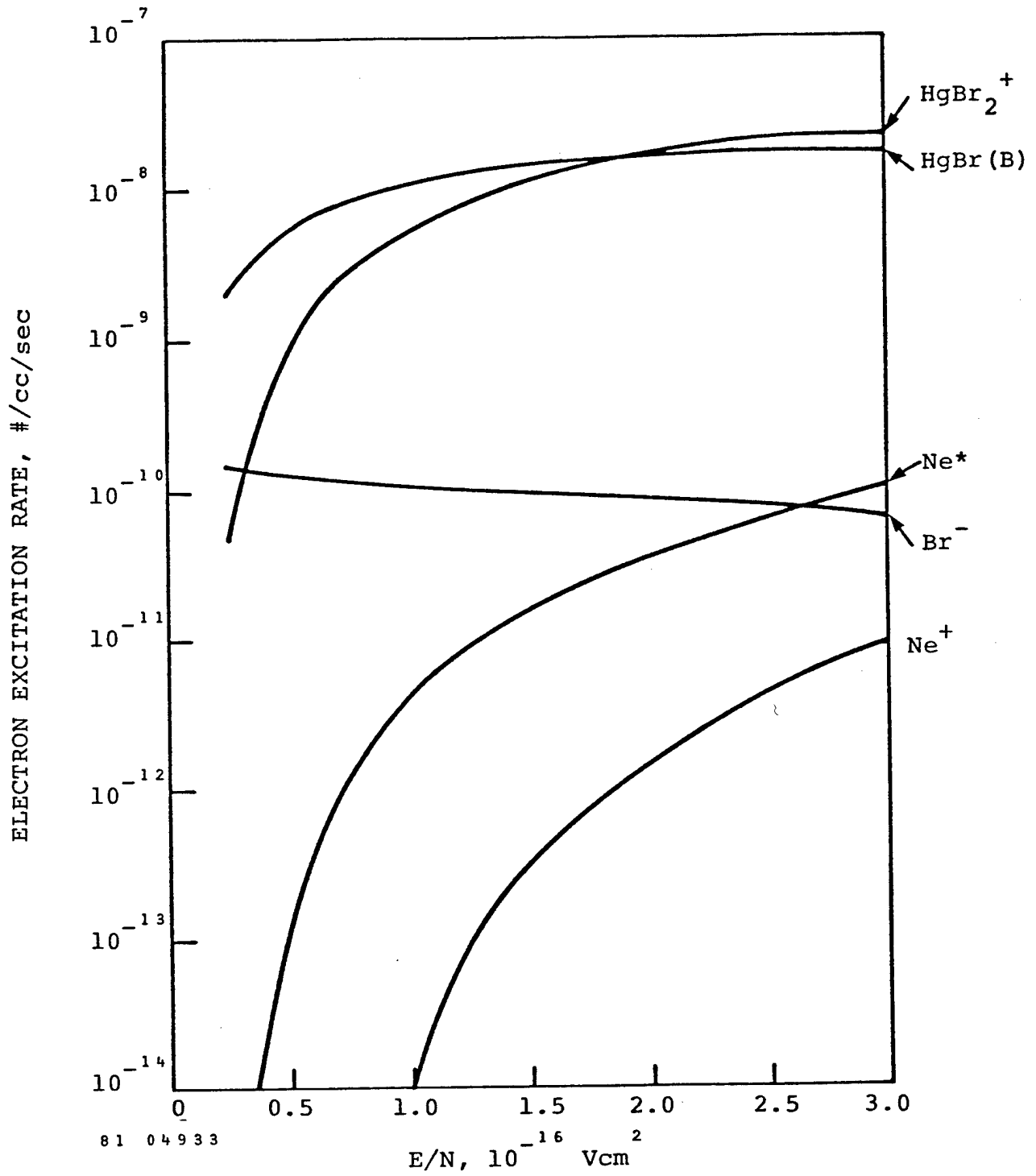
Figure 3-2. Boltzman solution for Ne + HgBr$_2$ (0.25%).
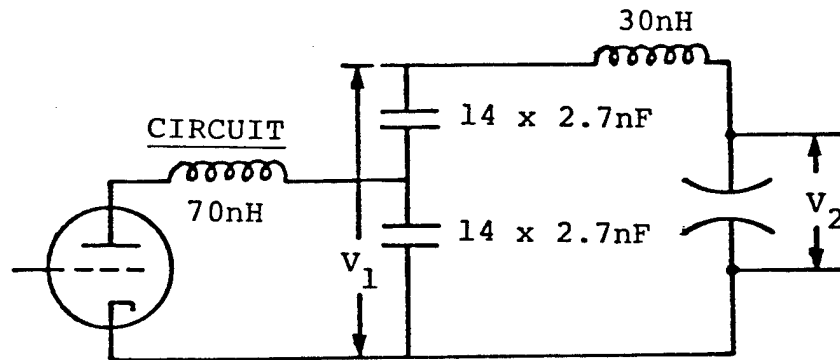
81 04814

Figure 3-3. Model of NOSC experiments.

2.7 torr HgBr$_2$
25 torr N$_2$
1000 torr Ne
12 kV charge
4.84 J Stored

VOLTAGE V$_2$ at
PEAK CURRENT

NOSC CALC - 6.1

MSNW Code - 8.8

CURRENT
--- NOSC EXPERIMENT
— MSNW CODE

VOLTAGE V$_1$

V$_2$

Voltage (kV)

Current (KA)

Time (20ns/Division)

81 04815
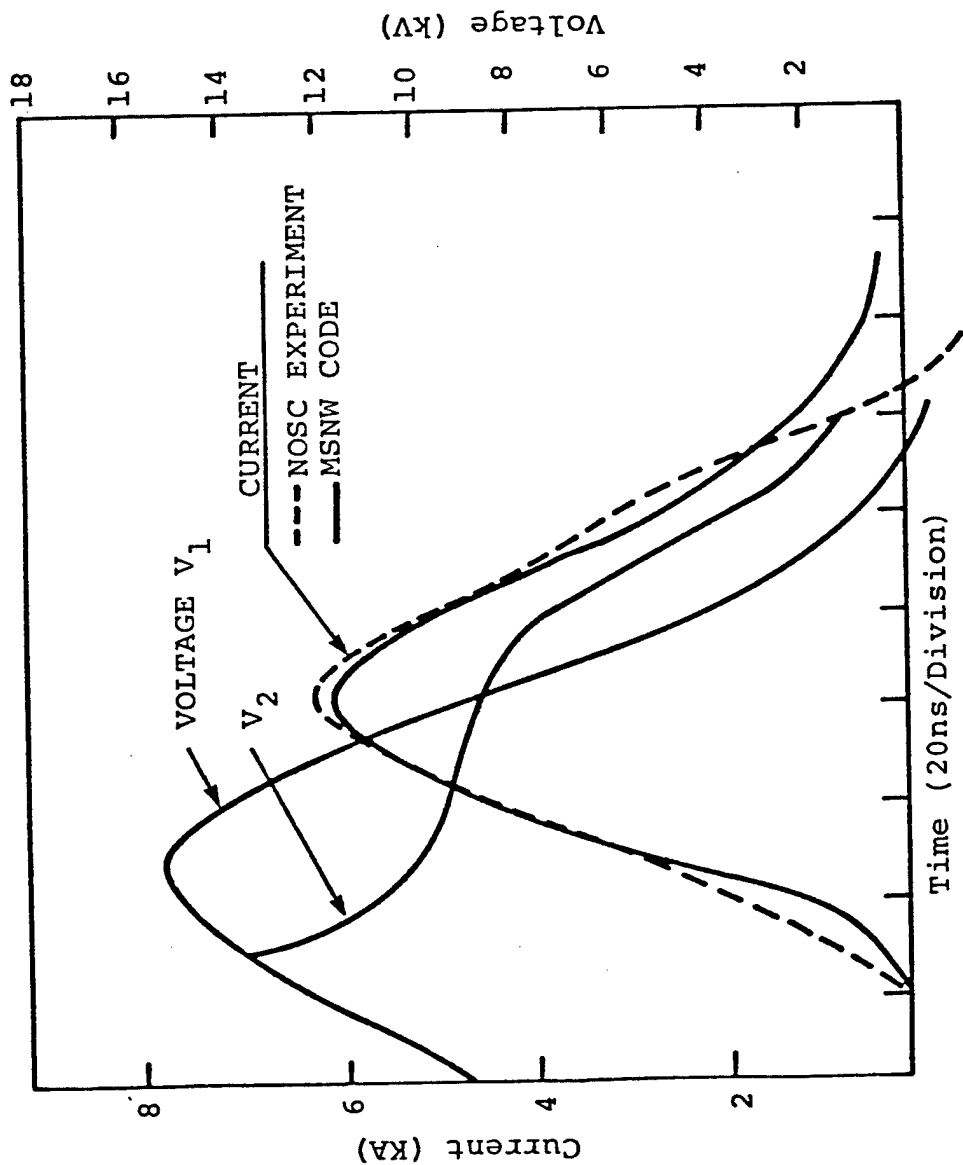
Figure 3-4. Current - Voltage waveforms from model.

current, while our code predicted 8.8 kV. Prediction of the gain, single pulse energy and peak current for the NOSC device are in reasonable agreement, (see Table 3-1). Energies slightly higher than the experimental result are found, probably due to the overprediction of V_2. The model also predicts the gain as a function of input energy. This is shown in Figure 3-5 and the predicted values are in good agreement with the NOSC data.

The same code was then used to model the MSNW 30 and 50 cm HgBr devices. The model predictions, based on measured values of capacitances of driver and head, the head inductance and the active lasing volume clearly shows that the sub optimum laser performance of these devices is due to factors relating to laser pulser and head design rather than the medium. Using a low value of the fringing current ratio $I_F/I_{DIS} \sim 2\%$, the model predicts that both devices should have produced twice or more the single pulse energy observed. This implies that there is some other unaccounted "efficiency loss" mechanism operating in the smaller devices. The 30 cm device results were complicated by gas impurities, electrode corrosion, light scattering due to dust, window losses and short gain length. The 50 cm device was however basically very similar to the NOSC device in terms of purity, gain length, and dust level. One important difference was electrode shape. One postulate is that the electrode contours in our laser allow for extraneous current flow. We have made an estimate of the effects of extraneous current in the MSNW 50 cm device. Figure 3-6 shows how the single pulse energy depends on extraneous current flow, expressed as the ratio of fringe current to discharge current. A total fringing current in the 50 cm device in the range of 25 to 40 percent drops the predicted output energy into the range of experimentally observed energy.

The laser kinetics/pulser model has been applied to the 1 m, 1.75 J laser. Because of the low impedance driving circuit, fluctuations in pump power were rapidly transmited to the discharge. This results in the laser intensity rapidly fluctuating , an effect not observed experimentally in our smaller devices or in the NOSC laser. Using the N_2 energy transfer mechanism[3] that modeled our slower pulsers/lasers, we fail to replicate the

Table 3-1

Comparison of Code and Model for
1000 Ne, 25 torr N_2, 2.7 torr $HgBr_2$, 5 J Stored

	NOSC Experiment	MSNW Model
Peak Current	5.6 kA	5.5 kA
Voltage at Current Peak	6.1 kA (calculated)	8.8 kA
Small Signal Gain	6.5%	6.5%
Single Pulse Energy		
No injection	50 mJ	63 mJ
Injection	65 mJ est.	73 mJ
Efficiency - No injection	1%	1.2%
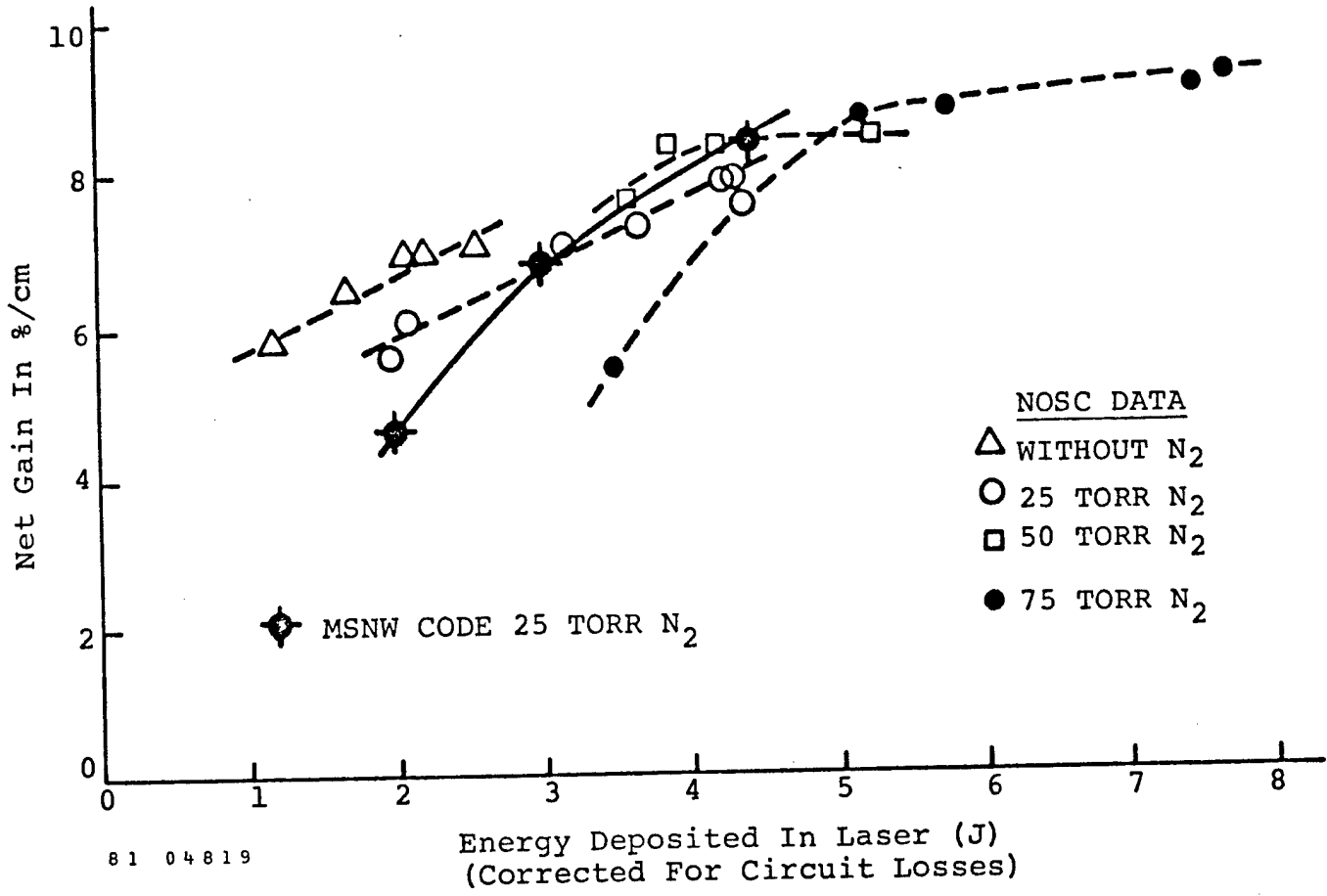
Figure 3-5. Comparison of code and NOSC gain.

o CURRENTS OUTSIDE OF OPTICAL
  VOLUME ASSUMED TO HAVE
  R(t) = R(Gas)

o WORSENS MISMATCH OF IMPEDANCE

$R_F(t)$

DRIVER

1

2 x 50 DISCHARGE

3 x 50 DISCHARGE

EXP

i_F/i_D (%)

ENERGY (mJ)

400

300

200

100

0

10   20   30   40   50
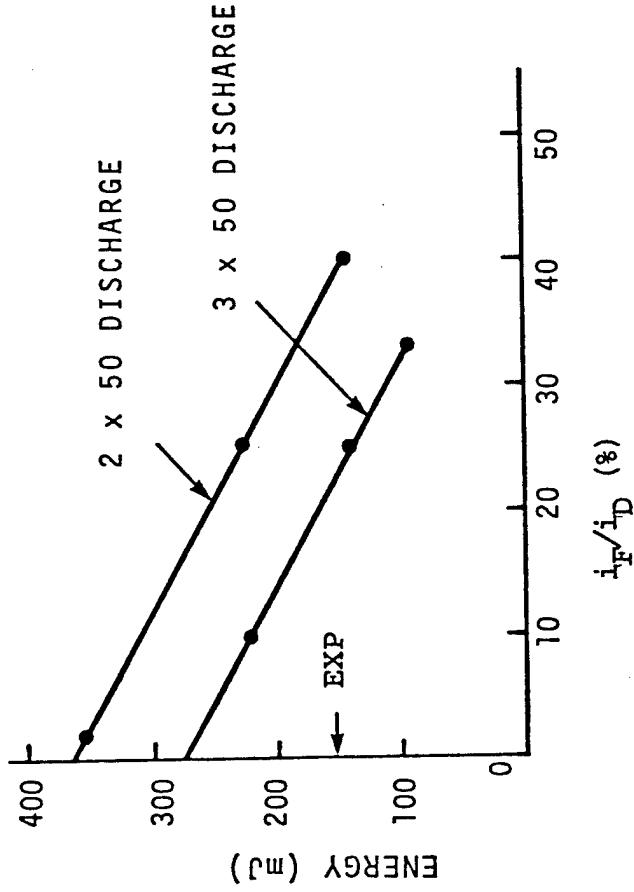
81 048 01

Figure 3-6. Performance degradation due to fringe currents.

time to laser threshold. Use of the direct mechanism leads to a prediction of laser turn on in better agreement with laser power temporal measurements. The code predicts somewhat larger intensity modulations than are actually observed. Figure 3-7 shows a comparison of the laser model predictions for the two extreme cases of only direct pumping and only N_2 transfer pumping. The comparison to experiment is given in Figure 3-8. Each model predicts the laser pulse energy reasonably well for the condition modeled. In Table 3-2 we compare code calculations with measured experimental values for the two electrode spacings utilized and several typical gas mixtures. For the case of pure Ne and $HgBr_2$ at higher densities, the model overpredicts performance. This may be due in part to experimental uncertainties in the $HgBr_2$ density.

One significant difference of the Phase II laser from the present laboratory demonstration is the need for bandwidth control. This is manifested in our design by the use of injection locking the 2 J oscillator. Model calculations show that on the 50 cm device such injection locking is capable of producing improved lasing performance, as shown by the work at NOSC. The estimated effect for efficient pumping is shown in Figure 3-9. An injected flux of 25 kW/cm^2 will clamp the gain sooner and result in about a 15 percent energy density and efficiency increase. Thus for the 100 ns pump pulse of our currently used pulser, an increase in energy density from 0.7 J/L at typically 1.3 percent efficiency to 0.8 J/L at close to 1.5 percent efficiency relative to the rollup capacitor should be readily achievable.

Another strategy for increasing single pulse energy is to increase the pump pulse duration. We have modeled a circuit similar to our current 1 m device which incorporates a larger capacitance driver. The code predicts that 2 J outputs are readily achievable for a lean N_2 mixture.

On the basis of the comparisons between the model predictions and the experimental data it is evident that the model is adequate to describe the qualitative laser characteristics. The model clearly needs better input for a variety of fundamental processes e.g., direct electron excitation versus indirect transfer from N_2 (A). However, since the

DIRECT PUMPING

N_2 TRANSFER ONLY

81 04939   100 nsec/Division
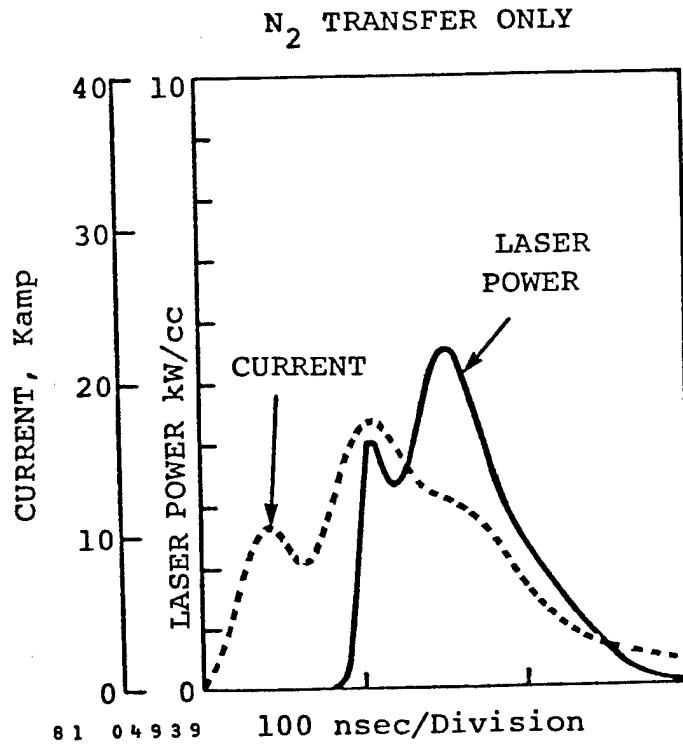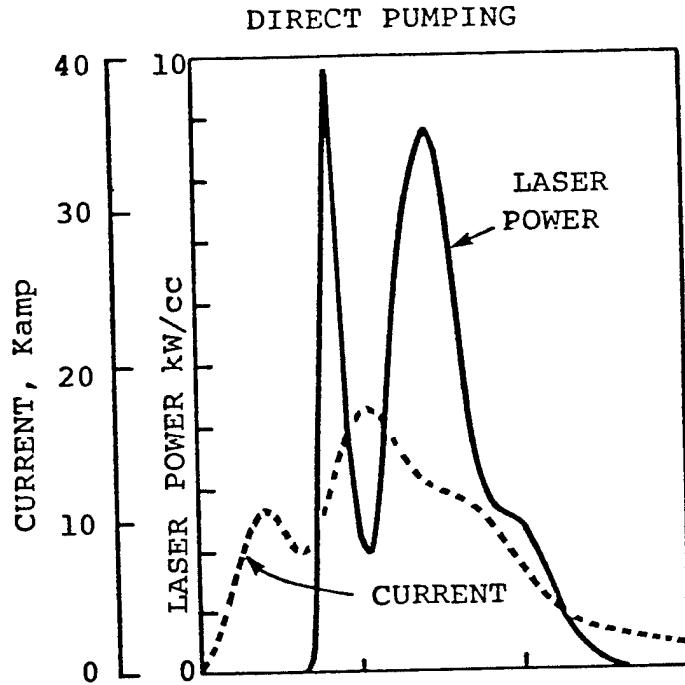
Figure 3-7.   Effect of Direct Excitation of $HgBr_2$ to HgBr(B) for a 2.5% N_2 and 0.25% $HgBr_2$ Mixture in Neon.
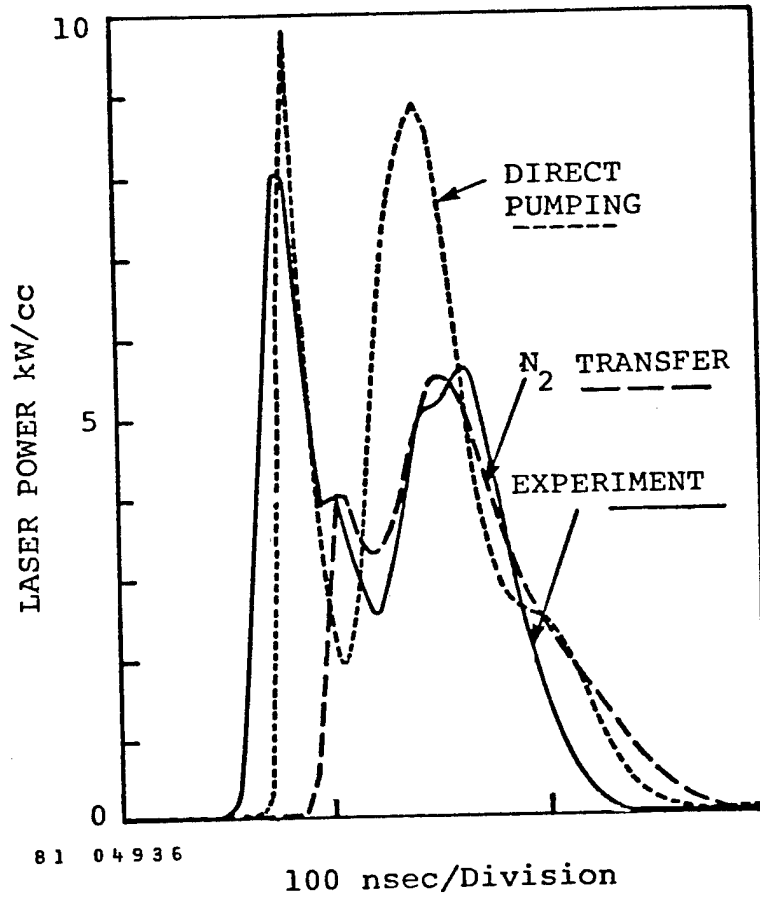
Figure 3-8.   Comparison of experimental power output with theoretical models for 2.5% N_2 and 0.25% $HgBr_2$ mixture in Neon.

Table 3-2

COMPARISON OF EXPERIMENT WITH THEORY

Cavity Size (L=100 cm)	%N$_2$	P$_{HgBr_2}$ (Torr)	V$_o$ (kV)	OUTPUT COUPLING (%)	OUTPUT ENERGY (J) (Theory)	(Experiment)
3.5 x 3	2.5	6*	38	70	0.73	0.65
3.5 x 3	2.5	6*	50	70	1.1	0.95
3.5 x 3	2.5	6*	55	70	1.2	1.1
5 x 4.5	2.5	6*	55	70	1.17	1.1
5 x 4.5	0	6*	55	70	1.7	1.3
5 x 4.5	0	6*	60	70	1.8	1.4
5 x 4.5	0	10**	55	92	2.1	1.6
5 x 4.5	0	10**	60	92	2.8	1.8

*Based on reservoir temperature.

**Based on coldest measured temperature in laser head – possibly in error.
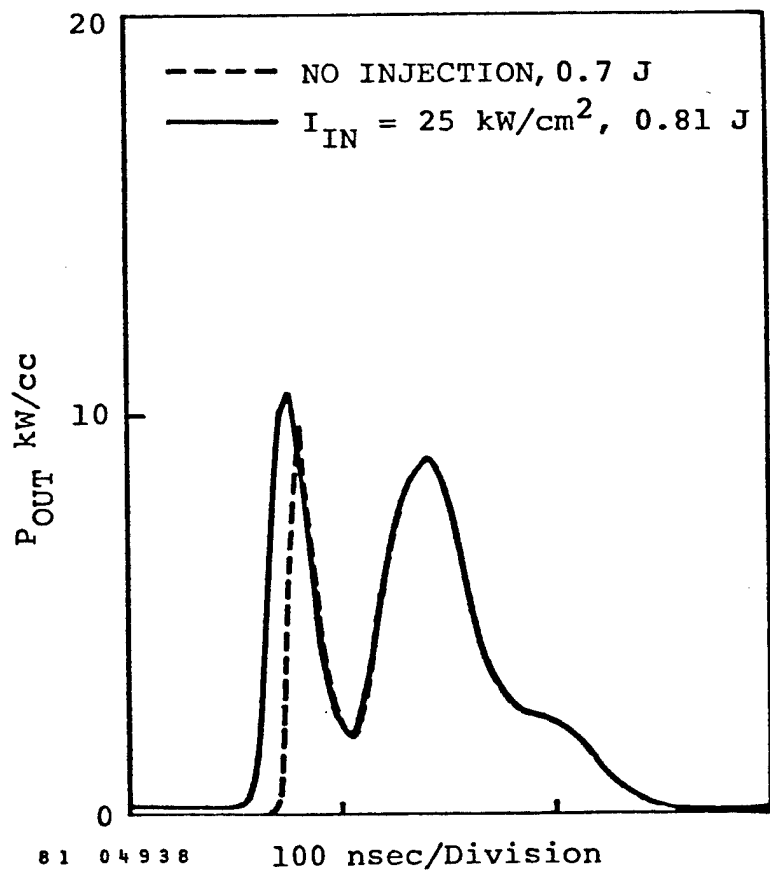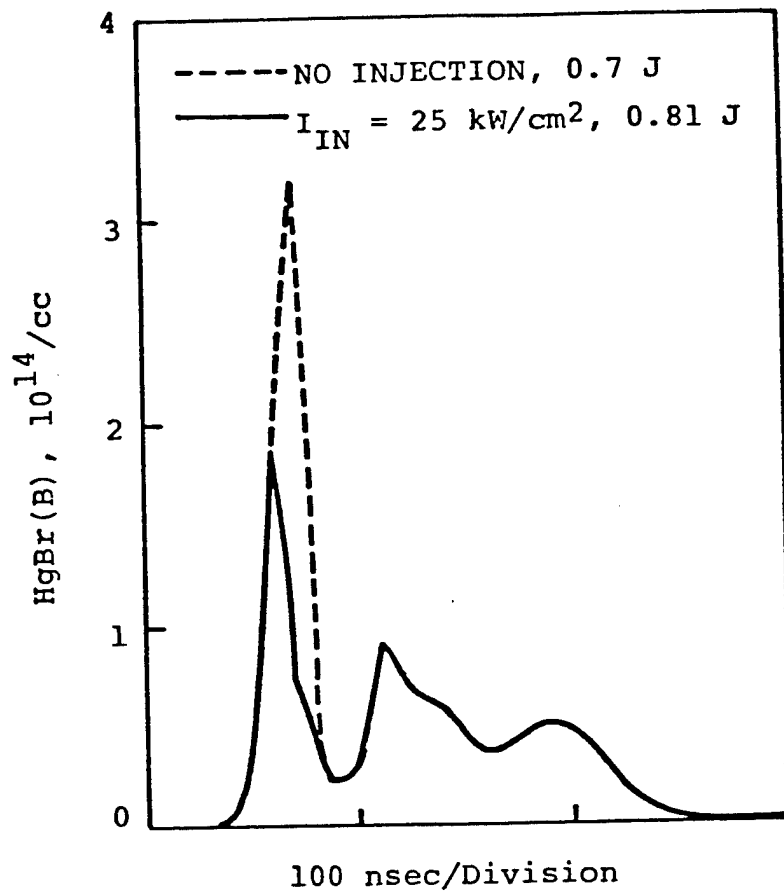
Figure 3-9. Effect of injection on a low pump rate laser for a 2.5% N_2 and 0.25% $HgBr_2$ mixture in Neon.

extrapolation from our current 1.75 J performance to 2 J is modest, the media modeling is adequate to support the system design. The comparison with experimental data will be enhanced in the future by careful measurements of the electrical circuit parameters and temporal characteristics of the switch.

3.2 Spectral Synthesis

We have demonstrated efficient narrow band (0.007 nm) amplification of an Ar ion laser over a limited aperture in our 50 cm device. This is expected from our spectroscopic analysis, which was developed to try to explain regularities in the 504 nm HgBr band.

The theoretical basis for the HgBr spectral analysis has been given by Hertzberg and others.[4] Briefly, the details of the electronic spectrum are derived from the $^2\Sigma\text{-}\Sigma^2$ nature of the transition. The doublet splitting of the P and R rotational branches has been neglected in our model. For simplicity, we assume Boltzmann rotational and vibrational distributions of the HgBr molecues with $T_V = T_R = 450$ K, the typical operating temperature of the laser. Rotational line positions and emission intensities were calculated by standard methods using published spectroscopic constants. Vibrational band intensities were calculated using published Franck-Condon factors.[5] Spectral lines were assumed to have a Lorentzian profile with a linewidth estimated to be 0.15 cm^{-1} FWHM for the conditions of the low pressure 50 cm laser. A synthetic fluorescence spectrum was produced by overlapping the emission from all isotopes of HgBr weighted by their relative abundance and all rotational and vibrational states emitting in that region.

The results of the fluorescence spectrum synthesis near 504 nm for all isotopic HgBr species is shown in Figure 3-10 for $T_V = T_R = 450$ K. The laser emission in the spectral region around 504 nm was analyzed because it exhibits a more open, less overlapped structure, and was potentially easier to analyze. The spectrum consists of contributions from 29 vibrational bands for each of the 12 possible isotopic species weighted by the appropriate natural abundance. Consequently, each separate emission
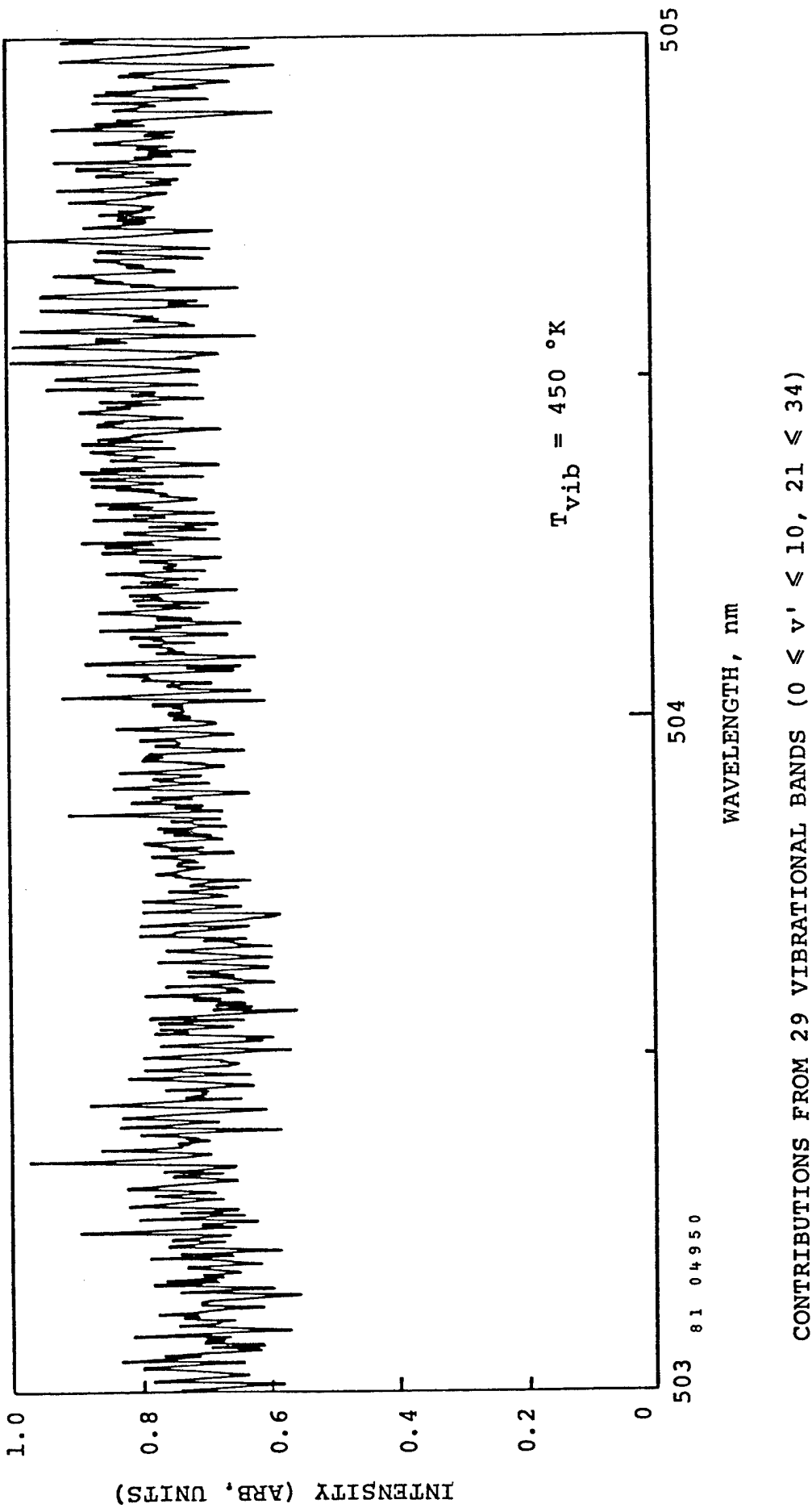
Figure 3-10. Theoretical HgBr Fluorescence Spectrum: All Isotopic Species.

"feature" in the spectrum, far from representing a single vibrational-rotational transition, in fact, samples populations of many different isotopic species distributed over a wide range of vibrational levels.

The model prediction shows two significant features from a narrow band extraction viewpoint. First, the intensity structure observed in lasing is not at all related to any simple rotation, vibration, or isotope effect. Second, any given spectral region is strongly overlapped by contributions from a large number of vibrational states. Thus, the spectrum is not entirely homogeneous but is so fully overlapped as to be rendered a quasi continuum. Finally, the synthetic spectrum for a single isotopic species looks very similar to that for a superposition of isotopes. That is, there are no windows in the spectrum of an $^xHg^yBr$ isotope relative to any other isotope or the sum of the isotopes. Thus, narrow band extraction should not leave energy behind in certain isotopes for a given wavelength. Higher pressures as used in our 1 m device and elevated vibrational temperatures also tend to blend the bands together.

REFERENCES

1. J.L. Levatter and S.C. Lin, J. Appl. Phys. 51, 210 (1980).

2. E.J. Schimitsckek and J.E. Celto, Appl. Phys. Lett. 36: 179 (1980).

3. W.L. Nighan, Appl. Phys. Lett. 36: 173 (1980).

4. G. Herzberg, Molecular Spectra and Molecular Structure, Volume I, Diatonic Molecules, Van Nostrand, New Jersey (1950).

5. N.H. Cheung and T.A. Cool, J. Quant. Spectrosc. Radiat. Transfer 21: 397 (1979).

Section IV

DESIGN CONSIDERATIONS FOR 200 WATT CLOSED LOOP LASER

One of the goals of our program was to develop a design of a 200 watt laser based upon our Phase I results. The design specifications are 2 J per pulse at 100 Hz pulse repetition rate with a wall plug efficiency of 1 percent and a lifetime greater than 10^8 shots. The major subsystems include the laser head, the gas recirculation loop, the pulse power modulator, the x-ray preionizer, and the optical system. The laser head includes the discharge electrodes and high voltage feedthroughs, both of which have to be compatible with flowing gas and with the low inductance and high voltage requirements of the low impedance $Ne/HgBr_2$ discharges. The flow loop includes the fan or blower to clear the gas between discharge pulses, the flow ducting and dampers to guide the flow and attenuate acoustic disturbances, and the heat exchanger to reject waste heat. The construction of this system must be compatible with high pressure (~5 atm) operation and with the hot, corrosive gas mixture. The x-ray preionizer includes the x-ray generator and the window to maximize transmission of the x-rays into the discharge volume. The pulse power modulator includes the rep ratable switch and the discharge pulse forming network. This system must be designed for the conflicting requirements of fast, low inductance switching and long lifetime at moderately high voltages. The optical system includes the cavity mirrors and the injection source required for narrowband operation. The issues for each subsystem and how the design addresses these issues are discussed in the following sections.

4.1   200 W Laser Head

Our Phase I effort included the preliminary design of a 200 watt laser. The extrapolation from our present 1 m device performance to the laser head for the 200 watt machine is modest. For scaling purposes we take as a base case the 1.4 J per pulse which corresponds to the highest efficiency in a 2 liter volume in $Ne/HgBr_2$ or Ne/2.5 percent $N_2/HgBr$ lasing mixtures. Clearly to drive a 2 J laser we need to increase the pulser

energy or the laser head efficiency. While we expect the laser head efficiency will improve with further optimization, we base a design of the 200 W device on a small increment in efficiency gain. This will occur from the use of injection locking, which allows the gain to be clamped earlier in the pumping pulse. Model calculations imply an increase in performance of about 10 percent by injection locking. We require 100 J delivered to the laser head by the pulser.

To increase the lasing energy the lasing volume may be increased or the energy density may be increased. We based our design on the proposal to increase the energy density slightly by utilizing a somewhat longer pump pulse duration, nominally 130 ns rather than our currently used nominal 100 ns. With a 2 liter volume, injection locking, and a 130 ns pump pulse, a 2 J per pulse single shot energy seems quite reasonable. The 2 liter volume can be obtained by using the same electrode profile and dimensions as our Phase I laser so that the lasing aperture is 4.5 x 4.5 cm^2 with an active length of 1 m.

As a backup position to the above scaling scenario, we have two simple alternates: length scaling at the same aperture as currently used, or aperture scaling at 1 m gain length without energy density scaling. These are each conservative approaches, but do have drawbacks. Length scaling beyond 1 m becomes somewhat cumbersome from a mechanical point of view. A longer gain length also requires greater work at parasitic suppression since the net $g_o L$ would be of order 8 to 10 for a length scaled device. A larger aperture and 1 m gain length is a second backup position. This impacts the pulse power because of greater voltage requirements for breakdown if discharge height is increased. In addition, the use of a larger discharge volume, will cause a significant increase in gas flow rate and flow power.

For the sake of further discussion, we will assume that a 4.5 x 4.5cm^2 laser volume and 1 m gain length will pass the relevant design verification tests and will be used as the nominal laser dimensions.

4.2 Flow Loop

Gas flow is required to flush the discharged gas from the laser volume between pulses. Because of the nature of the gases and the long run mission, a closed cycle flow system must be provided. This flow loop must cool the discharge heated gas to a uniform temperature and remove discharge generated disturbances to provide a uniform laser medium for the succeeding pulses. The medium must be capable of producing an output beam spreading angle equal to or less than ten times the diffraction limit during long term operation. Gas recirculation must be provided with a minimum power investment to allow high overall device efficiency.

If a laser operating at 4.75 atmospheres produces 1 J output per liter with a laser head efficiency of 2 percent the discharge will deposit 10.3 J per liter atmosphere into the gas. The fraction of this energy appearing as heat will be

$$\frac{[(\gamma-1)\ E/RT + 1]^{1/\gamma} - 1}{(\gamma-1)\ E/RT}$$

where E/RT is the dimensionless energy added and is the ratio of specific heats, 1.62 for a typical $HgBr_2$ mixture. The discharge will deposit 6.3 J per liter atmosphere in the gas as heat, producing a local gas temperature rise of 18 $^\circ$K. At a PRF of 100 Hz, this thermal energy input amounts to 630 W per liter atmosphere which must be removed by a heat exchanger in the flow loop.

The rest of the 10.3 J per liter atmosphere is carried out of the discharge region in the form of acoustic waves. The leading compression wave which will be the strongest wave will have a 3.17 percent pressure rise.

In order to provide a beam spread less than or equal to ten times the diffraction limit, both the laser medium and optics must be of high quality. Under the assumption that one-half the degradation will be introduced by the optics, an ordered density uniformity of 0.13 percent or

less is required of the flowing laser medium. These density disturbances can arise either from temperature variations in the cavity or from pressure disturbances remaining from previous pulses. For design purposes it is assumed that one-half the allowable density perturbation budget is assigned to pressure waves. Therefore these pressure waves must be attenuated to levels of 0.11 percent. Methods of achieving the required 30 db attenuation are discussed in Section 4.2.3.

4.2.1 Flow System Configuration

The flow loop consists of a heat exchanger to remove the discharge deposited heat, provisions to cause the required attenuation of pressure disturbances, a circulator to replace the momentum lost in traversing the flow loop together with bends and ducting to form a continuous 360 degree turning of the flow. The desired PRF, the cavity flow length and the design clearance factor determine the required laser cavity velocity. Since the pressure drop in a duct varies as the square of velocity, it is necessary to decelerate the flow downstream of the cavity through a diffuser into a larger area duct and, after traversing the flow loop, then accelerate the flow through a nozzle upstream of the cavity in order to decrease the power required to circulate the flow. These components can be arranged in the form of a small wind tunnel as shown in Figure 4-1.

The laser cavity flow area typically has a very high aspect ratio, that is, the optical length is an order of magnitude larger than the excitation height. The flow loop may be fabricated with a rectangular flow cross section to accomodate this geometry. Transition to circular cross section to match many circulators requires large volume transition sections to avoid separated flow. The diffuser then will be a two dimensional design that can be shortened with the use of splitter plates. Vanes are provided in the duct bends to allow small volume turns with reduced pressure drop and secondary flows.

The circulator fan may be of the axial or centrifugal type. An axial fan requires long transition sections to its round cross section and is quite sensitive to flow nonuniformities requiring substantial upstream
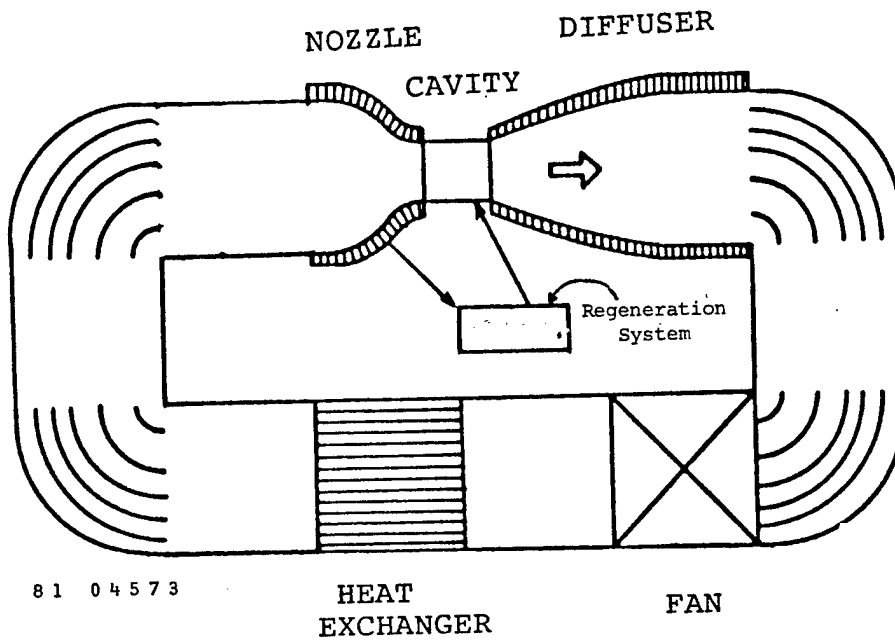
Figure 4-1. Schematic of external flow loop for Closed Cycle Pulsed Laser.

and downstream isolation to assure reliable operation. It can be very efficient however and produce quite uniform flow in the vane-axial configuration.

Centrifugal fans are much more adaptable in operation, offering a wider range of performance. They are of simpler design and can be integrated in the flow loop to provide one of the required 90 degree flow turns. Although these fans produce a relatively nonuniform exhaust flow, simple diffusers can be incorporated to introduce the flow to the heat exchanger, which by virtue of its viscous heat transfer also removes flow nonuniformities. Both these types of fans can be designed to require only one rotating seal to bring power into the duct.

The heat exchanger is placed downstream of the fan to smooth the fan exhaust and provide the temperature uniformity required in the laser cavity. The heat exchanger is most conveniently located in the uncrowded return leg of the flow loop. In cases of extremely stringent cavity uniformity requirements, a heat exchanger or thermalizer can be placed immediately upstream of the laser cavity. Two types of heat exchanger are applicable to the flow loop: the tube and shell type and the cross flow tube type. Although the cross flow tube type heat exchanger is theoretically better suited to application in a closed loop laser, the practical aspects of electroplating may increase the relative suitability of the tube and shell design.

After traversing the vaned flow bends, the laser flow is accelerated in the nozzle from the low loop velocity to the required cavity velocity. The design of this nozzle together with that of the diffuser is critical to the reliable operation of the flow loop under repetitively pulsed conditions. It is necessary to avoid the presence of separated flow regions in these components at any time during the cycle. Because of the low level of energy deposition in the discharge, the upstream running wave will not reverse the flow in this laser. However, this pressure wave will slow the flow to approximately 60 percent of its undisturbed velocity for a short time until the upstream running expansion overtakes and reaccelerates the flow. During this time the boundary layer velocity profile may become

unstable in the nozzle. The nozzle must be designed to operate without separation during this process.

The diffuser should be a conservative wedge type with an 8 degree included angle. The diffuser also experiences unsteady flow and must be designed conservatively to avoid flow separations. Although separations in the diffuser are not as serious as separations in the nozzle, the subsonic nature of the flow allows downstream disturbances to affect cavity uniformity by means of upstream running pressure disturbances. The diffuser can be shortened by the use of a splitter plate parallel to the optical axis that will split the flow in two and therefore reduce the required diffusion length by half. If necessary, acoustically absorbing material can be located on the sidewalls of the diffuser and nozzle sections.

4.2.2 Flow Loop Materials

Flow loop materials must be chosen to satisfy the requirements of structural integrity and chemical compatibility. Structurally the loop materials must be capable of design for a pressure vessel operating at about 450 $^\circ$K. Chemically the loop materials must be compatible with hot mixtures of $HgBr_2$ and its derivatives. Several materials are able to meet the structural requirements but few can fulfill the chemical compatibility requirements. The chemical compatability considerations, based on thermochemical calculations and practical experience, indicate that the two precious metals, gold and platinum, should be able to meet the chemical compatibility requirements. Although certain elements of the flow loop might be fabricated of pure precious metal, economic considerations dictate that the flow loop structure be fabricated from a structural base metal with internal surfaces plated with precious metal. Conceivably, a stainless steel system could be made that would not degrade the gas mix, but this is not a thermochemiclly safe approach.

Thermochemical screening calculations also suggest that the refractory metals, molybdenum and tungsten, should be fairly inert to reaction with mercury dibromide. Very limited experimental data are

available for these materials and are mostly based on HgBr discharge studies at MSNW and elsewhere[1,2] in both lasing and nonlasing media. The experimental experience to date suggests that preference should be given to the noble metals. There is insufficient experience with the refractory metals, although some experiments by Schimitschek et al.,[2] and Liu[1] indicate that molybdenum may not be a suitable surface material.

Several structural materials would be suitable for loop construction at the design pressure and temperature. The thermal expansion coefficient must be matched with that of the overcoat to assure adhesion during thermal cycles. Type 300 stainless steels are well suited to gold electroplating and type 400 stainless steels are well suited to platinum electroplating. Mild steel lies between the two, however experience has shown that stainless steel is more able to withstand chemical attack that might occur through microcracks or poorly plated areas. Al_2O_3, which is chemically compatible, may also be coated on mild steel, however reliability under thermal cycling must be demonstrated.

4.2.3 Medium Homogeneity

The flowing laser medium must be capable of producing an output beam spread, containing 80 percent of the beam energy, less than or equal to ten times the diffraction angle from the optical aperture. For a beam of uniform intensity, this corresponds to a half angle of 10 λ/d. A maximum phase front variation of 5 wavelengths will produce this large a spreading angle if the density disturbance is in the form of a triangular function across the aperture. This form of phase variation is difficult to compensate in the optical train. Since both the optical train and the flowing medium contribute to the overall phase front degradation, a maximum of 2.5 fringe disturbance was allowed in the laser medium.

The required density uniformity for ordered disturbances can then be written as

$$\frac{\Delta\rho}{\rho} = \frac{3\lambda}{L\beta p/p_s}$$

where λ is the output wavelength, L is the optical pathlength, β is the Gladstone Dale constant for the mixture and p/p_s is the cavity amagat level. The Gladstone Dale constant for $HgBr_2$ was calculated from the dielectric constant measured by H. Braune and R. Linke[3] to be 2.44 x 10^{-3}. The Gladstone Dale constant for the mixture, a function of the molar ratios, is 8.90 x 10^{-5} because of the large amount of Neon present. Thus, a maximum ordered density nonuniformity of 0.13 percent or less is required in the case of three passes through a 1.5 m long cavity.

There are several types of density disturbances that can contribute to the overall cavity density nonuniformity. All of them fall into two categories, either ordered or small scale disturbances. Ordered density disturbances are most detrimental when the maximum gradient is normal to the optical direction. Their effect on phase front uniformity is given by the interferometer equation used above. The phase distortion through ramdom small scale disturbances can be modelled as a random walk process. The overall phase front distortion given by the interferometer equation is then multiplied by the square root of the ratio of disturbance scale size to overall path length.

For this reason, random disturbances such as free stream turbulence and boundary layer turbulence will not adversely affect optical quality. The density fluctuations associated with free stream turbulence scale as:

$$\frac{\Delta \rho}{\rho} \sim M^2 (\Delta u/u)^2$$

since the cavity Mach number M is very low for a 100 Hz device of this size (M = 0.032), even a flow loop without special turbulence management ($\Delta u/u$ = 0.1) will allow very good optical quality because the turbulence scale size will be on the order of 1 percent of the cavity optical width.

Since pressure fluctuations in the boundary layer scale with the wall shear stress, the associated density fluctuations scale as

$$\frac{\Delta \rho}{\rho} \sim M^2 (Re)^{-1/5}$$

Under the assumption of boundary layer growth commencement at the end of the cavity nozzle, the cavity Reynolds number, Re, will be on the order of 10^5. Since these turbulence fluctuations are approximately the size of the boundary layer thickness

$$\frac{\ell}{\chi} \sim (Re)^{-1/5}$$

or only 1 percent of the cavity optical width, their effect on optical quality is also very small.

Another type of small scale density disturbance can be introduced by temperature fluctuations in the isobaric cavity flow. Such fluctuations could appear in wakes from upstream flow loop components or from temperature variations downstream of the heat exchanger and they will have a scale length on the order of 1 percent of the cavity optical length. Since approximately 60 percent of the discharge energy appears as heat, it is reasonable to allocate half of the medium density nonuniformity budget to such temperature disturbances. This indicates that random temperature variations with a scale length as large as 1.5 cm should be less than 3 $^\circ$K to assure the required medium quality. It should be straightforward to control wall temperatures to within this specification. Consultation with heat exchanger designers has indicated that typical temperature variations across outlet flows are about one half this value. Turbulent mixing in the intervening ductwork should further reduce this variation.

Ordered density disturbances are associated with the pressure pulses produced by the discharge. The size of the leading compression wave, P_2/P_1 can be calculated from the implicit expression

$$\frac{T_4}{T_1} = \frac{P_2}{P_1} \left[1 - \frac{(\gamma-1)(T_1/T_4)^{1/2}(P_2/P_1-1)}{((2\gamma)(2+(\gamma+1)(P_2/P_1-1)))^{1/2}} \right]^{-\frac{2\gamma}{\gamma-1}}$$

where γ is the mixture ratio of specific heats and

$$\frac{T_4}{T_1} = 1 + (\gamma-1) E/RT$$

and E/RT is the dimensionless Joules per liter-atmsophere deposited into the gas.

For the HgBr laser producing 1 joule per liter at 2 percent laser head efficiency and 4.75 atmospheres pressure, the pressure rise in the leading compression wave is only 3.2 percent. This small pressure wave must be attenuated and dispersed before it returns to the optical cavity. Allowing one half the medium quality budget to such pressure waves, the attenuation must be to a value of 0.16 percent pressure rise or a factor of 26 decibels.

The optical quality responds to the density variation across the cavity aperture, so that a flow disturbances with wavelengths significantly longer than the aperture width could be allowed to have greater amplitudes. Characteristic calculations show that a long time is required for the expansion fans to overtake the initial pressure waves and reduce the pressure rise to acceptable levels. The pressure waves reflect from flow corners, fan blades, the heat exchanger and the area variations to produce a complex field of pressure disturbances in the flow loop. During the reflection process, the shorter wavelength disturbances tend to cancel each other out, leaving the longer wavelength disturbances which are primarily damped in the viscous flow in the heat exchanger and flow loop corners. The density uniformity in the cavity can recover very rapidly as a result of these processes even without the provision of additional acoustic damping on the channel walls.

4.2.4 Flow Loop Efficiency

The overall laser efficiency may be defined as

$$e_L = \frac{P_o}{P_e + P_f} = (1/e_e + 1/e_f)^{-1}$$

where P_o is the laser output power, P_e is the power provided to the electrical system and P_f is the power provided to the flow circulation unit. The electrical and flow system efficiencies may be defined as shown. In particular, the flow loop efficiency is defined as

$$e_f = P_o/P_f$$

Which may be written in the form

$$e_f = \frac{2E_o n}{pcf\ D\gamma M^2}$$

where E_o is the output energy volumetric density, p is the cavity pressure, C is the ratio of cavity flow width to discharge width in the optical direction, D is flow loop pressure drop measured in cavity dynamic heads, M is the cavity Mach number, γ is the ratio of specific heats, n is the compressor efficiency, and f is the cavity clearance factor which determines the cavity flow velocity:

$$u = fLv$$

in terms of the cavity flow length, L, and the PRF, v. Substitution for the cavity Mach number and the use of E_o in units of joules per liter and p in atmospheres results in the expression:

$$e_f = \frac{1.66 \times 10^6 T\ E_o n}{cp\ W\ D\ L^2\ v^2\ f^3}$$

The parameters are:

T, cavity temperature, ^oK

E_o, output energy density, J/l

n, compressor efficiency

c, ratio of flow length to discharge length in optical direction

p, cavity pressure, atmsopheres

w, mixture molecular weight, gm/mole

D, flow loop pressure drop, multiples of cavity dynamic pressure

L, cavity length in flow direction, cm

v, pulse repetition frequency, Hz

f, number of cavity volumes circulated per discharge

For the HgBr laser mixture at 450 °K operating at 100 Hz and producing 2 J from 2.5 liters discharge volume, the flow efficiency can be as high as 0.1 when the fan efficiency is taken as 50 percent, the flow cavity is 20 percent longer than the discharge, the pressure is 4.76 atm, the cavity flow width is 3.5 cm, and the cold flow clearance factor is 4.8 at 100 Hz. This cold flow clearance factor corresponds to 2.4 at the maximum prf of 200 Hz, required for the maximum pulse modulation excursion. A clearing factor of 2.4 has been demonstrated on the Mistral device. The flow loop pressure drop has been taken as 1.6 times the cavity dynamic pressure. The effect of flow loop design on overall system efficiency is shown in Figure 4.2. This figure is drawn for the conditions described above in which the flow loop cross-sectional area is 6 times that of the laser cavity. A flow loop efficiency calculation was also made for a smaller volume flow loop with an expansion ratio of 4. The figure shows the increasing benefit of more efficient flow loop design when the electrical efficiency is increased.

Figure 4.3 shows the relationship between the flow loop efficiency and electrical efficiency for an overall system efficiency of 1 percent. In the region of operation, a small increase in electrical efficiency is equivalent to a large increase in flow loop efficiency. For the nominal design with expansion ratio equal to 6, an electrical efficiency of 1.11 percent is required.

The sensitivity of flow loop efficiency and overall efficiency to flow loop design changes can be seen from these figures. The flow loop efficiency is seen to be quite sensitive to the cavity clearance factor, the cavity length in the flow direction and the pulse repetition frequency. The cavity clearance factor is determined by the desired pulse position modulation. The sensitivity to this parameter is shown on Figure 4.5. For a particular flow loop design and the nominal flow loop parameters given previously, without any pulse position modulation, the flow loop efficiency would be 85 percent. When the pulse position modulation requirement is 5 msec, the flow speed is doubled throughout the flow loop and the flow loop efficiency is reduced to 10 percent. For 7 msec pulse
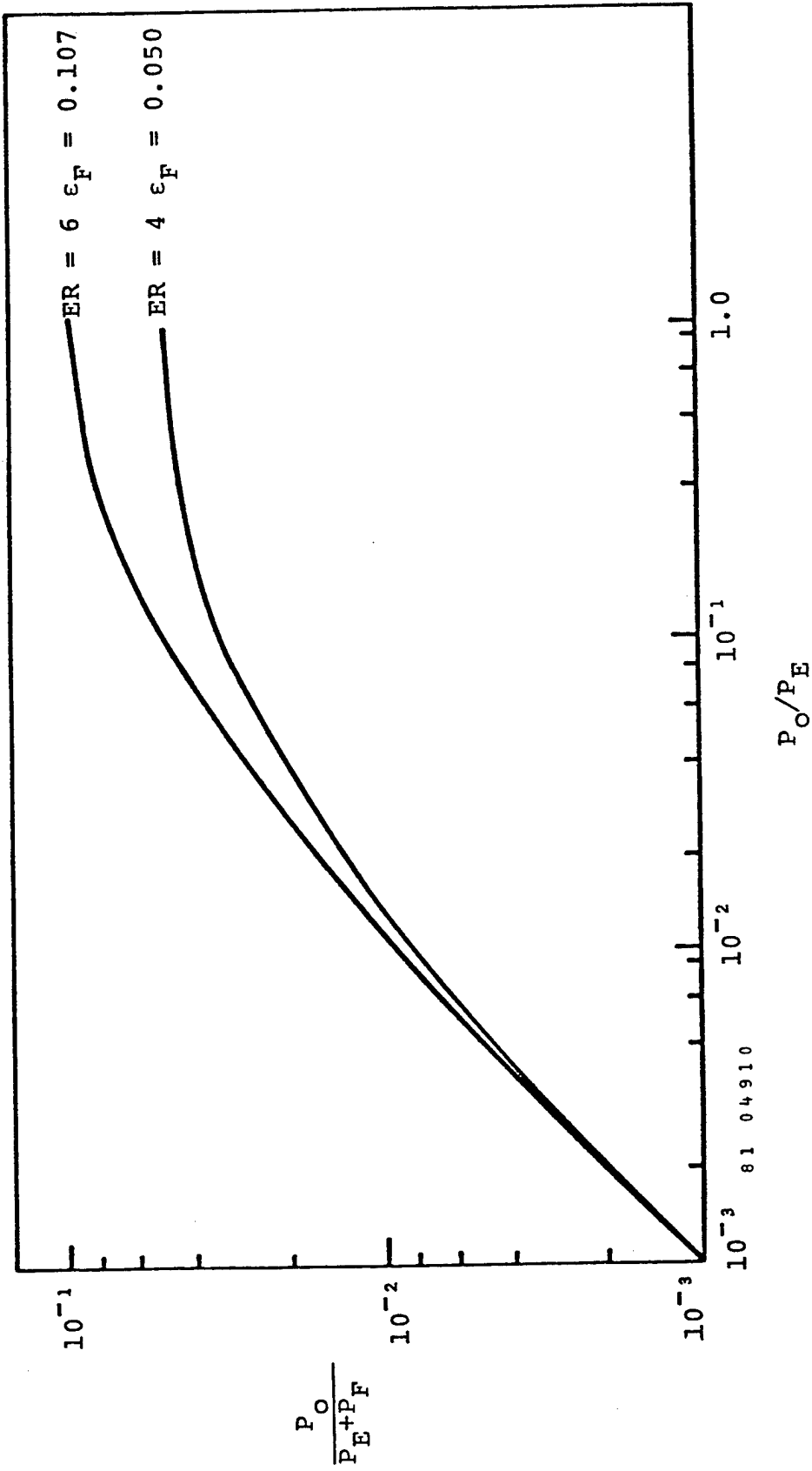
Figure 4-2. Total laser system efficiency.
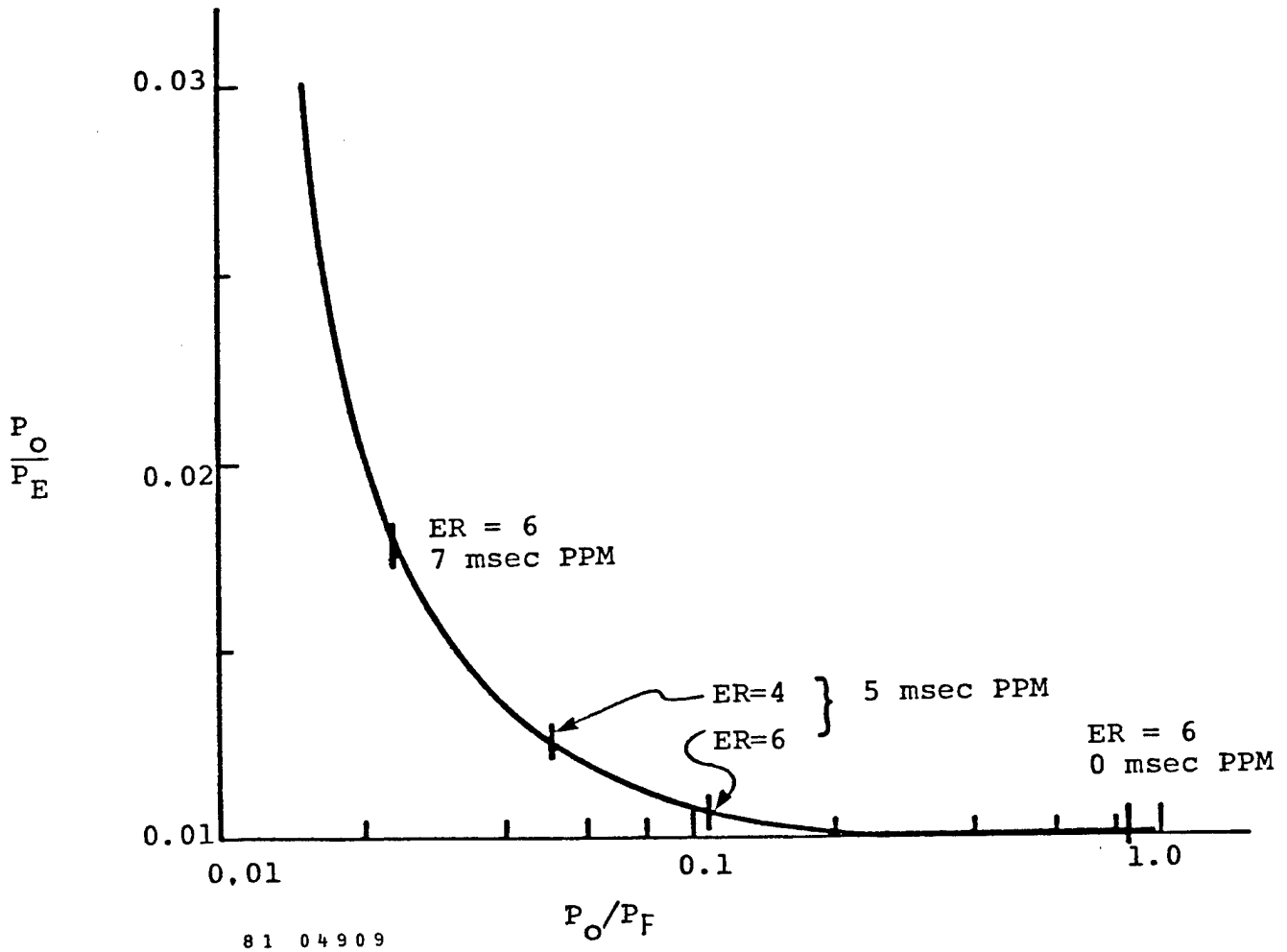
Figure 4-3. Design effects on flow loop and electrical efficiencies for overall 1% efficient system.

position modulation the flow efficiency drops to 2.3 percent. Clearly, for larger values of pulse position modulation or pulse repetition frequency, the flow loop must be redesigned to accommodate the higher cavity flow, utilizing a larger direct and heat exchanger expansion ratio.

4.3 Preionization Technique/Choice of X-ray Approach

Three different preionization techniques can be used to obtain stable self-sustained discharges in the rare gas halide lasers as well as in the HgBr laser. These are uv preionization, electron beam preionization, and x-ray preionization.

Both electron beam and x-ray preionization have the advantage of potentially uniform preionization as compared with the uv approach. The x-ray preionization tends to be volumetrically uniform because of the long absorption lengths as well as the random direction of ionization following absorption of a photon. E-beam preionization is also uniform at high voltages, and the deposition is determined by the multiple scattering path of the electrons in the gas. In contrast, the uv absorption cross sections are typically quite large, with the mean free path comparable to or less than the discharge dimensions of several centimeters.

Experiments in both $HgBr_2$ gas mixtures as well as rare gas halogen lasers have shown that the time overlap between the preionization source and the discharge is not critical provided the preionization preceeds the application of the main discharge. This is shown in Figure 4.4 for x-ray preionization of the 30 cm HgBr laser in which the laser performance (energy) is plotted as a function of the delay time between the preionization and the main discharge. Similar results have been obtained in XeF using electron beam preionization.[4]

Since all three techniques have been shown to be applicable to the HgBr laser, the choice of the preionization technique for the 200 watt closed loop design must be based on factors affecting technical risk and overall system efficiencies. The major technical problem concerns the system lifetime and reliability. We have discarded uv preionization
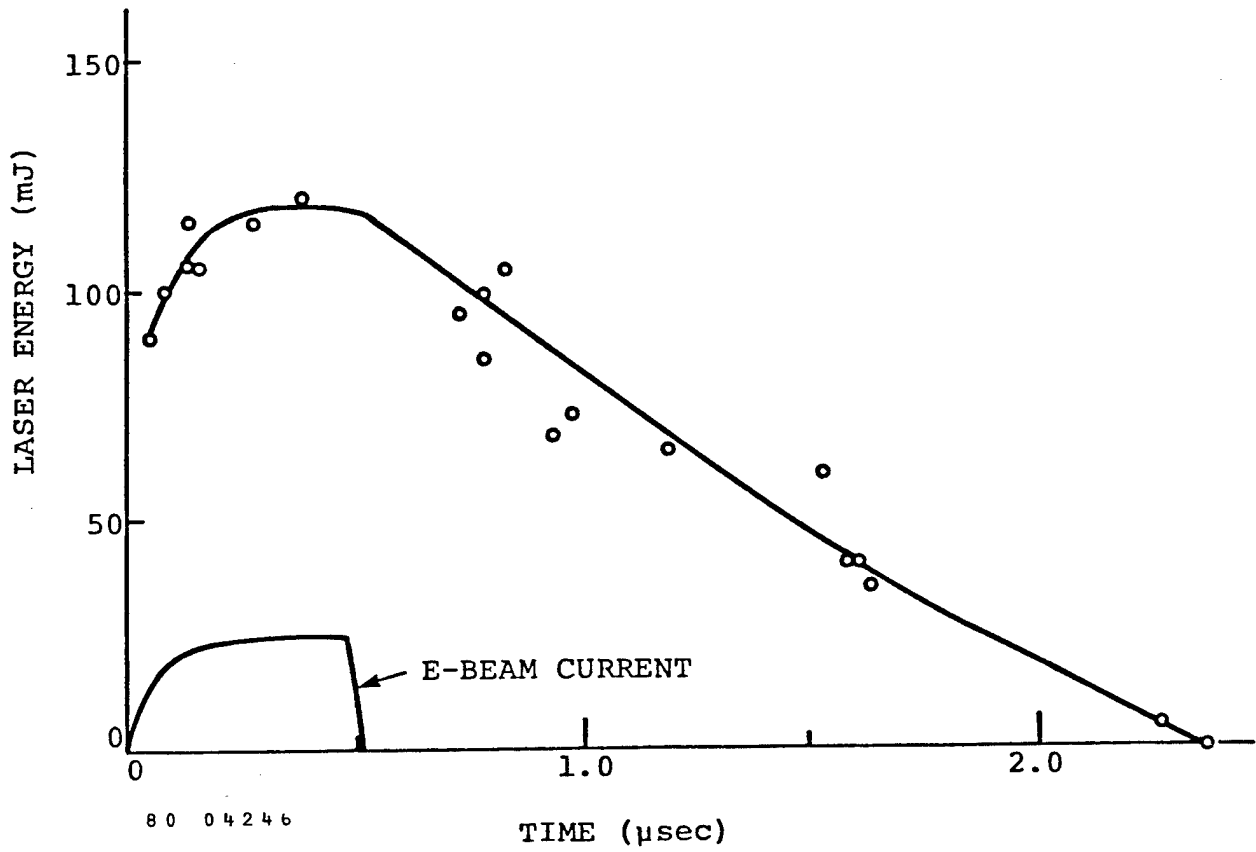
Figure 4-4.   Effect of delay between Preionization and
Main Discharge.

because 1) erosion of the uv spark sources tends to generate impurities and limits the lifetime of the spark source, 2) the very high temperatures associated with the uv source may lead to chemical reactions in the gas, and 3) it is difficult to isolate the discharge from the thermal disturbance created by the uv source.

A major factor in the choice of x-ray preionization over e-beam preionization has to do with the window interface which isolates the high vacuum region of the x-ray or e-beam and the discharge region. In the case of an e-beam, this window must be a thin metallic membrane (in order to provide high transmission for the electrons), and it is susceptible to mechanical failure. With an x-ray preionization source, the window can be much thicker while maintaining high x-ray transmission.

4.3.1 Source Requirements for HgBr Laser

The preionization source strength required for stable self-sustained discharges in $HgBr_2$ gas mixtures is determined by the minimum required electron density and the attachment properties of the gas mixture.[5] This required source strength is independent of the method of preionization. Levatter and Lin[5] have shown that the discharge stability is a sensitive function of rate of rise of voltage on the discharge and the preionization level. For typical attaching gas mixtures, they deduce a minimum preionization level of the order of 10^5 electrons/cm^3.

In an attaching gas mixture the positive and negative ion densities are determined by

$$\frac{dn_e}{dt} = S - \alpha n_e n^+ - k_a n_e X$$

$$\frac{dn^-}{dt} = k_a n_e X - \gamma n - n^+$$

$$n^+ = n_e + n^-$$

where n_e is the electron density, n^- is the negative ion density, n^+ is the positive ion density, S is the source strength, α is the electron-positive ion recombination rate coefficient, γ is the saturated two body ion-ion

recombination rate coefficient, k_a is the attachment rate coefficient, and X is the density of the attaching species.

The attachment rate coefficient in $HgBr_2$ is very small in the absence of a strong applied electric field, as determined by the experiments of Wiegand.[6] Typically,

$$k_a < 10^{-11} \ cm^3/sec$$
$$\alpha \sim 10^{-6} \ cm^3/sec \qquad \text{for } \frac{E}{N} < 10^{-17} \ volt\text{-}cm^2$$
$$\gamma \sim 10^{-6} \ cm^3/sec$$
$$X = (HgBr_2) \sim 10^{17} \ cm^{-3}$$

so that

$$\alpha \ n_e \ n^+ \ll k_a \ n_e \ X$$

and under steady state conditions the required preionization source strength is

$$S = k_a \ n_e \ X \sim 10^{12} \ cm^3/sec$$

A typical x-ray source configuration for the 200 watt design is shown schematically in Figure 4.5. An electron beam generated in a high vacuum chamber is directed toward a high Z target, and the resulting x-rays are transmitted into the discharge region via a low Z vacuum window. The ionization source strength in the gas discharge region is:

$$S = \frac{1}{\varepsilon} \int \mu(\upsilon) \ T(\upsilon) \ F(\upsilon) \ d\upsilon \quad (cm^{-3}/sec)$$

where ε is the energy to create an ion pair, $\mu(\upsilon)$ is the absorption coefficient in the gas, $T(\upsilon)$ is the window transmission, and $F(\upsilon)$ is the x-ray flux at the window. The source strength depends linearly on the absorption coefficient at any one frequency because of the small x-ray absorption coefficient.

For a line source of strength $G(\upsilon)$, the x-ray flux can be expressed[7] as

$$F(\upsilon) = \frac{G(\upsilon)}{2\pi a} = \frac{2.4 \times 10^{-31}}{2\pi a} \ j_{eb} Z(\upsilon_m - \upsilon) \quad (ergs/cm^2/sec/sec^{-1})$$
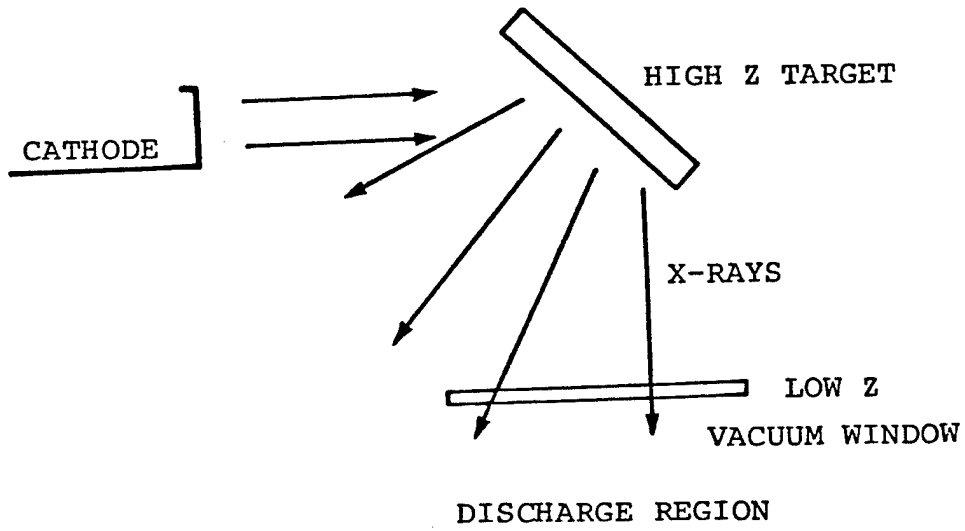
80 04356

Figure 4-5. Sketch of preferred X-ray source
configuration.

where a is the distance from the target to the center of the discharge region and J_{eb} is the e-beam current per unit length. By substitution, one obtains

$$S = 6.6 \times 10^{-22} \frac{j_{eb} Z}{a} \int \mu(\upsilon) \, T(\upsilon) \, (\upsilon_m - \upsilon) \, d\upsilon \qquad (cm^{-3}/sec)$$

It should be noted that the x-ray flux is largest at low energies, and the resultant source strength is optimized by enhancing the low energy region of the spectrum. This is illustrated in Figures 4.6 and 4.7 showing the photoionization absorption coefficient in the gas and the window transmission as a function of x-ray energy.[8] The discontinuities in the photoabsorption curves are due to the K and L edges of $HgBr_2$. The window transmission plot clearly shows the desirability of using low Z materials. Beryllium is a good choice because of its mechanical properties at high temperatures. However, the chemical compatibility of this window material needs to be investigated.

Using this photoabsorption and window transmission data, one can evaluate the integral in the source strength equation to yield

$$S \sim 10^{15} \, J_{eb} \quad (cm^3/sec)$$

where we have assumed a tungsten target (Z = 74) and a mean distance, a = 15 cm. This implies a required e-beam linear current density on the order of 1 ma/cm or greater.

4.4 Discharge Pulse Power: Design Requirements and Risks

An estimate of the laser system power budget suggests that 85 percent of the 20 kW input should be available to the power conditioning system, including the preionizer. The x-ray preionization source required for this laser has a projected maximum power consumption of approximately 1 kW. The remaining 16 kW of electrical power can be utilized for the electrical modulator. Thus, to meet the overall efficiency specification
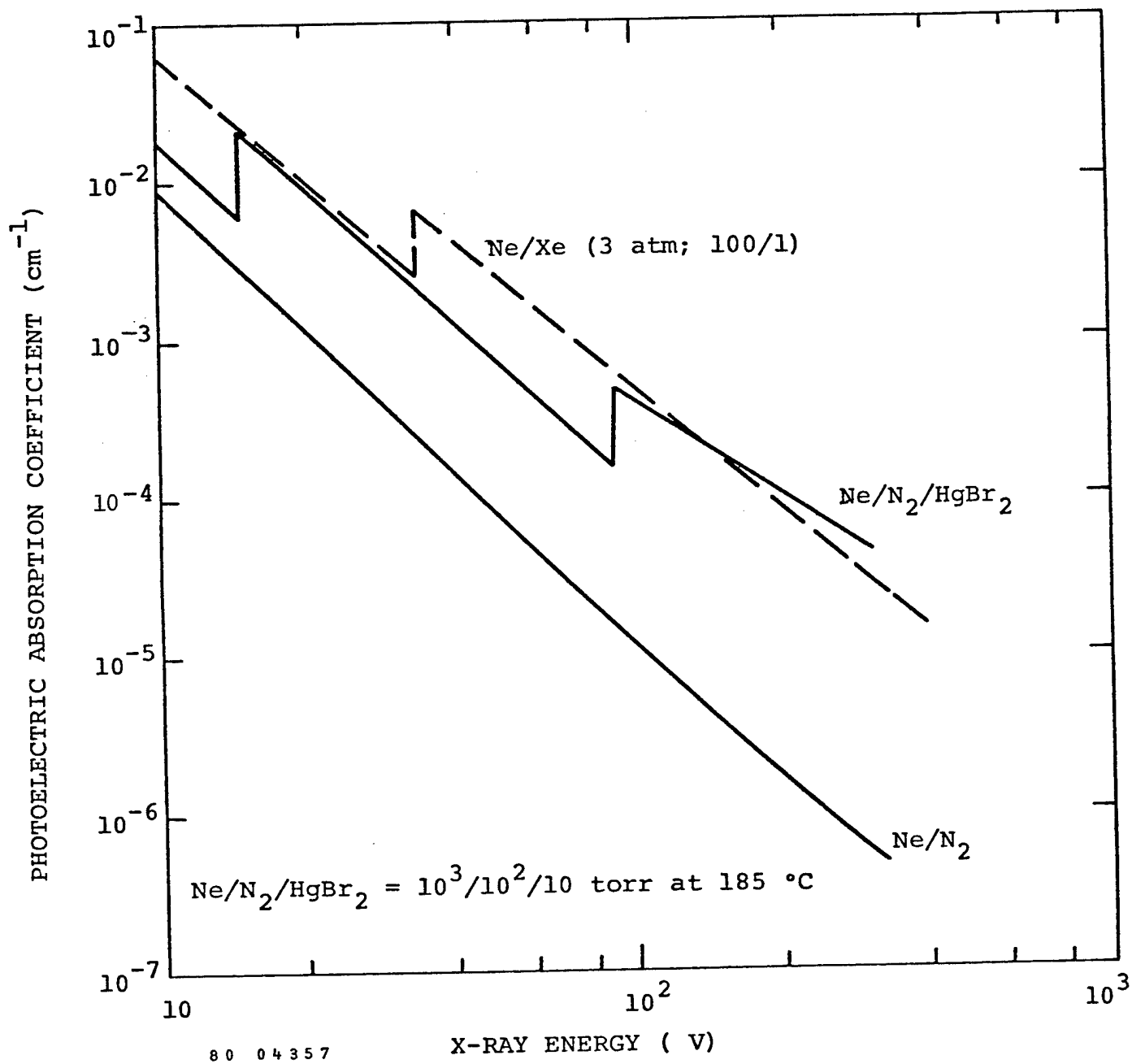
Figure 4-6.   Photoionization Absorption Coefficients
              in Typical Gas Mixtures.
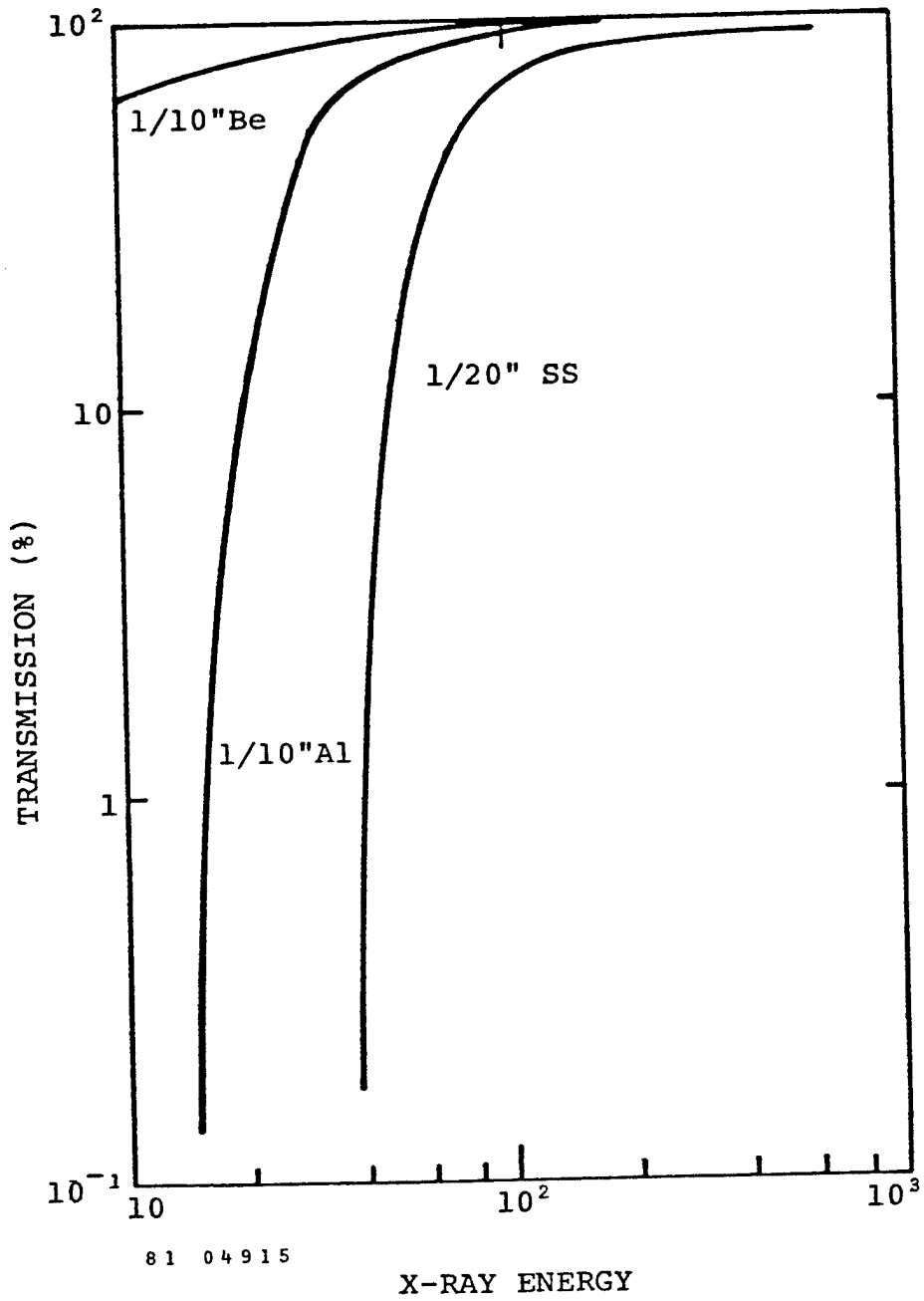
Figure 4-7.   X-ray Transmission through
             various window materials.

of at least 1 percent at 2 J per pulse output with the demonstrated laser head efficiency of 2 percent, it is necessary to achieve 63 percent efficiency for the power conditioning.

Lifetime for the proposed device is also a significant consideration. Power conditioning components need to be selected for a 10^8 shot system life for the next phase of the blue green program. Ultimate extension to 10^{10} shot life will be required for a truly long run device. This lifetime consideration seriously impacts the selection of pulser components.

In Figure 4-8 we show an idealized description of the modulator output needed to drive the laser. Breakdown voltages of order 60 kV are anticipated. Laser head impedances of order 0.4 to 0.7 have been shown to apply for the relevant electrode spacings. Thus a nominal 100 J input pulse to the laser head is achieved with a 100 ns flat top pulse. The driving network is slightly mismatched with the laser load. The most significant element of such a circuit requirement is the rapid dI/dt necessary. A current rate of rise of order 2 x 10^{12} amps per second is anticipated for the 2 J laser head.

Such performance can be achieved in a variety of ways. Considering first the output switch, we compare rail gaps, spark gaps and thyratrons. Our experiments utilized an electrically triggered rail gap, as well as laser triggered gaps. This method easily produces the requisite current rate of rise. The significant issue is that of lifetime. Various work in laser triggering shows that input energies of a few mJ, such as that provided by our commercial excimer laser product EXCI-LITE^{TM}, can successfully trigger a rail gap with order of 30 to 100 channels per meter. The lifetime with respect to erosion of the electrodes of such a device is not known but could be of order 10^2 to 10^4 times that of a single channel spark gap. Thus, verification tests of a repetitively pulsed rail switch are required to qualify this technology for a long run device. The laser physics risk of a laser triggered or electrically triggered rail gap based modulator are low, but the technology risks are considered high.

Voltage

60 kV

20 kV

0   10 ns

125 ns

Current

50 kA

25 ns

100 ns
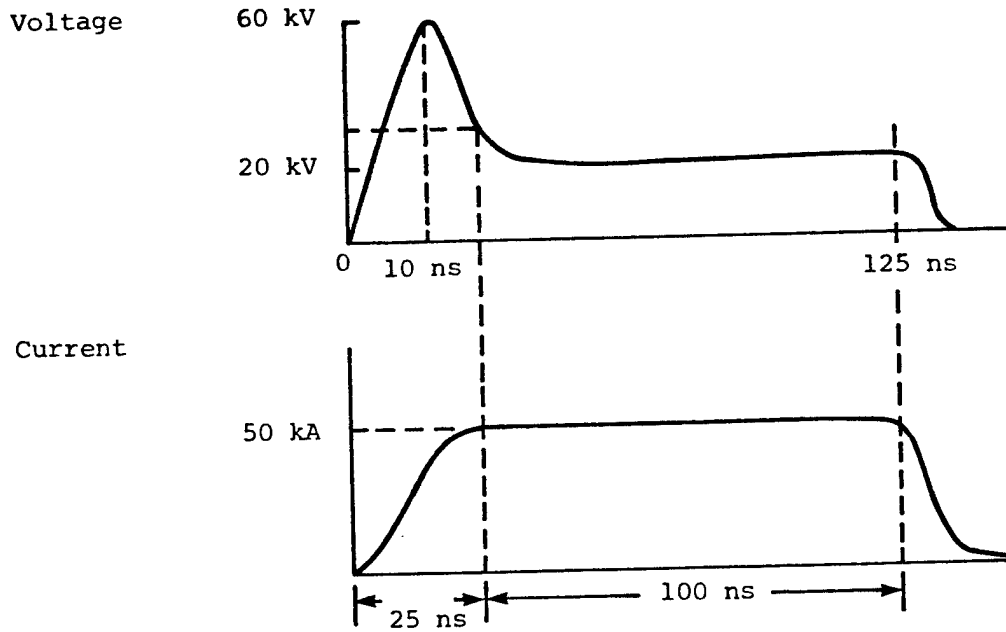
Figure 4-8.   Ideal Requirements for Current and Voltage Outputs at the Laser Head for the Electric Modulator.

Moreover, the gas flow power requirements are unknown but likely to be nontrivial.

Single spark gaps are not suited for this application for two reasons: inductance and, hence, efficiency and lifetime. Multiple parallel spark gaps are a possible selection, and in fact were utilized in some of our 50 cm device experiments. This method is deemed unsatisfactory from both a laser physics viewpoint and from a lifetime and technology risk view point.

Thyratrons are the final possible selection for a gas switch. Their principal advantage is a proven rep rate and long lifetime capability. These devices are inadequate in terms of peak current, current rate of rise and inductance for typical thyratrons. Although one tube is insufficient to drive the 2 J laser head, a modulator utilizing multiple parallel PFN's and thyratrons can deliver the requisite parameters. This approach is straightforward but cumbersome. Moreover the lifetime of large thyratrons used in parallel is probably adequate for a 10^8 shot run life at 100 Hz. Extension to the 10^{10} shot level will require some technology development, however. The largest negative aspect of a multiple parallel thyratron approach is the efficiency of the tube, both in terms of anode heating losses and in standby power for the cathodes of conventional thyratrons. To achieve the requisite modulator efficiency we need a high efficiency charging system. Our laser head efficiency of 2 percent is also thought to be a lower limit on the efficiency of this media given the rapidly maturing technology base, and further experiments will relax the modulator efficiency requirements. We select for this conceptual design multiple parallel thyratron approach. Clearly, a laser physics verification test is required to show that a thyratron system will provide the requisite laser energy. The circuit diagram for such a pulser is shown in Figure 4-9. Ten parallel PFN's will store ~150 J, easily sufficient to drive the 2 J laser. EGG 5313, and 5333 gradient grid tubes, ITT F187 and 178 tubes and the EEV-CX1536 all appear to be candidates for tube selection.
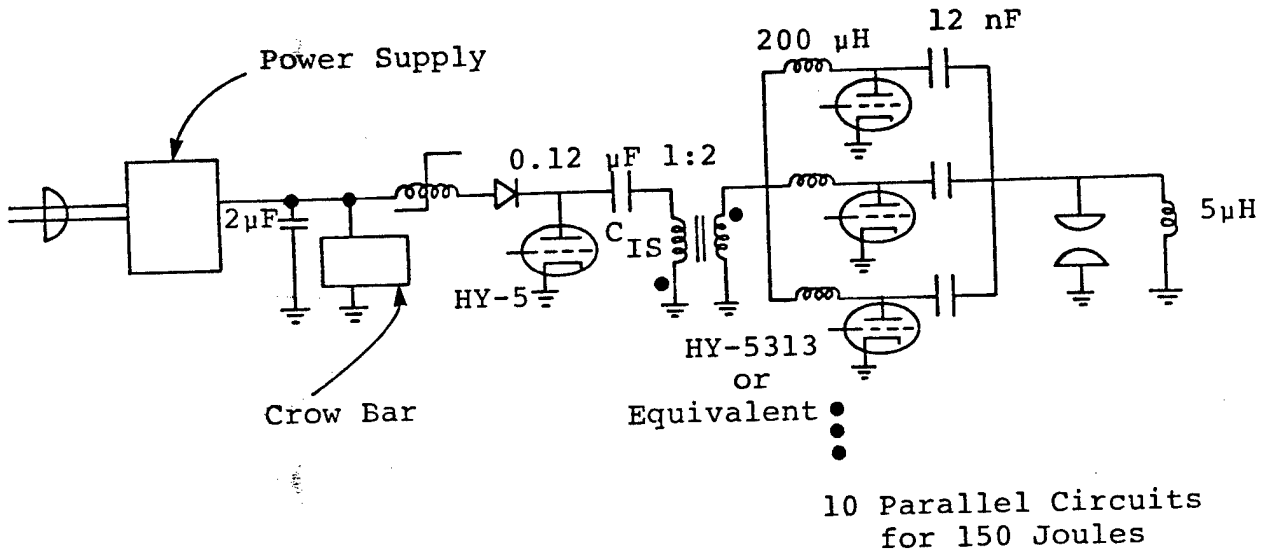
Figure 4-9. Multiple Thyratron HgBr Pulser.

In designing the modulator and laser head and transition sections we must consider the inductance, capacitance, charge voltage and laser impedance and their interrelation. The parallel pulse forming networks (PFN) that are proposed to achieve the desired low impedance energy storage should match the discharge impedance, expected to be in the range of 0.5 to 1 . The design requirements for the PFN's are shown in Figure 4-10. This scaling graph is based on 125 J stored in the PFN capacitance to deliver 100 J to the laser head with an assumed 80 percent pulser efficiency. At the demonstrated medium efficiency of 2 percent, this would result in a 2 J laser pulse.

The circuit was assumed to be a single section type A Guillemin network with a matched resistive load[4], i.e., a series RLC cricuit with an ideal switch. The capacitance is calculated using $E = 1/2\ CV^2$ for E = 125 J. The inductance is calculated using $L = 0.22\ ^2/C$, where is approximately the full width half maximum (FWHM) current pulse duration for the type A network.[9]

Based on the experimental results with the 1 m single pulse laser, we are projecting a required charge voltage of 50 kV to breakdown the gas. At this charge voltage the pulser capacitance should be 100 nF. The predicted cavity inductance of 12 nH precludes pulse durations shorter than 70 nsec; when the inductance of circuit components and connections to the laser are included, the minimum pulse duration is probably about 90 nsec. For a 100 nsec pulse the total circuit inductance, including the laser head, should be less than 33 nH.

4.5 Optics and Other Subsystems

The flow, pulsed power, and laser head design issues present the most difficult technological problems for the Phase II HgBr laser. However, to ensure successful completion of such a program, there are several other systems issues that must be carefully addressed, because they play a role in achieving the ultimate mission goals. This section describes the methods available for generating the specified optical performance, in regards to both beam divergence and spectral narrowing.
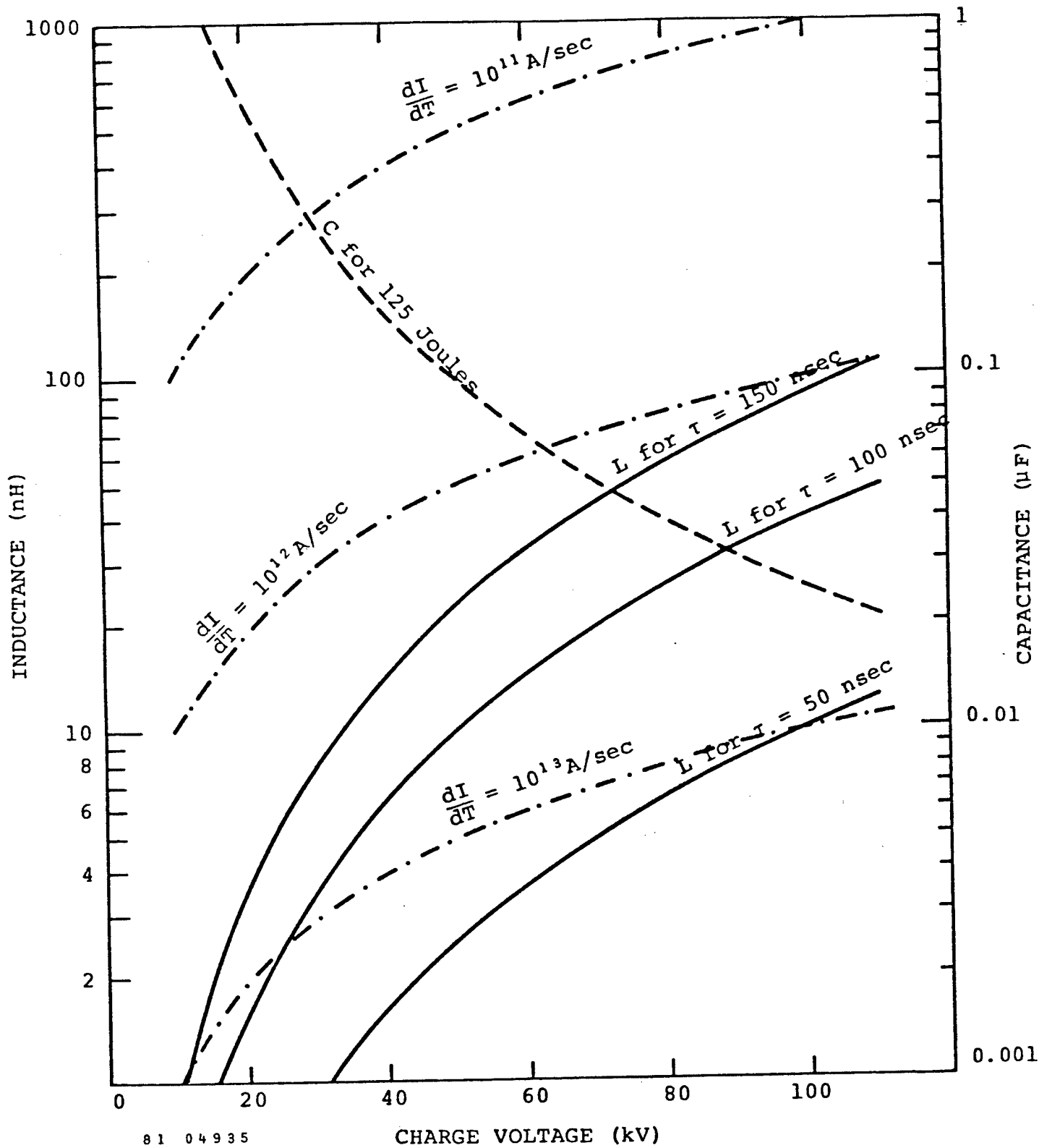
Figure 4-10. Scaling Curves for Pulse Forming Network (PFN).

The control and diagnostic subsystems, which are essential to conducting a successful experimental program, are presented.

4.5.1 Front End/Narrowbanding

The required spectral and spatial properties for the high average power laser output can be produced by an extension of MOPA concepts which have been used in high-power system of many kinds. The needed characteristics are generated at a low-power level, and then transferred to the high-power laser via one or more stages of injection locking or high-order multipass amplification. This approach is preferable to the insertion of spatial/frequency filtering components into the high power oscillator resonator, because insertion of such devices would inevitably introduce additional losses which would in turn result in loss of output power. In contrast, control of laser characteristics using seed radiation does not compromise laser output power, and in fact may increase it, because better total energy extraction of the primary oscillator during the startup regime may result from seeding.

To exploit this kind of technique, it is necessary to first provide a seed source having the desired spectral and spatial characteristics. This source must be capable of running at the needed rep rate, and must have sufficiently high efficiency that it does not significantly impact the total system wall-plug power consumption. The power level required for the seed source is an open question at present. Based on experience with injection locking of short pulse rare-gas halide oscillators, we anticipate that a peak power of 10 kW would serve as a useful upper limit for the seed source needed during these injection experiments. We anticipate that a small HgBr discharge laser could be used as the seed source.

Ideally, the seed pulse length should be as long as the pulse length of the primary laser to reduce temporal jitter requirements and to ensure the most stable possible injection locking of the entire pulse. However, control of laser properties using shorter injection pulses has been amply demonstrated, so that this requirement is not an absolute one.

The small HgBr reference oscillator can itself be injection locked using either a HgBr discharge laser, line narrowed by intracavity dispersive elements, or to some other tertiary source. One possible low power injection source is the argon ion laser, which intrinsically produces the needed linewidth (typically 5 Ghz). The 501.7 nm Ar^+ line has an excellent overlap with the HgBr gain spectrum, as has been amply demonstrated in Phase I experiments at MSNW. Because these lasers are always operated in low Fresnel number configurations within long narrow discharge tubes, the needed beam quality is also then essentially an intrinsic property of the laser. The Ar+ laser can be operated in a pulsed mode with a duty cycle of perhaps 10^{-4} (1 usec pulses) to bring the average input power to a reasonable value. Relatively low power input levels are necesssary since at higher current density the desired 501.7 nm line begins to disappear from the output spectrum.

4.5.2 Optics and Beam Quality

The primary requirements of the optical system needed by the high average power mercury bromide laser are the capability of providing appropriate beam quality while operating under the environmental conditions imposed by the high average optical power incident on the various optical components.

A positive branch unstable resonator can probably be used for the primary resonator. The gain and loss parameters derived from previous MSNW experiments and from kinetic modelling suggest that a magnification of 3-4 will provide the optimal output coupling. Resonators of this kind have been demonstrated to be capable of generating reasonably high-quality beams in a number of short pulse lasers, including discharge pumped rare-gas halide,[10] Q-switched Nd:Yag[11], and copper vapor.[12] The primary limitation on beam quality, aside from optical aberation within the laser medium itself, is the finite time needed to form a low divergence beam, which is frequently referred to as the "collapse" or "response" time for the

resonator. There are several qualitative models used for describing this transient process, which are in rough agreement.[13] Using the response time as defined by Hargrove et.al.,

$$\tau_r = \frac{2L}{C} \frac{\ln\left[\frac{N(M-1)}{\eta M}\right]}{\ln M}$$

the calculated response time as a function of resonator magnification is shown in Figure 4-11. The geometric parameters of the proposed HgBr resonator were used in this calculation. This response time has been shown experimentally to give a good description of the actual mode collapse time in copper vapor lasers[14].

At the magnifications required for appropriate output coupling it is clear that a significant part of the output optical pulse length may be required to acheive the desired beam quality. One way to circumvent this time is to inject optical power with good beam characteristics into the resonator during the buildup phase of the pulse, so that the laser begins operation in a high quality mode. Because the beam quality specification for the HgBr system is not extremely stringent, it appears likely that in a pulse integrated sense, the beam quality specification may be met by the primary oscillator alone. However, because injection also appears to be desirable for spectral control, it can be made an integral part of the optical system throughout our experiments.

REFERENCES

1. C.S. Liu, Westinghouse R & D Center, Private Communication.

2. E. Schimitschek, Private Communication.

3. H. Braune and R. Linke, Z. Physik. Chem. B31: 12 (1925).
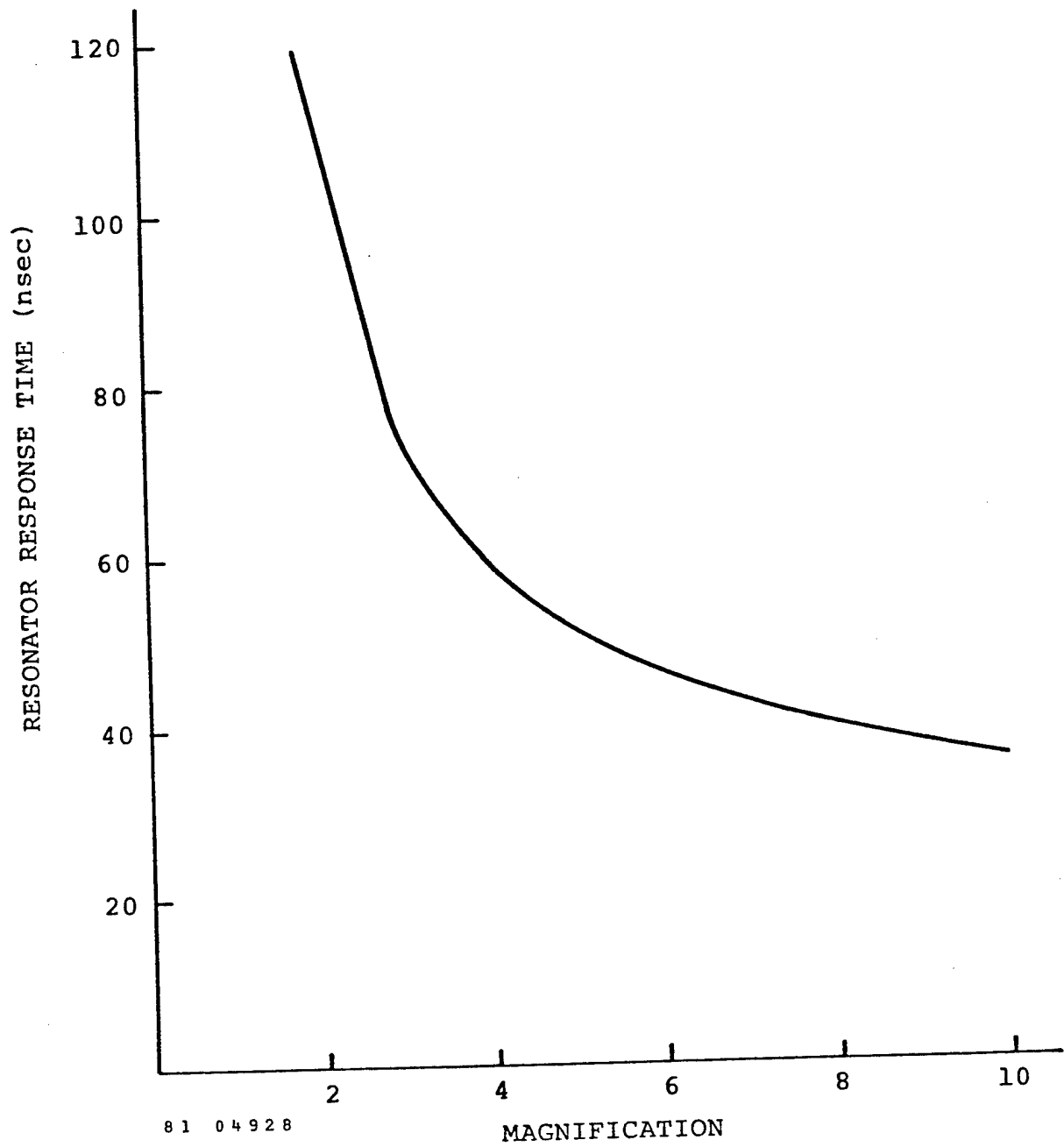
Figure 4-11. Resonator Response Time vs.
Resonator Magnification.

4. C.S. Fisher and R.E. Center, MSNW Report 76-1053-1, submitted to Lawrence Livermore Laboratory, December 1976.

5. J.L. Leavatter and S.C. Lin, J. Appl. Phys. 51, 210 (1980).

6. W.J. Wiegand, Final Report, Contract N00014-79-1-0593.

7. R.D. Evans, The Atomic Nucleus, McGraw Hill, New York.

8. A.H. Compton and S.K. Allison, X-rays in Theory and Experiment, D. Van Nostrand Co., New York.

9. Pulse Generators, G.N. Glasoe and J.V. Lebacqz, Editors, Dover Publications, New York.

10. Terrence J. McKee, and Walter Skilac, IEEE QE-15, 335 (1979).

11. R.L. Herbst, H. Komine, and R.L. Byer, Opt. Comm. 21: 5 (1977).

12. K.I. Zenskov, A.A. Isaev, M.A. Kazaryan, G.G. Petrash, and S.G. Rautian, Sov. J. Quantum Elec. 4: 474 (1974).

13. A.A. Isaev, M.A. Kazarya, G.G. Petrash, S.G. Rautian, and A.M. Shalagia, Sov J. Quantum Electron 7: 746 (1977).

14. R.S. Hargrove, R. Grove, and T. Kan, IEEE QE-15, 1228 (1979).

APPENDIX A

HgBr Laser Kinetics Code Inputs

List of Reactions and Rate Constants

Reaction	Rate Constant	Reference

Electron Excitation

| Reaction	Rate Constant	Reference
$N_2 + e \rightarrow N_2(VIB) + e$	$f(E/N, Q_{ij})$	1
$N_2 + e \rightarrow N_2(A) + e$	"	1
$N_2 + e \rightarrow N_2(B) + e$	"	1
$N_2 + e \rightarrow N_2(a^1\pi_g) + e$	"	1
$N_2 + e \rightarrow N_2(C) + e$	"	1
$N_2 + e \rightarrow N_2^+ + e$	"	2
$Ne + e \rightarrow N_e^* + e$	$f(E/N, Q_{ij})$	3
$Ne + e \rightarrow N_e^{**} + e$	"	est.
$Ne + e \rightarrow N_e^+ + e$	"	2
$HgBr_2 + e \rightarrow HgBr + Br^-$	$f(E/N, Q_{ij})$	4
$HgBr_2 + e \rightarrow HgBr(X,B,C) + Br + e$	"	est.
$HgBr_2 + e \rightarrow HgBr_2^+ + e$	"	4

Penning Ionization

$Ne^* + N_2 \rightarrow N_2^+ + e + Ne$	8.0×10^{-11}	est.
$Ne^* + HgBr_2 \rightarrow HgBr_2^+ + e + Ne$	2.4×10^{-10}	est.

Ion-Electron Recombination

$N_2^+ + e \rightarrow N_2$	10^{-7}	5
$Ne_2^+ + e \rightarrow Ne^{**} + Ne$	$f(E/N)$	6
$HgBr_2 + e \rightarrow Products$	1×10^{-7}	7
$HgBr_2^+ + e \rightarrow Br + HgBr(B)$	0.1×10^{-7}	est.
$HgBr_2^+ + e \rightarrow Br + HgBr(C)$	0.1×10^{-7}	est.
$HgBr_2^+ + e \rightarrow Br + HgBr(X)$	0.8×10^{-7}	est.

Ion-Ion Recombination

$Ne^+ + Br^- \rightarrow Ne + Br^*$	10^{-6}	est.
$N_2^+ + Br^- \rightarrow N_2 + Br^*$	10^{-6}	est.
$HgBr_2^+ + Br^- \rightarrow Products$	3.0×10^{-7}	7
$HgBr_2^+ + Br^- \rightarrow 2Br + HgBr(B)$	$0.1 \times 3 \times 10^{-7}$	est.
$HgBr_2^+ + Br^- \rightarrow 2Br + HgBr(C)$	$0.1 \times 3 \times 10^{-7}$	est.
$HgBr_2^+ + Br^- \rightarrow 2Br + HgBr(X)$	$0.8 \times 3 \times 10^{-7}$	est.

Dimer Formation

$Ne^+ + 2Ne \rightarrow Ne_2^+ + Ne$ 4.4×10^{-32} 8

$Ne^* + 2Ne \rightarrow Ne_2^* + Ne$ 4.0×10^{-34} est.
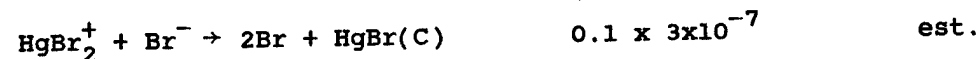
Neutral Channel Formation of HgBr(*)

$N_2(A) + HgBr_2 \rightarrow N_2 + Br + HgBr(C)$ $0.0 \times 3.5 \times 10^{-10}$ est.

$N_2(A) + HgBr_2 \rightarrow N_2 + Br + HgBr(B)$ $0.3 \times 3.5 \times 10^{-10}$ 9

$N_2(A) + HgBr_2 \rightarrow N_2 + Br + HgBr(X)$ $0.7 \times 3.5 \times 10^{-10}$ 9

$HgBr(C) + M \rightarrow HgBr(B) + M$

      $M = N_e$ 5.3×10^{-13} est.

         $= N_2$ 4.4×10^{-12} est.

         $= HgBr_2$ 1.7×10^{-10} est.

$Br^* + HgBr_2 \rightarrow HgBr(C) + 2Br$ 3.0×10^{-10} est.

Quenching of HgBr(*)

$HgBr(B) + M \rightarrow HgBr(X) + M$

      $M = Ne$ 5.3×10^{-13} 10

         $= N_2$ 4.4×10^{-10} 10

         $= HgBr_2$ 1.7×10^{-10} 10
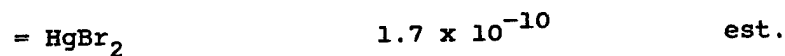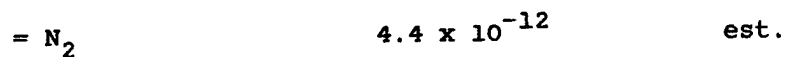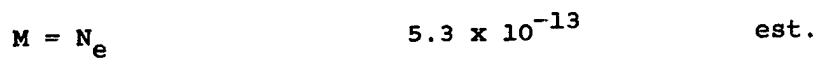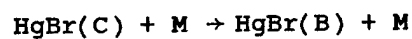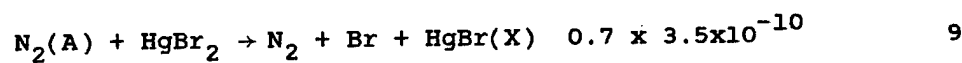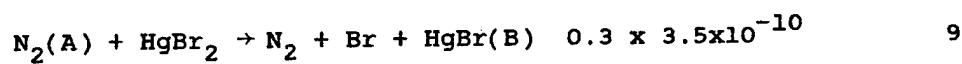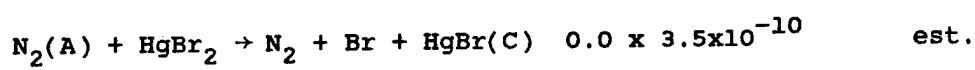
= e	1.0×10^{-7}	est.

$HgBr(C) + M \rightarrow HgBr(X) + M$

M = Ne	5.3×10^{-13}	est.
= N_2	4.4×10^{-12}	est.
= $HgBr_2$	1.7×10^{-10}	est.
= e	1.0×10^{-7}	est.

$HgBr(C) + e \rightarrow HgBr(B) + e$	1.0×10^{-7}	est.

Radiation from HgBr(X)

$HgBr(B) \rightarrow HgBr(X,v=22) + h\nu$	4.4×10^{7}	10
$HgBr(B) + h\nu \rightarrow HgBr(X,v=22) + 2h\nu$	$1.5 \times 10^{-16} cm^2$	11
$HgBr(C) \rightarrow HgBr(A)$	4.4×10^{6}	est.

Lower Laser Level Removal

$HgBr(X,v=22) + M \rightarrow HgBr + M$

M = Ne	6.9×10^{-11}	12
= N_2	1.8×10^{-10}	12

Radiation

$N_2(C) \rightarrow N_2(B) + h\nu$	1.7×10^{7}	13

$N_2(B) \rightarrow N_2(A) + h\nu$ 4.0×10^5 13

$Ne_2^* \rightarrow 2Ne + h\nu$ $1/4 \times 3 \times 10^8$ 14

Miscellaneous

$N_2(A) + N_2(A) \rightarrow N_2(C) + N_2$ 10^{-11} est.

$N_2(A) + N_2(A) \rightarrow N_2(B) + N_2$ 1.6×10^{-10} est.

$HgBr + Br + Ne \rightarrow HgBr_2 + Ne$ 1.0×10^{-32} est.

$Ne^{**} + Ne \rightarrow Ne^* + Ne$ 5.0×10^{-11} est.

Kinetics Table References

1. A.G. Englehardt, A.V. Phelps and G.G. Risk, Phys. Rev. 135, A1566 (1964).

2. D. Rapp and P. Englander-Golden, J. Chem. Phys. 43, 1469 (1965).

3. M. Schaper and H. Scheibner Beit. Plasma Phys. 9, 45 (1969).

4. W.J. Wiegand (UTC report R80-924780-1, July 31, 1980).

5. D.H. Douglas-Hamilton J. Chem. Phys. 58, 4820 (1973).

6. J.N. Bardsley and M.A. Biondi in <u>Advances in Atomic and Molecular Physics</u> (Academic Press, NY, 1970).

7. W.L. Nighan, Appl. Phys. Lett., 36, 173 (1980).

8. A.V. Phelps JILA Data. Memo. No. 1, Joint Institute for Laboratory Astrophysics, Boulder, CO (1977).

9. R.S.F. Chang and R. Burnham Appl Phys. Lett., 36, 397 (1980).

10. J.G. Eden and R.W. Waynant Appl Phys. Lett., 34, 324 (1979).

11. E.J. Schimitschek and J.E. Celto Appl. Phys. Lett., 36, 176 (1980).

12. H. Helvajian, M. Mangir, and C. Wittig Chem. Phys. Lett.,71, 177 (1980).

13. A.W. Johnson and R.G. Fowler J. Chem. Phys. 53, 65 (1970).

14. D.C. Lorents, Physica. 82c, 19 (1976).